DESIGN OF MACHINES AND STRUCTURES

A Publication of the University of Miskolc

Volume 13, Number 2 (2023)

EDITORIAL BOARD

CONTENTS

IMPROVING CHATTER PERFORMANCE OF A LATHE SPINDLE THROUGH GRAPHO-OPTIMIZATION

MOHAMMAD ALZGHOUL[1] – FERENC SARKA[2] – FERENC JÁNOS SZABÓ[3]

University of Miskolc, Institute of Machine and Product Design
H-3515, Miskolc-Egyetemváros
[1]mohammadzgoul90@gmail.com, [2]ferenc.sarka@uni-miskolc.hu, [3]ferenc.szabo@uni-miskolc.hu
[1]https://orcid.org/0000-0002-4673-3328, [2]https://orcid.org/0000-0003-3136-4248,
[3]https://orcid.org/0000-0002-6694-8959

Abstract: Structural modifications to spindle systems have been demonstrated in previous studies to improve their dynamical performance. The aim of this study is to improve the performance of a lathe spindle system in terms of chatter occurrence, while maintaining the same overall mass of the system. The design of the spindle system is optimized using the grapho-optimization method, employing the Kuhn-Tucker optimality criterion to evaluate the design parameters. Specifically, the thickness of the spindle shaft and the diameter of the shaft next to the chuck are varied. The optimized spindle system shows a significant improvement in the first natural frequency value compared to the original design; the first natural frequency is increased by 59.7 %.

Keywords: Spindle system, Chatter, Spindle model, FEM analysis

1. INTRODUCTION

Machine tools depend on spindle systems to hold and rotate cutting tools or workpieces. Spindle shaft stiffness affects its static and dynamic behaviour, affecting lathe machine performance (Rayapati & Rathijit, 2020). Previous studies have examined spindle models, from simplified Euler-Bernoulli beam theory models (Alzghoul, Cabezas, & Szilágyi, 2022) to more complex models using Timoshenko beam theory in the systems receptance coupling approach (Alzghoul, Sarka, & Szabó, 2022) (Kato, Kono, & Kakinuma, 2022), and models solved and analysed using the finite element method with computer programs like ANSYS (Mahdavinejad, 2005) (Baker & Rouch, 2002). Despite these efforts, optimizing spindle design for lathe machine

applications is difficult. Production quality and efficiency depend on spindle system performance (Yan & Zhu, 2019) (Alzghoul, Sarka, & Szabó, 2022). Studies have shown that spindle system structural modifications improve dynamical performance (Tong, Hwang, Shim, Oh, & Hong, 2020) (Lv, Li, Jin, He, & Li, 2021) (Lin, 2014). The current study uses grapho-optimization to optimize a spindle system in a lathe machine to reduce chatter while maintaining mass. The Kuhn-Tucker optimality criterion is used to evaluate design parameters like spindle shaft thickness and shaft diameter next to the chuck (Szabó, 2018) and the location of the rear bearing. Finite element analysis calculates natural frequency.

2. ANALYSIS

The proposed model of the lathe spindle consists of a shaft with uniform thickness, three bearings, a chuck, and a workpiece. Figure 1 is the section view of the model. Major considerations need to be taken into account. Firstly, the minimum diameter of the shaft should not be less than 55 mm, as it is necessary for the bar feeding mechanism. Additionally, the thickness of the shaft must not be less than 7 mm, considering the maximum allowable angle of twist to be 0.25 °/m (Zsáry, 1999), the applied torque applied to the spindle is 576 Nm (based on the data sheet of Haas ST-35L CNC lathe (Haas, 2023)). Finally, the stiffness of the bearings is assumed to be 7.5+008 N/m (Stone, 2014).
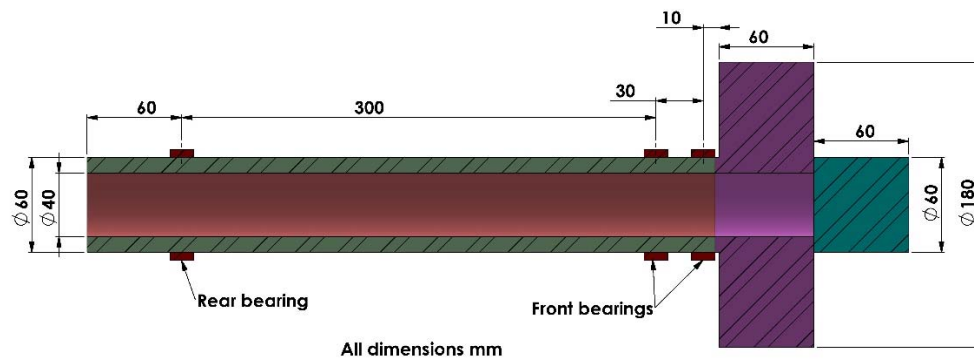
Figure 1. *Section view of lathe spindle proposed model.*

A single diagram with the objective function iso-lines and feasible region borders can represent constrained optimization problems. The optimization system is created by setting the constraints of the optimization problem and defining the objective function and its contours. To maintain shaft mass, the proposed model increases the

inner diameter of the shaft adjacent to the chuck while reducing its thickness. Two variables are introduced and related by the formula for the volume of a truncated hollow cone, as the pre-optimized shaft system volume is 628318.53 mm^3. The two variables are the cone's second radius (R) and thickness (t). Figure 2 illustrates the truncated hollow cone.
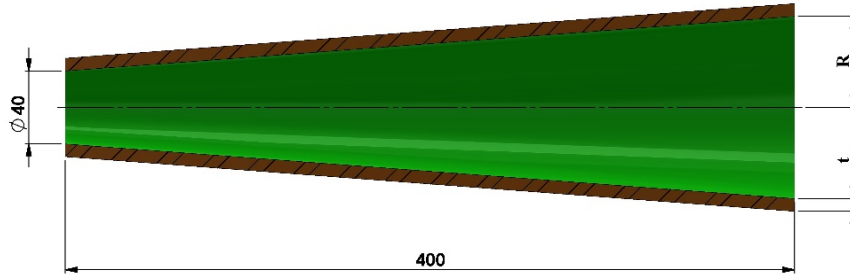
Figure 2. *Section view of the truncated hollow cone representation for optimizing spindle shaft design*

The relationship between the variables is derived from the volume equation and is presented as equation (1).

$$R = \frac{650.33 - 27.5t - t^2}{t} \tag{1}$$

Additional constraints are introduced as follows:

$$R \geq 27.5 \ mm \tag{2}$$

$$7 \leq t \leq 10 \ mm \tag{3}$$

Where R is the internal radius next to the chuck (mm) and t is the thickness of the shaft (mm).

The first natural frequency of the spindle system was determined using the Finite Element Method with ANSYS 19 for a range of R and t values to establish the objective function. A second-degree polynomial representing the objective function in equation (4) was fitted to the data set.

$$R(t) = 4.41t^2 - 125.54t + 1141.8 \tag{4}$$

The optimization process is visualized in Figure 3, which shows a plot of the objective function and its contours alongside the implicit and explicit constraints.
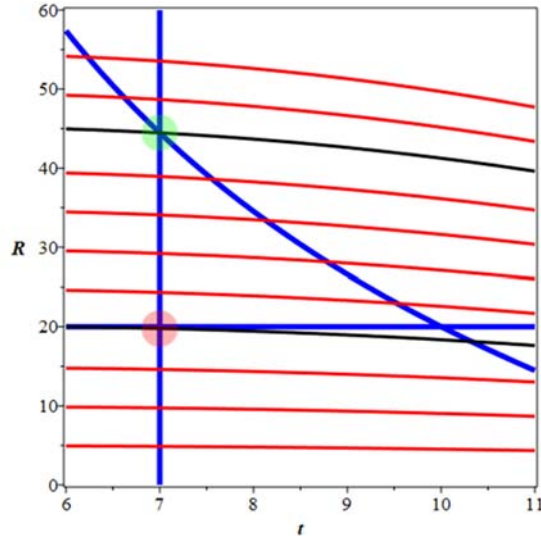
Figure 3. *The plot of the constraints and the objective function contours of the first natural frequency*

In Figure 3, the feasible solution region is the area between the constraint borders (blue lines and curve). Red contours indicate objective function. Black curves are optimal objective function contours. The green circle is the optimal point where two constraints and one objective function contour intersect. Green circle has 7 mm t, 44.46 mm R. The highest first natural frequency is expected with a 7 mm shaft thickness and 44.46 mm radius adjacent to the chuck.

The second parameter is to investigate the location of the rear bearings (as illustrated in Figure 1), the main steps of the previous part are repeated in order to construct the objective function. For the constraints, the first constraint is the axial location of the bearing taking the left end of the shaft as a reference, then the constraint of the axial location (as illustrated in Figure 1) of the bearing is expressed as:

$$7.5 \ mm \leq t \leq 200 \ mm \tag{5}$$

Setting L as the axial location of the rear bearing which ranges from 7.5 mm, the bearing centre, to 200 mm, the shaft midpoint. And D as the shaft diameter, L and D

relationship is another constraint. (The shaft section is conical now.) This relationship is:

$$D = 0.0612L + 26.54 \tag{6}$$

To determine the objective function, the spindle system is analysed using the finite element method for various D and L values to determine the first natural frequency, which was determined using the Finite Element Method with ANSYS 19 for a range of D and L values to establish the objective function. A third-degree polynomial representing the objective function, Equation 7, was fitted to the data set.

$$D(L) = (-0.3.\,10^{-5})L^3 - 0.0027L^2 - 1.1843L + 703.62 \tag{7}$$

Figure 4 plots the objective function, contours, and implicit and explicit constraints to illustrate optimization. The optimization problem is plotted to help understand the objective function-constraint relationship.
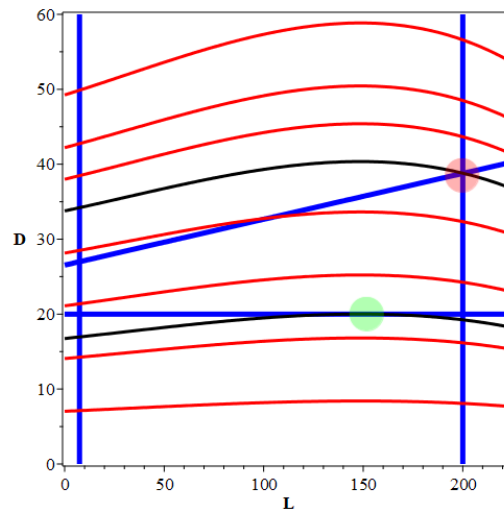
Figure 4. *The rear bearing location constraints and first natural frequency objective function contours plot.*

In Figure 4, the feasible solution region is enclosed between constraint border blue lines. Red curves show objective function contours. Black curves are optimal objective function contours. The green circle is the maximum point because it is tangent

to the feasible region. This implies that there is only one intersection solution when the two curves are equal. The green circle has 152 mm L. This implies the highest first natural frequency is 152 mm from the shaft left end at the rear bearing centre. The red point is the minimum optimal point.

3. RESULTS

Figure 5 shows the pre-optimized spindle system in sub-figure 'a' and the optimized version in 'b'. The figure shows optimization changes.
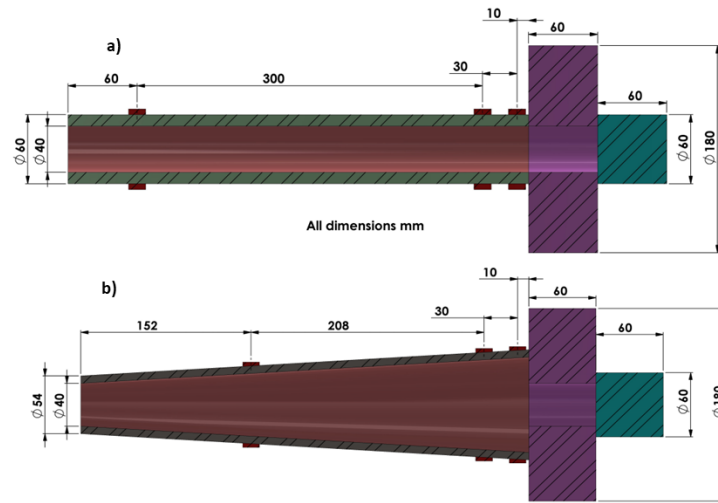
Figure 5. *Comparison of the a) pre-optimized and the b) optimized spindle systems*
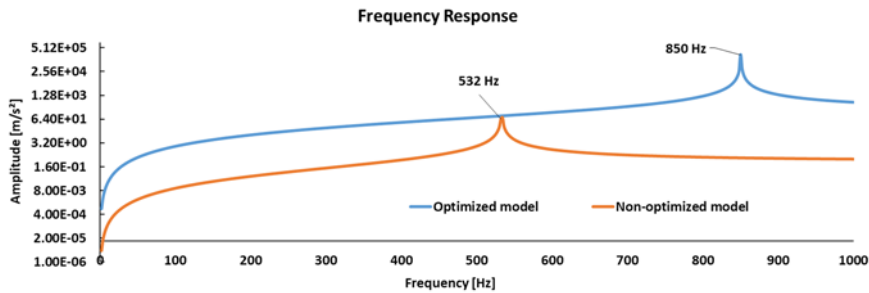
Figure 6. *The frequency response of the pre-optimized spindle system and the optimized spindle system*

Figure 6 compares the frequency response of the optimized and pre-optimized spindle systems. The x-axis shows frequency in Hertz and the y-axis acceleration in m/s^2. Both curves were generated by applying 1 kN (excitation force) to the workpiece and extracting the response with ANSYS 19. The optimized curve shifts right, indicating a higher first natural frequency than the pre-optimized curve.

4. CONCLUSIONS

According to this study, structural modifications to spindle systems can significantly improve dynamical performance. The grapho-optimization method improved the first natural frequency of a lathe spindle system while maintaining its mass. The optimization method needs more testing for other spindle systems and applications. This study shows that optimization can improve spindle system performance and industrial process efficiency.

REFERENCES

Alzghoul, M., Cabezas, S., & Szilágyi, A. (2022, May 04). Dynamic modeling of a simply supported beam with an overhang mass. *Pollack Periodica, 17*(2), 42–47. https://doi.org/10.1556/606.2022.00523

Alzghoul, M., Sarka, F., & Szabó, F. (2022). A spindle system analysis using systems receptance coupling approach. *Design of Machines and Structures, 12*(2), 24-30. https://doi.org/10.32972/dms.2022.010

Alzghoul, M., Sarka, F., & Szabó, F. (2022). Analytical and experimental techniques for chatter prediction, suppression and avoidance in turning: literature survey. *Design of Machines and Structures, 12*(2), 31-40. https://doi.org/10.32972/dms.2022.011

Baker, J., & Rouch, K. (2002). Use of finite element structural models in analyzing machine tool chatter. *Finite Elements in Analysis and Design, 38*(11), 1029–1046. https://doi.org/10.1016/S0168-874X(02)00050-1

Haas. (2023, 04. 20.). Retrieved 04 20, 2023, from Haas web site: https://www.haas.co.uk/lathes/st-35l/

Kato, M., Kono, D., & Kakinuma, Y. (2022). Dynamical characteristic validation of motorized CFRP spindle unit based on receptance coupling. *Mechanical Systems and Signal Processing, 173*. https://doi.org/10.1016/j.ymssp.2022.109028

Lin, C.-W. (2014). Optimization of Bearing Locations for Maximizing First Mode Natural Frequency of Motorized Spindle-Bearing Systems Using a Genetic Algorithm. *Applied Mathematics, 5*(14), 2137-2152. https://doi.org/10.4236/am.2014.514208

Lv, Y., Li, C., Jin, Y., He, J., & Li, J. (2021). Energy saving design of the spindle of CNC lathe by structural optimization. *The International Journal of Advanced Manufacturing Technology, 114*(1), 541-562. https://doi.org/10.1007/s00170-021-06758-4

Mahdavinejad, R. (2005). Finite element analysis of machine and workpiece instability in turning. *International Journal of Machine Tools and Manufacture, 45*(7-8), 753–760. https://doi.org/10.1016/j.ijmachtools.2004.11.017

Rayapati, S., & Rathijit, D. (2020). Selection of Lathe Spindle Material Based on Static and Dynamic Analyses Using Finite Element Method. *Materials Today, 22*(4), 1652-1663. https://doi.org/10.1016/j.matpr.2020.02.182

Stone, B. (2014). *Chatter and Machine Tools.* Perth: Springer. https://doi.org/10.1007/978-3-319-05236-6

Szabó, F. (2018). Optimization of Springs Applied in Vehicle Suspension Structure. In K. B. Jármai (Ed.), *Vehicle and Automotive Engineering 2. VAE.* Springer, Cham. https://doi.org/10.1007/978-3-319-75677-6_51

Tong, V., Hwang, J., Shim, J., Oh, J.-S., & Hong, S.-W. (2020). Multi-objective Optimization of Machine Tool Spindle-Bearing System. *International Journal of Precision Engineering and Manufacturing, 21*(10), 1885–1902. https://doi.org/10.1007/s12541-020-00389-7

Yan, B., & Zhu, L. (2019). Research on milling stability of thin-walled parts based on improved multi-frequency solution. *International Journal of Advanced Manufacturing Technology, 102*(1), 431–441. https://doi.org/10.1007/s00170-018-03254-0

Zsáry, Á. (1999). *Gépelemek I.* Budapest: Nemzeti Tankönyvkiadó.

RECONSTRUCTION OF SIMPLE PARTS USING FDM TECHNOLOGY

CSABA DÖMÖTÖR

University of Miskolc, Institute of Machine and Product Design
H-3515, Miskolc-Egyetemváros
csaba.domotor@uni-miskolc.hu
https://orcid.org/0000-0002-6406-3460

Abstract: This article shows the experiences of component reconstruction supported by FDM 3D printing through a few examples. It presents the profile copying technique that can be used as an alternative to traditional measuring methods and 3D scanners for relatively complicated parts.

Keywords: FDM printing, machine element reconstruction, copying geometry

1. INTRODUCTION

The reconstruction of machine components is one of the most elementary engineering tasks. Because of this, already at the BSc mechanical engineer students in all universities meet with this challenge during their studies.

The essence of this elementary creative activity is to determine the original geometry of a touchable, but in most cases unusable (worn, broken) part. An important task of the process is the preparation of a technical drawing of the selected part containing the dimension, tolerance and material information required for remanufacturing if production documentation is not available.

2. THE AIM OF THE RECONSTRUCTION

2.1. Unavailable parts for replacement

The reconstruction of machine components may be necessary in several cases. Sometimes the productive machine is simply so old that product support or the

purchase of spare parts is not available. However, by replacing a single failed or worn part, the lifetime of this expensive equipment can be significantly extended.

2.2. Reducing lost time

Another frequently occurring problem is that the part that we need to be replaced can be available, but the delivery takes much longer than we can afford by taking the machine out of production. A solution may be to temporarily use a machine component with a shorter service life –or even a narrower functionality–, but which can be quickly accessed by means of component reconstruction.

2.3. Economical repairing

A similar situation is when an original part can only be purchased at such a high cost that it is not economical to pay for continued operate of the equipment. In this case the machine part can be replaced by an element, produced by a proper rapid prototyping technology (RPT), that is perfectly suitable in long term.

3. TRADITIONAL PRACTICE

For each of the cases listed in paragraph 2, it is essential to define the precise geometry required for assembly and operation. (Bihari & Szente, 2011) Engineer students in the practical courses of the Machine Elements I. subject at the University of Miskolc usually have to perform the documentation process of the reconstruction of axle, disc, gear and simple cast parts. This work, which may seem to be difficult at first sight as a second-year student, gives them practice in the use of conventional measuring tools (vernier calliper, micrometres, radius templates, thread combs, etc.) and the application of their knowledge of engineering drawing.

4. USE OF NEW TECHNIQUES

4.1. Stand-alone modelling equipment

In addition to traditional measurement methods, it is also possible to define the geometry of the component using advanced equipment. In the past, engineers used a profile projection device to determine 2D projections, which is now an important segment of the history of technology (Figure 1.a). But nowadays 3D coordinate measuring machines or even contact or non-contact optical surface digitizing devices are also common solutions. (Sarka & Tóbis, 2017) (Figure 1.b)

a)   b)
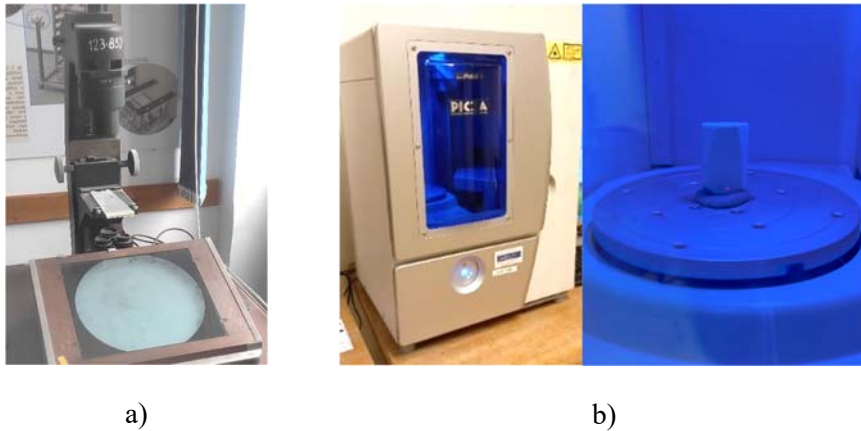
Figure 1. *a) Past: CarlZeiss Projector 320*
b) Present: Roland LPX-1200 laser scanner

4.2. An alternative method

These modern geometry digitisation techniques also have limits and, in most cases, require specific training for operators. In such cases, the use of old methods supported by modern technologies is a good alternative solution.

Taking a digital photo with the right resolution and orientation is very similar to the 'old age' profile projector principle, but the image is processed by a computer. In all cases, it is essential that the photograph (or microscope image) of the part to be reconstructed has an accurate millimetre (or micrometre) scale on the picture, which can be used as a reference for processing. (Figure 2)
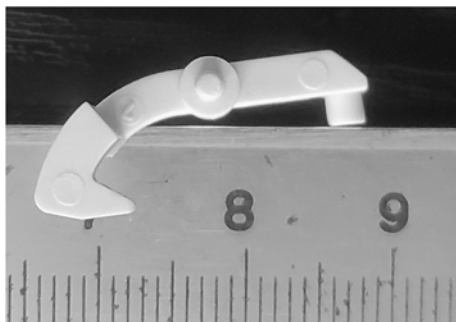
Figure 2. *Mechanical timer clock switch arm with millimetre scale*

5. WORKFLOW

5.1. Preparation and photography

If not all the dimensions of the part are defined or a complex CAD model is not obtained by scanning, the final geometry can be determined by reconstructing the edges and proportions shown in the projection photograph of the part. This can be aided by colouring the edges before photographing, for example with graphite powder for light parts or chalk powder for dark machine parts. After photography, it is possible to further highlight the edges using image manipulation programs (e.g., GIMP, PhotoShop).

5.2. Processing in CAD

The prepared and cropped photo can be set up as a background image in a suitable CAD software (e.g., Solid Edge, Creo, etc.) as a desktop in the editor. Of course, the size of the part is not yet defined, so it is a good idea to crop the photo to fill the drawing area of the CAD program as much as possible.

The next step is to redraw the bounding curves of the visible projection as accurately as possible. At this point, the dimensions are still flexible and only the shape of the sketch is drawn. In this step, information from the operation of the part and from the measurement of surfaces that can be specified with conventional tools is used. So, for example, if we know that there is a rounding, we do not approximate it with a perpendicular spline, but with a normal circular arc. In the same way, straight lines, parallels, and perpendiculars, known angles or even the coaxiality are available from our knowledge of the features of the part through our engineering experience. It is useful to indicate the known dimensions on the sketch, but not yet as a construction definition, but as a flexible guide that can be freely varied during the subsequent steps of the design.

5.3. Scaling

After the 2D shape sketch is complete, the key step follows it in the process, which is the scaling. Every CAD program has a tool that can zoom in and zoom out on the selected drawing elements while maintaining their fixed relationship to each other.

Since a known size is entered as an informative dimension, it can be divided by the real equivalent of the original part measurement to determine the exact ratio of magnification or reduction. Then it can be used to scale the part to obtain the scale projection. From this sketch, we can use a protrusion or revolved protrusion tool to

create a 3D body model, on which we can make further refinements based on our previous measurements.

5.4. Modification, redesign

After getting the original part geometry, it is possible to improve the part before production. Either by carrying out tests with FEM or simply by considering expected loads, failure that has occurred or the space available for the part in the machine, we can usually reinforce the critical cross-sections –mostly through the addition of material to the set.

6. 3D PRINTING

After conversion to a file format managed by the 3D printer (e.g., STL), the CAD model is ready to print. In the present case, FDM printing –using a thermoplastic polymer substrate fed as filament– is considered as one of the most common rapid prototyping processes.

6.1. Building structure and fibre orientation

More research has shown that the orientation of the component structure, in other words the plane in which the printing layers are parallel to each other, has a relevant influence on the mechanical properties of the finished product. (Konya & Ficzere) (Albert & Takács, 2023) It is easy to see that, in a technology where layer separation is an existing problem, the directions of load that result in their mechanical separation should be avoided.

Similar to this, fibre orientation and the rate of internal filling are parameters that need to be chosen consciously. For example, results from a series of measurements carried out at John von Neumann University GAMF Department of Materials Technology show that in all cases measured, a 45° fibre orientation resulted in specimens with higher impact-bending strength, higher tensile strength, and higher elongation at break. (Ádám & Polgár, 2019)

6.2. Material selection

The choice of FDM printing material is also a crucial consideration when aiming for a product with a relatively long lifetime. The most commonly used materials are ABS, ASA and PLA (Marada & Bihari, 2022) and their doped versions. Among these, PLA known for its easy (lower temperature) printability, is perhaps the most popular. Of course, its heat resistance is correspondingly lower than usual, limited

to max.60°C. Care should be taken when printing finished products that may be exposed to higher temperatures at the point of installation or during operation.

A solution can be found in CPLA (crystallised PLA), a material designed for products with higher heat requirements. Products printed from CPLA have a heat resistance up to 80°C. (Qingdao Knowledge Industry & Trading Corporation, 2022)

If you are expecting higher stress, TPLA (tough PLA) with increased mechanical performance is a good choice. The name TPLA refers to PLA doped with talc, where talc is a natural mineral that helps PLA to form a harder material. Thus, while maintaining the lightweight printing authority, you can get increased impact resistance, but only at the lower heat resistance typical of PLA. (MakerBot Industries, 2023)

7. PRACTICAL EXAMPLES

7.1. Switch arm

The first example shows the reconstruction of a component that cannot be purchased, because the structure containing this component is also not a particularly expensive product, so spare parts are not provided. However, after the cause of the failure had been identified, the reconstruction of this low-material-demand switcher arm was a natural step (also due to the availability of 3D printing).

a)   b)
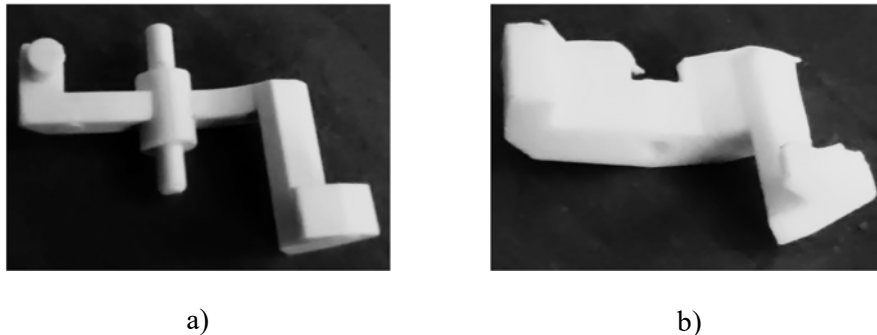
Figure 3. a) original part b) redesigned switch arm

As shown in Figure 3, the original geometry of this rocker arm has undergone several modifications. The broken small cross section of the arm has been given maximum thickness considering the available space. A further modification was the replacement of the crankshaft, injection moulded from the same material as the original part, with a hole of the same diameter, into which a steel rod was later inserted, thus increasing the lifetime of the component (Figure 4).

It is obvious, but important to note in the case of a printed spare part, that it is advisable to print in the laid down position, taking into account the expected loads. Experience has shown that a part produced in this way has been working continuously and correctly for a year after installation.

Figure 4. *3D printed switch arm being installed*

7.2. Cooling fan

In this example, a higher thermal load is applied to this machine component. The interesting aspect of the problem is that a special shaft-hub connection had to be reconstructed. The compressor fan shown in Figure 5 is a component that fits on the eccentric shaft end of a crank mechanism.

Figure 5. *3D printed fan in motion*

In order to ensure a shock-free operation, it was important to determine the most precise hole position as possible. The stiffening ribs of the hub have been slightly modified to allow the impellers to be held in place by a larger support. As a result, the product has operated without problems for many years with intermittent use.

7.3. RC car part

The last example is an often-breakable plastic part. This is a sleeve bearing, closed at one end, which is a radio remote control model car component that holds the front swing fork axle in place without play. Due to the variability of the chassis geometry, its design is not symmetrical (Figure 5.a). Experience shows that it has a long life in normal operation, but it works as a breaking element in a crash and in this way it protects more expensive components from damage.

a)   b)
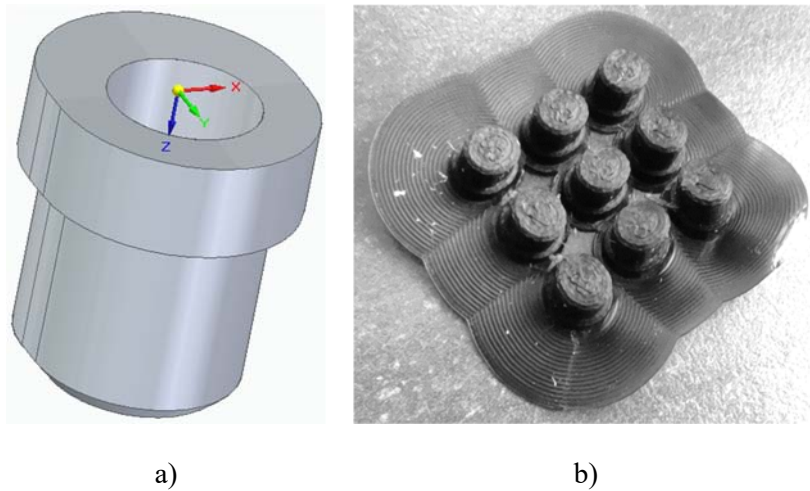
Figure 6. *a) CAD model of the shaft positioning sleeve*
b) Spare parts printed in multiple copies

8. SUMMARY

Experience has shown that 3D printing based on FDM technology has become suitable for the reconstruction of real and working parts. With the right choice of layers, printing directions and other parameters, long-life and properly functioning replacement parts can be produced.

REFERENCES

Ádám, B., & Polgár, B. (2019). 3D nyomtatott próbatestek mechanikai vizsgálata. *Gradus, 6*(1), 185-191.

Albert, J., & Takács, Á. (2023). Additív gyártás biomimetikai megközelítéssel. *GÉP, 74*(4), 9-12.

Bihari, Z., & Szente, J. (2011). Speciális geometriájú gépelemek rekonstrukciója. *Multidiszciplináris Tudományok*, 143-150.

Konya, G., & Ficzere, P. (dátum nélk.). The Effect of Layer Thickness and Orientation of the Work piece on the Micro- and Macrogeometric Properties and the Machining Time of the Part during 3D Printing. *Periodica Polytechnica-Mechanical Engineering, 67*(2), 143-150. https://doi.org/10.3311/PPme.21473

MakerBot Industries. (2023. September 29). Forrás: MakerBot Industries Web site: https://support.makerbot.com/s/article/1667337612208

Marada, I., & Bihari, J. (2022). Experiences with 3D printing of small plastic gears using FDM and SLA. *GÉP, 73*(3-4), 60-65.

Qingdao Knowledge Industry & Trading Corporation. (2022. August 22). Forrás: Qingdao Knowledge Industry & Trading Corporation Web site: https://www.ecopulppak.com/info/what-s-the-difference-between-pla-and-cpla-74277848.html

Sarka, F., & Tóbis, Z. (2017). The potential of 3D scanning and prototyping in the production of packaging tools - a case study. *GÉP, 68*(4), 47-52.

INVESTIGATION OF THE DEPTH IMPACT OF THE IRONING PROCESS USING SEM IMAGES AND CAD SYSTEM

PÉTER FICZERE[1] – NOÉMI LÁSZLÓ[1,2]

[1]Budapest University of Technology and Economics,
Department of Railway Vehicles and Vehicle System Analysis,
1111, Budapest, Műegyetem rkp. 3.
[2]H-ION Kutató, Fejlesztő és Innovációs Kft. – SEM Labor
[1]ficzere.peter@kjk.bme.hu, [2]noemi.laszlo@h-ion.hu
[1]https://orcid.org/0000-0003-3207-5501, [2]https://orcid.org/0000-0002-8912-2711

Abstract: The adoption of additive manufacturing within the automotive sector is progressively growing, primarily attributed to the technology's speed, relative ease of use, and its capability to manufacture components with intricate geometries that are beyond the reach of traditional methods. This holds especially true for enhanced or structured plastic parts. A variety of instrumental, analytical, and image analysis techniques are accessible for both qualitative and quantitative assessment of surface structures. This article outlines the potential of utilizing scanning electron microscopy (SEM) and CAD for image analysis in this context.

Keywords: ironing, SEM, CAD, Additive manufacturing, surface topology, FDM

1. INTRODUCTION

The implementation of Industry 4.0, which is now expected in an increasing number of areas, poses many challenges. Industry 4.0 imposes a number of conditions, of which the need to use additive manufacturing technologies becomes clear if we only think of the specific requirements to be met and the need to react quickly. The role of additive manufacturing technologies has changed significantly in recent times, and they are no longer seen as a marketing tool or a rapid prototyping process. Quality requirements have changed accordingly. Not only the correct geometric design, but also criteria for dimensional accuracy, colour, shape, feel and material suitability, as well as appropriate load-bearing capacity, are being set. As a result, the additive manufacturing engineer today needs to have a much more profound knowledge than

before. It is easy to see that, if we think only about the appropriate load-bearing capacity, the use of generative design, developed to exploit the specific features and advantages of additive manufacturing technologies and supported by artificial intelligence, is now essential (Albert & Takács, 2023), (Borsodi & Takács, 2022). The surfaces of parts created by additive manufacturing technologies do not guarantee the quality expected in the engineering field, and therefore often require some kind of surface improvement process. However, these processes not only modify the surface quality, but also the morphology of the material. It is therefore important to understand the effect of the parameters of each process on surface quality and morphological changes. Achieving uniform surface qualities as a goal is particularly difficult for parts produced by layer-by-layer build-up, where the manufacturing technology results in parts with different material properties and surface qualities in different directions.

The application of surface modification processes is becoming increasingly common for parts produced by additive manufacturing. Additive manufacturing or 3D printing uses innovative methods to produce parts layer by layer. These parts often have to meet different functional and aesthetic requirements, and surface modification processes are used to meet these requirements.

These processes can be chemical, mechanical, or coating and can be aimed at improving mechanical properties, smoothing the surface or modifying technical properties. For example, surface treatment may be used to apply coatings to the parts to increase wear resistance or corrosion resistance. In addition, laser surface treatment and the use of electrochemical processes are also becoming increasingly common in additive manufacturing. The best-known surface finishing processes are machining (Kónya & Ficzere, 2023), (Kónya & Ficzere, 2022), rolling, coating and ironing (Alzyod, Takács, & Ficzere, 2023).

In the present study, the effect of the parameters of the ironing process used in FFF (Fused Filament Fabrication) technology on the surface quality was investigated. The ironing process consists of "going through" the top layer again after a part has been printed, by holding the nozzle temperature but not or only very little material is deposited on the surface. This means that the high temperature (and very small amount of material) should cause the surface to merge more effectively, filling the gaps better and making the surface "smoother" and denser.

The investigated parameters are:
- ironing speed,
- rate of material addition,
- distance between the tool paths covered by the nozzle.

The test pieces were 10 mm edge length cubes from PLA material.

Previous studies (Ficzere, 2023) have shown that the surface roughness can be significantly reduced by the reinforcement process, as shown in Figure 1.
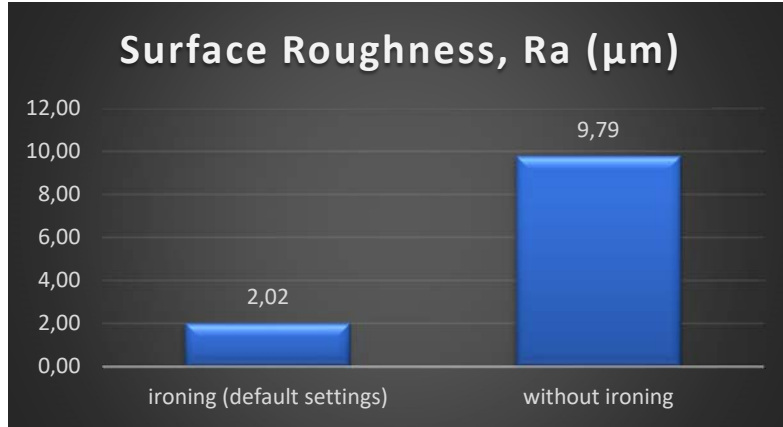
Figure 1. *Comparison of ironed and non-ironed surfaces (Ficzere, 2023)*

Since there is a clear correlation between surface roughness and dimensional accuracy (tolerances), it can be stated that parts with up to 4 tolerance classes more accurate (IT) can be achieved with ironed surfaces.

It was also established that the surface roughness increases with increasing ironing speed, but the increase is not significant. In addition, it can be stated that the smaller the deposited amount of material during the ironing process, the better the surface quality. However, it must also be seen that this is not significant. However, it is important to note that the smaller the ironing distance during the ironing process, the more efficient the process.

These tests were carried out with a Keyence VR-5000 microscope.

In addition to the results obtained, we wanted to investigate the depth changes of the reinforced layer during the ironing process. To do this, scanning electron microscope images were taken.

2. METHODOLOGY

In order to determine the dependence of the thickness of the ironed layer on the manufacturing parameters, test specimens were prepared with different settings. Table 1 shows the test parameters. The images for the test were taken with a Zeiss Sigma 300 scanning electron transmission electron microscope (FE-SEM).

Test parameters to determine the thickness of the ironed layer

	Ironing speed (mm/s)	Ironing distance (mm)	Flowrate (%)	Layer thickness (mm)	Ironed layer
1	20	0.1	5	0.2	Top layer
2	80	0.1	5	0.2	Top layer
3	20	0.4	5	0.2	Top layer
4	20	0.1	20	0.2	Top layer
5	20	0.1	5	0.3	Top layer
6	20	0.1	5	0.4	Top layer
7	20	0.1	5	0.2	Every layer

Figure 2 shows a scanning electron microscope (SEM) image of an iron clad layer on one of the specimens.
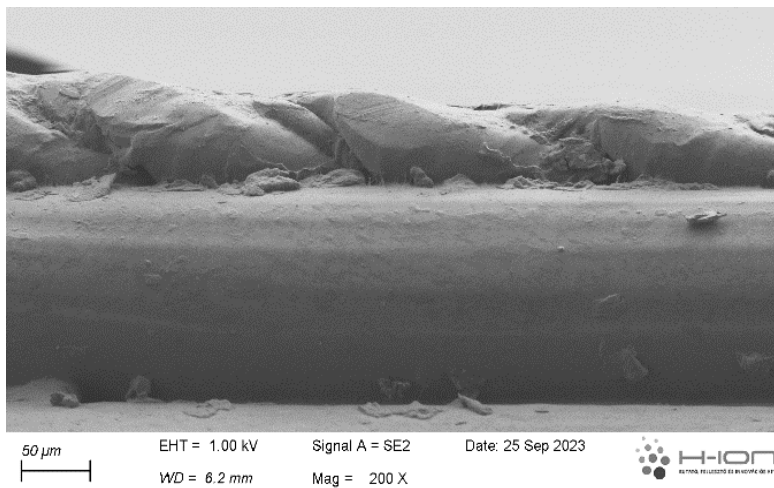
Figure 2. *SEM image of an ironed layer*

It can be clearly observed in the figure that the thickness of the resulting surface layer is not uniform. It is possible to measure at several locations, or even to examine the layer height in equal divisions over a base length, as we do for the average surface roughness, but it is clear that our average depends on where we measure. Of course, the more measurement locations, the more accurate the average layer thickness.

Today's CAD systems allow us to instantly generate all area information (area size, centre of gravity, moments, etc.) for areas bounded by closed curves. This allows us to insert SEM images taken for inspection purposes as backgrounds on a sketch plane. Next, based on the scale of the SEM images, we rescale the image to see it at true size. We then draw a contour around the layer of interest, as shown in Figure 3. It is important to note that this method can only be used if the sample itself has flat surfaces. A possibility of verification is to measure the known layer thickness under the ironed surface.
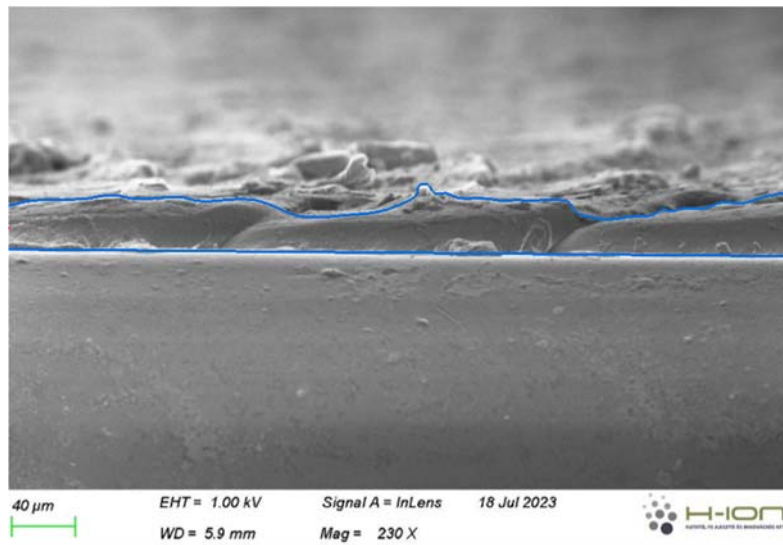
Figure 3. *Ironed layer drawn around in CAD system*
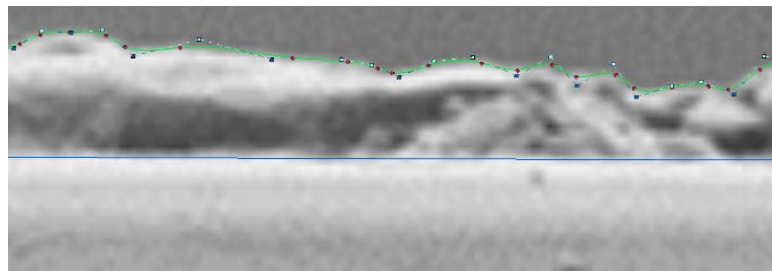
Figure 4. *NURBS curve approximated boundary of the ironed surface*

It can also be observed in Figure 4 that the base can be approximated practically well by a straight line, while the upper contour can only be approximated by a NURBS (Non-Uniform Rational Bezier Spline) curve of at least third order.

At the beginning and at the end of the inspected length, the section to be examined is closed by straight lines perpendicular to the base. In this way, we obtain the length and the size of the investigated area, as shown in Figure 5.

From this information, we can easily calculate that if we had a perfect surface - a rectangle would be the enclosed area - the height of this rectangle would be. This height is equal to the average height of the ironed layer.
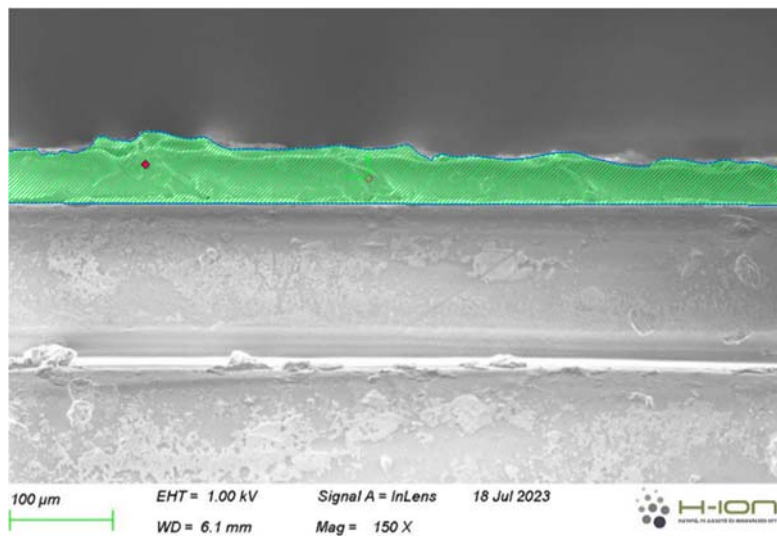
Figure 5. Obtaining area information bordered by curves using CAD software

The procedure presented here was used to examine the pieces for each parameter setting and calculate the average thickness of the ironed layers.

3. RESULTS

The average depth of the ironed layer measured under different production and ironing parameters is shown in Table 2. The base length, area and resulting depth of the ironed layer for the settings according to the series numbers in Table 1 can be read from Table 2.

Table 2
Results from CAD software based on SEM images

	Base length (μm)	Area covered (μm2)	Depth of the ironing (μm)
1	764.25	34420.95	45.04
2	228.2	2700.91	11.84
3	229.3	485.2	2.12
4	505.05	15687.26	31.06
5	229.42	7650.36	33.35
6	1618.56	193374.9	119.47
7	763.5	47460.71	62.16

4. ANALYSIS

The principal results of the study are summarised in Table 3.

Table 3
Ironing depth as a function of ironing parameters

	Ironing speed (mm/s)	Ironing distance (mm)	Flowrate (%)	Layer thickness (mm)	Ironed layer	Depth of the ironing (μm)
1	20	0.1	5	0.2	Top layer	45.04
2	80	0.1	5	0.2	Top layer	11.84
3	20	0.4	5	0.2	Top layer	2.12
4	20	0.1	20	0.2	Top layer	31.06
5	20	0.1	5	0.3	Top layer	33.35
6	20	0.1	5	0.4	Top layer	119.47
7	20	0.1	5	0.2	Every layer	62.16

Analysis of the results shows that:
- as the ironing speed increases, the depth of the ironed layer decreases,
- as the ironing distance increases, the depth of the ironed layer decreases,
- as the flow rate increases, the depth of the ironed layer decreases,
- the depth of the ironed layer increases in the case of for each layer ironed.

A discrepancy was found in the determination of the depth of the ironed layer as a function of the print layer thickness, so this requires further, repeated investigations. Figure 6 also clearly shows the ironed layer between the deposited layers.
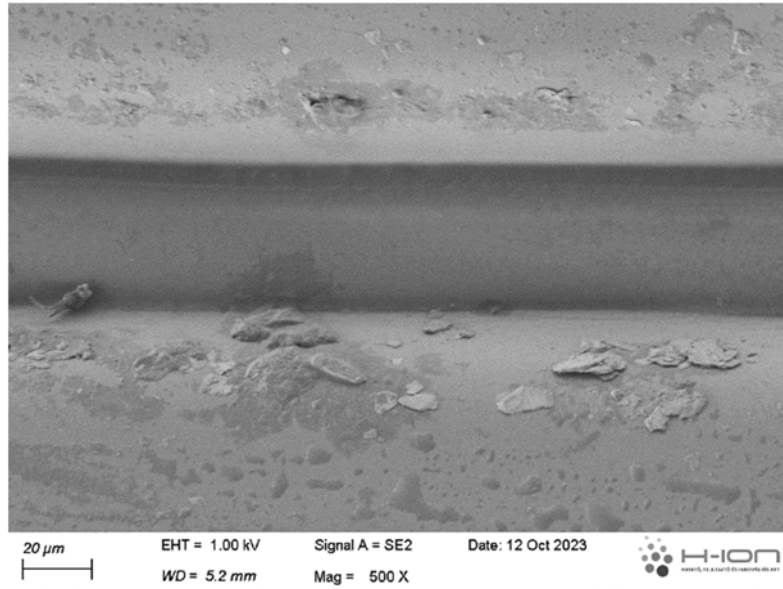
Figure 6. *SEM image of the ironed layer between printed layers*

5. SUMMARY

Taking into account the results of the examinations, it can be concluded that the ironing parameters have a significant effect on the depth of the ironed layer.

It is important to note that only one in-line test was performed in the present study, therefore, for more accurate and reliable results, it may be worthwhile to examine values taken in several cross-sections.

In order to increase the reliability of the results, CT (Computer Tomography) scans will also be performed in the future.

The results - the depth of the ironed layers - are also expected to have a significant effect on the mechanical properties, and we will continue our research in this approach.

REFERENCES

Albert, J., & Takács, Á. (2023). Additív gyártás biomimetikai megközelítéssel. *GÉP, 74*(4), 9-12.

Alzyod, H., Takács, J., & Ficzere, P. (2023). Improving surface smoothness in FDM parts through ironing post-processing. *Journal of Reinforced Plastics and Composites*. https://doi.org/10.1177/07316844231173059

Borsodi, E., & Takács, Á. (2022). Generative Design: An Overview and Its Relationship to Artificial Intelligence. *Design of Machines and Structures, 12*(2), 54-60. https://doi.org/10.32972/dms.2022.013

Ficzere, P. (2023. szeptember 15). *A vasalási eljárás paraméter-változásának hatása a felületi érdességre FFF el-járással készített additív gyártás esetén.* (N. J. Egyetem, Rendező) Országos Additív Ipari Tudományos Konferencia és Workshop, Kecskemét.

Kónya, G., & Ficzere, P. (2022). A rétegvastagság és az alkatrész tájolásának hatásai az alkatrész mikro- és makrogeometriai jellemzőire 3D nyomtatás során. *Gradus, 9*(2). https://doi.org/10.47833/2022.2.ENG.005

Kónya, G., & Ficzere, P. (2023). The Effect of Layer Thickness and Orientation of the Work-piece on the Micro- and Macrogeometric Properties and the Machining Time of the Part during 3D Printing. *Periodica Polytechnica Mechanical Engineering, 67*(2), 143-150. https://doi.org/10.3311/PPme.21473

NEW METHOD FOR THE GEOMETRIC DESIGN OF THE RUNNER WHEEL OF THE BÁNKI TURBINE

SÁNDOR HAJDÚ

University of Miskolc, Institute of Energy Engineering and Chemical Machinery
3515, Miskolc-Egyetemváros
hajdusor@gmail.com
https://orcid.org/0009-0007-4291-6673

Abstract: This article is a continuation of a previous publication by Author. Paper (Hajdú, 2022) analyses the velocity relationships in the flow stream through the Bánki turbine. By exploring the velocity relationships, it is possible to determine the flow losses in the turbine runner and the runner efficiency of the runner. By implementing the theoretical results in practice, a new design procedure for the geometry of the runner of the Bánki turbine is developed.

Keywords: streamline, methodology, runner efficiency, Bánki-turbine

1. INTRODUCTION

The Hungarian literature on Bánki's turbine has long lacked further development of the theory, which has stagnated since Bánki's time. In order to move forward, it was necessary to turn the research work in a completely new direction, breaking away from the available precedents in the Bánki turbine literature. Important result of this research work, beyond the results summarised in (Hajdú, 2022), is the new design procedure based on the determination of the runner efficiency of the Bánki turbine runner. The interpretation of the indices assigned to the velocity and the direction angle of the velocity on the radius circle is the same as it was given in the above-mentioned literature. Likewise, the interpretation of the x, y orthogonal coordinate system and the r, ϕ polar coordinate system are also the same.

2. THE BANKI TURBINE IN THE PARTIAL OPENING CONDITION

Quantities for partial openings are indicated by the subscript i. For full closure of the waterway $i = 0$, for full opening $i = 1$. The regulating tongue is rotated by an angle δ_1 from its position of full closure to its position of full opening (Figure 1.). In the case of partial opening, the angle of rotation of the control tongue is less than δ_1, as expressed by the following relation: $\delta_i = i\delta_1; \dots 0 \leq i \leq 1$.
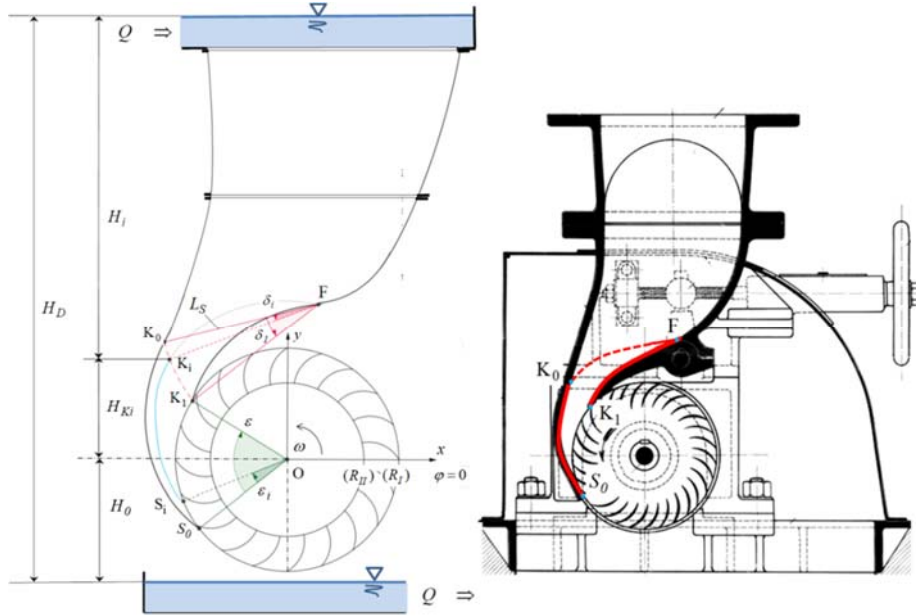
Figure 1. Schematic of the Bánki turbine in the partial opening condition

The flow at the runner inlet in the partial opening condition is assumed to be
- the direction angle of the flow on the section $S_i S_0$ (Figure 1.) of the runner circumference is equal to the direction angle α_0,
- the central angle associated with the section $S_i S_0$ varies in proportion to the opening parameter i: $\varepsilon_i = i\varepsilon; 0 \leq i \leq 1$

The variation of the $H_i < H$ head as a function of the opening determines the $c_{1,i} < c_1$ flow velocity of the fluid on the runner.

$$c_{1,i} = \sqrt{2gH_i} = c_1\sqrt{H_i/H} \tag{1}$$

The flow velocity at the inlet in the direction perpendicular to the inlet surface:

$$c_{1m,i} = c_{1,i} \sin \alpha_0 = \sin \alpha_0 \sqrt{2gH_i} = c_1 \sin \alpha_0 \sqrt{H_i/H} \tag{2}$$

The volume flow rate through the runner varying as a function of the opening parameter:

$$Q_i = R_I \varepsilon_i L c_{1m,i} = R_I i \varepsilon L c_1 \sin \alpha_0 \sqrt{H_i/H} = iQ\sqrt{H_i/H} \; ; \quad 0 \le i \le 1 \tag{3}$$

3. THE EFFICIENCY SHELL DIAGRAM OF THE BÁNKI TURBINE

In paper (Hajdú, 2022), equations (16) and (17) interpret the runner efficiency for the partial opening condition as the difference between the theoretical runner power and the contraction, collision, and friction performance losses in the runner in the partial opening condition. By combining the above equations (16) and (17), a formula is obtained to calculate the runner efficiency for the partial opening condition:

$$\eta_{jk,i} = \frac{P_{jk,i}}{P_H} = \frac{P_{E,i} - P'_{0,i} - P'_{K,i} - P'_{V,i}}{P_H} = C_{2,i}\psi^2 + C_{1,i}\psi \tag{4}$$

$$C_{2,i} = -\frac{i}{1 + \cot^2 \alpha_0}\left(\frac{H_i}{H}\right)^{3/2}\left[2 + \frac{2\cot\beta_I}{\psi_0} + \zeta_{K,i}\left(S_{II}^2 - \frac{1}{\psi_0^2 S_{II}^2}\right) - \frac{\zeta_{V,i}}{\psi_0^2 S_{II} \sin \beta_I}\right] \tag{5}$$

$$C_{1,i} = \frac{2i}{1 + \cot^2 \alpha_0}\left(\frac{H_i}{H}\right)^{3/2}\left[3\cot\beta_I + \psi_0 - \frac{\zeta_{K,i}}{\psi_0 S_{II}^2} - \frac{\zeta_{V,i}}{\psi_0 S_{II} \sin \beta_I}\right] \tag{6}$$

The equation (4) obtained for the runner efficiency of the runner interprets a surface in the three-dimensional rectangular coordinate system i, ψ, η and can therefore be used to construct a shell diagram of the Bánki turbine runner efficiency. This shell diagram is nothing more than the image of the surface described by the previous equation, represented by the $\eta_n = const$ level lines. The implicit equation of such a level line is:

$$C_{2,i}(i)\psi^2 + C_{1,i}(i)\psi - \eta_n = 0 \qquad (7)$$

The solution of this second-degree algebraic equation (7) for ψ:

$$\psi_{1,2}(i) = \frac{-C_{1,i}(i) \pm \sqrt{C_{1,i}^2 + 4C_{2,i}\eta_n}}{2C_{1,i}(i)} \qquad (8)$$

which provides the upper and lower sections of the level line in question in the orthogonal coordinate system (Figure 2).
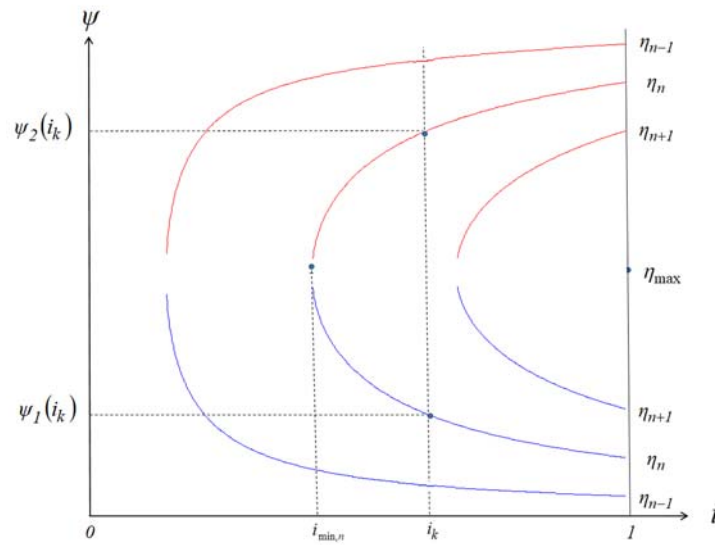
Figure 2. *Level lines of the runner efficiency surface of the runner on the i, ψ coordinate plane*

The interpretational range of the efficiency curve in the i, ψ coordinate plane is $i_{min,n} \leq i \leq 1$; and this curve has a peak at the abscissa $i = i_{min,n}$ (Figure 2.). At the peak of the curve, the tangent to the curve is vertical, and the two curve segments are located to the right of this point. The equation $C_{1,i}^2 + 4C_{2,i}\eta_n = 0$ is true for the abscissa at the peak of the curve. The abscissa value can be calculated from the above equation by a series of trial-and-error operations.

4. DESIGN OF THE BÁNKI TURBINE

The design task is to determine the main geometric dimensions of the Bánki turbine that can optimally utilize the $P_D = \rho g Q H_D$ power coming from the river at a given location for a given pair of values Q (flow rate to the turbine) and H_D (difference in level of the dam).
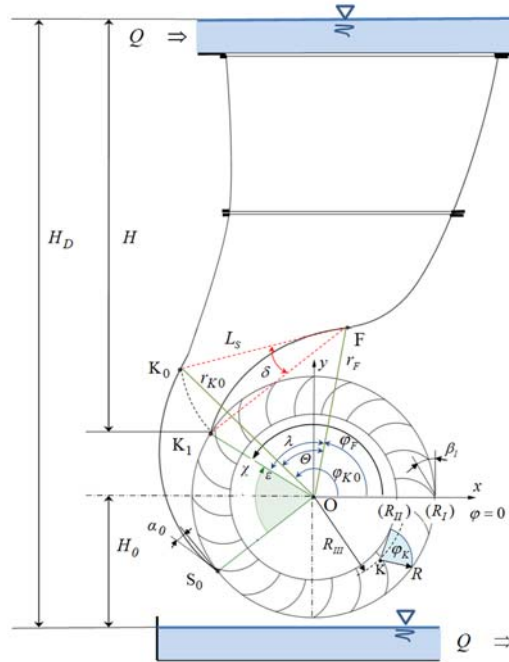
Figure 3. *The angles and radii determining the installation of the Bánki turbine and the runner bladed space and the logarithmic spiral guideway walls*

The initial design data are:
(a) the volumetric flow rate of the water flow through the turbine Q (m^3/s);
(b) the difference in dam level at the location H_D (m);
(c) the ratio of the runner radii $R_{II}/R_I = S_{II}$;
(d) the relative width of the runner L/R_I;
(e) the relative height of the centre of the runner above the sub-water level H_0/R_I;
(f) the angle of the centre of the guide tongue λ;
(g) the number of runner blades N;

(h) the angle of entry of the blades β_1;

(i) the angle of direction of the absolute flow defined by the guide channel α_0;

(j) the centre angle associated with the full opening condition ε;

(k) the angular coordinate value defining the position of the end point of the water flow control tongue in the r, φ coordinate system at full opening χ.

For notations, see the notations in Figure 3.; L is the length of the runner blade measured perpendicular to the blade.

The Bánki turbine shall be designed a) for an impact-free flow entering the runner (i.e., the operating condition $\psi_0 = \cot \alpha_0 - \cot \beta_1$ (Hajdú, 2022) is the design operating condition) and b) for the full opening condition of the turbine.

Using the value of the initial data (a) to (k), the main data of the Bánki turbine can be calculated using the equations listed below.

The power coming from the river:

$$P_D = \rho \, gQH_D \tag{9}$$

The size R_I and the value of the available head H can be determined iteratively using the following two equations. The size of the inlet surface $R_I \varepsilon \, L$ at the runner peripheral face affected by the inlet is given by the ratio of the volumetric flow rate Q through the runner at full opening divided by the radial (meridional) inlet velocity $c_{1m} = \sqrt{2gH} \sin \alpha_0$, and hence:

$$R_{I,i+1} = \sqrt{\frac{Q}{\varepsilon \, L/R_I \sqrt{2gH_i} \sin \alpha_0}} \tag{10}$$

From equation (1) in (Hajdú, 2022):

$$H_{i+1} = H_D - R_{I,i+1}(H_0/R_I + \sin \chi) \tag{11}$$

At the beginning of the iteration ($i = 0$) $H_0 = H_D$.

The inlet is impact-free if the runner speed in RPM is:

$$n_0 = \frac{30\sqrt{2gH} \sin \alpha_0}{R_I \pi} \psi_0 = \frac{30\sqrt{2gH}}{R_I \pi} (\cos \alpha_0 - \cot \beta_1) \tag{12}$$

The radius of the blade arc can be calculated from Figure 3 in (Hajdú, 2022):

$$R = \frac{R_I(1 - S_{II}^2)}{2\cos\beta_1} \tag{13}$$

Centre angle of the blade arc is:

$$\varphi_k = \pi - \beta_1 - \arctan\left(\frac{1 - S_{II}^2}{1 + S_{II}^2}\tan\beta_1\right) - \arctan\left(\frac{S_{II}R_I}{R}\right) \tag{14}$$

Length of the blade arc is: $L_k = R\phi_k$. Runner width is: $L = R_I(L/R_I)$.
The relative flow in the blade channels can be considered as a rectangular cross-sectional pipe flow. According to (Hajdú, 2022), the length of the pipe is: $L_{cs} = L_k N \frac{\varepsilon}{\pi}$ and the hydraulic diameter of the pipe is: $D_H = 4\frac{L\pi R_I}{LN + 2\pi R_I}$. The velocity of fluid flow in the pipe is: $\bar{w} = \sqrt{\frac{2gH}{S_{II}\sin\beta_1(1 + \cot^2\alpha_0)}}$. The Reynolds number of the pipe flow is: $Re = \frac{\bar{w}D_H}{\upsilon}$, $\upsilon = 10^{-6}\ m^2/s$.
Knowing the Reynolds number, the pipe friction coefficient λ_{cs} can be determined by a numerical approximation method taking into account that $\kappa = 0.407$. Knowing the pipe friction coefficient λ_{cs}, the friction loss factor is: $\zeta_V = \lambda_{cs}\frac{L_{cs}}{D_H}$. The contraction loss factor according to (Hajdú, 2022) is: $\zeta_K = \left(\frac{\varepsilon\sin(\varepsilon/2)}{2(1 - \cos(\varepsilon/2))} - 1\right)^2$.
The runner efficiency of the Bánki turbine runner in the operating condition ψ_0 is:

$$\eta_{jk}(\psi_0) = 1 - \frac{1 + (\psi_0 - \cot\beta_1)^2}{1 + \cot^2\alpha_0} - \frac{\zeta_K(1 + S_{II}^4\psi_0^2)}{S_{II}^2(1 + \cot^2\alpha_0)} - \frac{\zeta_V}{S_{II}\sin\beta_1(1 + \cot^2\alpha_0)} \tag{15}$$

The resulting efficiency in the operating condition ψ_0 is interpreted as the ratio of the runner power to the power coming from the river:

$$\eta_{resulting}(\psi_0) = \frac{P_{jk}(\psi_0)}{P_D} = \eta_{jk}(\psi_0)\frac{\rho\,gQH}{\rho\,gQH_D} = \eta_{jk}(\psi_0)\frac{H}{H_D} \tag{16}$$

The height difference between the centre of the runner and the sub-water level (Figure 3.) is: $H_0 = R_I(H_0/R_I)$. The radius of the circle delimiting the inside of the runner's bladed space is: $R_{II} = S_{II}R_I$. The radius of a circle concentric with the centre of the runner and representing the geometric location of the centres of the blade arcs

(Figure 3.) is: $R_{III} = \sqrt{R_{II}^2 + R^2}$. The angular coordinate φ_F (Figure 3.) of the point of rotation F of the control tongue (Figure 3.) in the coordinate system r, φ is:$\phi_F = \chi - \lambda$. The radial coordinate r_F of the rotation point F of the regulating tongue (Figure 3.) in the coordinate system r, φ is: $r_F = R_I e^{\lambda \tan \alpha_0}$.
Length of the regulating tongue (Figure 3.) is:

$$L_S = R_I \sqrt{1 + e^{2\lambda \tan \alpha_0} - 2e^{\lambda \tan \alpha_0} \cos \lambda} \tag{17}$$

The angle of the absolute flow leaving the runner is α_4 (as indicated in (Hajdú, 2022)). The following equations are obtained by taking into account equation (7) of (Hajdú, 2022) and equation $\beta_4 = \pi - \beta_1$:

$$\cot \alpha_4 = \psi + \cot \beta_4 = \psi - \cot \beta_1 = (\cot \alpha_1 - \cot \beta_1) - \cot \beta_1 = \cot \alpha_1 - 2 \cot \beta_1 \tag{18}$$

In the impact-free entry mode ($\psi = \psi_0$) $\alpha_1 = \alpha_0$ is valid, hence, according to the (18), $\cot \alpha_4 = \cot \alpha_0 - 2 \cot \beta_1$ is satisfied. This implies that the choice of the value pair $\alpha_0; \beta_1$ in the impact-free entry mode determines the direction angle α_4 of the absolute flow exit, and that the mode characteristic number ψ_p associated with the radial exit is:

$$\psi_p = \cot \beta_1 \quad (\alpha_4 = \pi/2, \qquad \cot \alpha_4 = 0) \tag{19}$$

If the choice of the value pair $\alpha_0; \beta_1$ satisfies the condition $\cot \alpha_0 = 2 \cot \beta_1$, then, according to the (19)

$$\psi_p = \cot \beta_1 = \psi_0 = \cot \alpha_0 - \cot \beta_1 \tag{20}$$

 is satisfied, i.e., the radial exit and impact-free entry occur in the same operating condition. It also follows from the above that, if $\alpha_0 = \beta_1/2$, then $\alpha_4 = \text{acot}(\cot \alpha_0 - 2 \cot \beta_1) < \pi/2$ is satisfied and the angle of exit deviates only slightly from $\pi/2$.
Baseline data chosen for the design example are:

$$H_D = 3\,[m], Q = 1\,[m^3/s], L/R_I = 4, R_{II}/R_I = \frac{2}{3}, \frac{H_0}{R_I} = 1.15, N = 20, \lambda = 70°$$

For the design, we choose $\alpha_0; \beta_1$ value pairs, where, based on (20), one β_1 value is assigned three different α_0 values for which the following equations are satisfied:

$$\alpha_0 = \text{acot}(2 \cot \beta_1) \rightarrow \alpha_4 = \text{acot}(\cot \alpha_0 - 2 \cot \beta_1) = \frac{\pi}{2}$$

$$\alpha_0 < \text{acot}(2 \cot \beta_1) \rightarrow \alpha_4 = \text{acot}(\cot \alpha_0 - 2 \cot \beta_1) < \frac{\pi}{2} \leftarrow \alpha_0 = \frac{\beta_1}{2}$$

$$\alpha_0 > \text{acot}(2 \cot \beta_1) \rightarrow \alpha_4 = \text{acot}(\cot \alpha_0 - 2 \cot \beta_1) > \pi/2 \leftarrow \alpha_0 = 1{,}1 \text{acot}(2 \cot \beta_1)$$
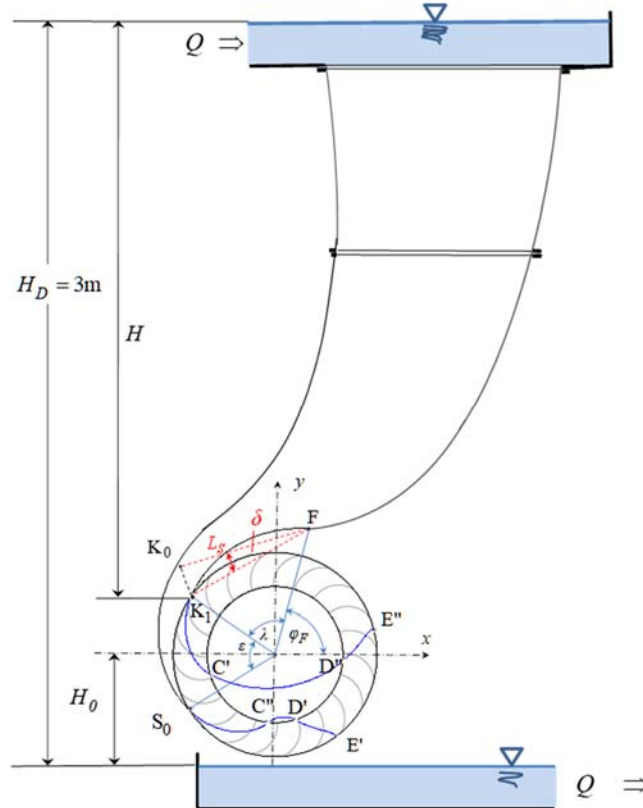
Figure 4. *Scale drawing of the Bánki turbine*

Given the data of the Bánki turbine variants using the different $\alpha_0; \beta_1$ value pairs, a decision can be made on the variant to be implemented. The results of the calculations are easy to review when the data are tabulated. The results of a sample calculation are shown in Table 1. In the calculation example, the data in Table 1 are used to select the variant „c" in the case of $\beta_1 = 20°$ for the Bánki turbine to be

implemented in order to achieve a high resulting efficiency, and the Bánki turbine is thus designed. Based on the data determined in the design, a scale plan of the Bánki turbine (Figure 4) and a shell diagram of the runner efficiency of the Bánki turbine runner (Figure 5) can be drawn.
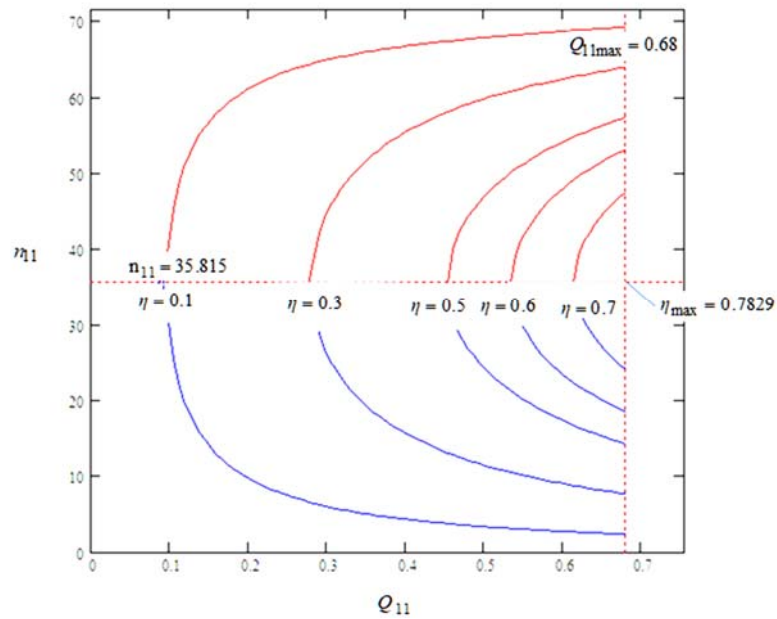
Figure 5. *Shell diagram of the runner efficiency of the Bánki turbine runner*

Table 1.
Calculated results

	a	b	c	a	b	c
$\beta_1°$	15			20		
$\alpha_0°$	7.5	7.631	8.394	10	10.314	11.346
$\varepsilon°$	45	47	55	56	59	68
$\chi°$	147	147	150	151	150	145
$\psi_t = \psi_0$	3.8637	3.7321	3.0450	2.9238	2.7475	2.2364

$\eta_E(\psi_0)$	0.9827	0.9824	0.9686	0.9689	0.9679	0.9512
$\alpha_4(\psi_0)°$	82.5000	90.0000	124.4911	80.0000	90.0000	117.0694
$\varphi_C°$	78.9424	76.8471	65.9123	62.4776	59.6713	51.5377
$\alpha_C°$	30.2141	31.0851	36.4613	37.5799	39.3152	45.1733
$\varphi_D°$	139.3705	139.0174	138.8349	137.6374	138.3016	141.8843
$(\varphi_D - \varphi_C)°$	60.4281	62.1703	72.9226	75.1598	78.6303	90.3467
$\varphi_E°$	183.4135	180.9651	169.8478	168.2273	166.0852	161.5342
$\varphi_{K2}°$	15.4135	14.9651	14.8478	15.2273	15.0852	14.5342
R_I m	0.6291	0.6075	0.5249	0.4719	0.4514	0.3986
H m	1.9339	1.9705	2.1339	2.2286	2.2551	2.3129
R_{II} m	0.4194	0.4050	0.3499	0.3146	0.3010	0.2658
R m	0.1809	0.1747	0.1510	0.1395	0.1334	0.1178
R_{III} m	0.4568	0.4411	0.3811	0.3441	0.3292	0.2907
$\varphi_K°$	92.4497	92.4497	92.4497	85.9439	85.9439	85.9439
L_k m	0.2919	0.2819	0.2436	0.2092	0.2002	0.1768
L m	2.5165	2.4299	2.0996	1.8875	1.8057	1.5946
$\varphi_F°$	77.0000	77.0000	80.0000	81.0000	80.0000	75.0000
r_F m	0.7389	0.7155	0.6286	0.5853	0.5638	0.5094
L_S m	0.7898	0.7640	0.6671	0.6135	0.5896	0.5287
$\Theta°$	66.3442	66.1137	65.0009	64.0709	63.4416	61.6672
$\varphi_{K0}°$	143.3442	143.1137	145.0009	145.0709	143.4416	136.6672
r_{K0} m	0.7035	0.6842	0.6126	0.5710	0.5559	0.5208
$\delta°$	6.2180	6.6287	8.6573	10.5396	11.6029	15.1030
L_{cs} m	1.4596	1.4721	1.4885	1.3019	1.3122	1.3356

D_H m	0.3665	0.3539	0.3058	0.2749	0.2630	0.2322
$\overline{w}$ m/s	1.9356	1.9877	2.2739	2.4046	2.4941	2.7753
Re	709393	703439	695337	661047	655917	644527
λ_{cs}	0.0152	0.0152	0.0152	0.0154	0.0154	0.0154
ζ_V	0.0604	0.0632	0.0741	0.0728	0.0768	0.0888
ζ_K	0.9491	0.9446	0.9244	0.9217	0.9132	0.8854
$\eta_{jk}(\psi_0)$	0.8330	0.8353	0.8340	0.7912	0.7931	0.7829
$P_{jk}(\psi_0)$ kW	15.8036	16.1478	17.4582	17.2965	17.5450	17.7626
n_0 f/p	47.1520	48.4379	52.3227	67.9381	69.2174	70.9942
$\eta_{resulting}(\psi_0)$	0.5370	0.5487	0.5932	0.5877	0.5962	0.6036
	a	**b**	**c**	**a**	**b**	**c**
$\beta_1\,°$	25			30		
$\alpha_0\,°$	12.5	13.124	12.5	13.124	12.5	13.124
$\varepsilon\,°$	65	70	65	70	65	70
$\chi\,°$	148	144	148	144	148	144
$\psi_t = \psi_0$	2.3662	2.1445	2.3662	2.1445	2.3662	2.1445
$\eta_E(\psi_0)$	0.9509	0.9484	0.9509	0.9484	0.9509	0.9484
$\alpha_4(\psi_0)\,°$	77.5000	90.0000	77.5000	90.0000	77.5000	90.0000
$\varphi_C\,°$	52.1815	48.6532	52.1815	48.6532	52.1815	48.6532
$\alpha_C\,°$	43.5580	46.3751	43.5580	46.3751	43.5580	46.3751
$\varphi_D\,°$	139.2975	141.4034	139.2975	141.4034	139.2975	141.4034
$(\varphi_D - \varphi_C)\,°$	87.1160	92.7503	87.1160	92.7503	87.1160	92.7503
$\varphi_E\,°$	162.4345	161.0120	162.4345	161.0120	162.4345	161.0120

φ_{K2} °	15.4345	15.0120	15.4345	15.0120	15.4345	15.0120
R_I m	0.3872	0.3636	0.3872	0.3636	0.3872	0.3636
H m	2.3495	2.3682	2.3495	2.3682	2.3495	2.3682
R_{II} m	0.2581	0.2424	0.2581	0.2424	0.2581	0.2424
R m	0.1187	0.1114	0.1187	0.1114	0.1187	0.1114
R_{III} m	0.2841	0.2668	0.2841	0.2668	0.2841	0.2668
φ_K °	79.5223	79.5223	79.5223	79.5223	79.5223	79.5223
L_k m	0.1647	0.1547	0.1647	0.1547	0.1647	0.1547
L m	1.5489	1.4543	1.5489	1.4543	1.5489	1.4543
φ_F °	78.0000	74.0000	78.0000	74.0000	78.0000	74.0000
r_F m	0.5077	0.4834	0.5077	0.4834	0.5077	0.4834
L_S m	0.5227	0.4956	0.5227	0.4956	0.5227	0.4956
Θ °	61.4249	60.2348	61.4249	60.2348	61.4249	60.2348
φ_{K0} °	139.4249	134.2348	139.4249	134.2348	139.4249	134.2348
r_{K0} m	0.5147	0.5030	0.5147	0.5030	0.5147	0.5030
δ °	15.8289	18.2592	15.8289	18.2592	15.8289	18.2592
L_{cs} m	1.1896	1.2030	1.1896	1.2030	1.1896	1.2030
D_H m	0.2256	0.2118	0.2256	0.2118	0.2256	0.2118
$\overline{w}$ m/s	2.7685	2.9159	2.7685	2.9159	2.7685	2.9159
Re	624521	617625	624521	617625	624521	617625
λ_{cs}	0.0155	0.0156	0.0155	0.0156	0.0155	0.0156
ζ_V	0.0819	0.0883	0.0819	0.0883	0.0819	0.0883
ζ_K	0.8951	0.8788	0.8951	0.8788	0.8951	0.8788
$\eta_{jk}(\psi_0)$	0.7386	0.7377	0.7386	0.7377	0.7386	0.7377

$P_{jk}(\psi_0)$ kW	17.0227	17.1388	17.0227	17.1388	17.0227	17.1388
n_0 f/p	85.7510	87.1758	85.7510	87.1758	85.7510	87.1758
$\eta_{resulting}(\psi_0)$	0.5784	0.5824	0.5784	0.5824	0.5784	0.5824

5. SUMMARY

Under the conditions of a circular curve of the runner blade (the tangent to the blade is radial at the inner boundary of the bladed space) and congruent relative flow, the geometry of the runner of the Bánki turbine can be designed and a scale drawing of the turbine installation can be prepared by applying the relationships summarized in the paper. Furthermore, the expected operating data of the designed turbine can be determined, including a shell diagram of the runner efficiency of the runner. Such a calculation has not been reported in the literature so far.

ACKNOWLEDGEMENT

REFERENCES

Bánki, D. (1920). *Energiaátalakulások folyadékokban* (2.. kiad.). Budapest: Franklin.

Czibere, T. (2009). Az el nem évülő Bánki-turbina létrehozója 150 éve született. *GÉP, 60*(3), 9-15.

Hajdú, S. (2022). Calculation of the flow generated in the runner of a Bánki turbine. *Design of Machines and Structures, 12*(1), 12-25. https://doi.org/10.32972/dms.2022.002

Mockmore, C., & Merryfield, F. (1949). The Banki Water Turbine. *Engineering Station Bulletin Series, 25*.

DEVELOPMENT OF A TEST BENCH TO SOLVE A SIMPLE LABYRINTH

PÁLMA KAPITÁNY[1] – MÁTÉ SZABÓ[2]

University of Miskolc, Robert Bosch Department of Mechatronics
3515, Miskolc-Egyetemváros
[1]palma.kapitany@uni-miskolc.hu, [2]szabo.mate1@student.uni-miskolc.hu
[1]https://orcid.org/0000-0001-6826-2371

Abstract: This paper deals with building an automatic test bench for detecting and solving a simple maze. There are many suitable sensors for detecting walls and ball, as find quick and stabile algorithm for deliver the ball to the target. Two servo motor are used to tilt the table of the maze. The first part of the paper shows the experiences of using OV7076 camera with Arduino Nano which was used for the first time to solve the problem. The final version of the maze solver contains a USB camera, an Arduino UNO platform, OpenCV and PyCharm software. Furthermore, paper reveals possibilities of decision-making-process and the direction of following research work.

Keywords: maze, OpenCV, PyCharm, ball labyrinth

1. INTRODUCTION

Nowadays one of the leading sectors is the development of self-driving vehicle (Almadhoun & Zhang, 2021), (Kosuru & Venkitaraman, 2023), the use of cooperative robots (Yan, Zeng, He, & Hong, 2023), (Yu, Tong, Xu, Dong, & Yang, 2021) and a wide range of autonomous decision-making devices. These kinds of tasks can serve convenience functions, help people, or operate autonomous systems, thus freeing up human resources and freeing people's time for creative work. In the case of such systems, sensor signals are used in a targeted manner, decisions are made in the light of the defined goal, and the necessary actuators are controlled. Many self-driving vehicles and autonomous system must solve a maze-situation, discover, and follow possible path (Mohammed, Al-Dabagh, & Rashid, 2023), (Suryani, Agustriana, Rakhmatsyah, & Pahlevi, 2023).

This article also presents an independent system, the stated goal of which is to be suitable for solving a simple ball maze, based on image processing, and to come to rest when the ball reaches the target. Section 2 deals with structure of ball maze solving system and shows the way of moving table of labyrinth, the 3D model of the plan was made in the Autodesk Inventor software.

Section 3 introduces the first solution that used an OV7670 camera and Arduino Nano development platform with ATmega328 microcontroller. Section 4 discusses elements and control of the final system. The solution includes USB camera used in OpenCV, cooperate with PyCharm to control two servo motors via Arduino Uno platform. Several algorithms are known, which can be used to get out of a labyrinth. In the case of the simple ball maze, reaching a target position is desirable, therefore the ball must be roll along the path leading to it.

2. STUCTURE OF BALL LABYRINTH SOLVING SYSTEM

The maze is placed on a double table, which contains two sheets. The top sheet holds the ball and the walls of the maze, at the ends a hinge is opposite to a servo motor, these two elements provide the attach to the bottom sheet. Figure 1 shows that if Motor-A is turn counter-clockwise, the left side of top sheet rises therefore the ball rolls direction from the left to the right. The speed of the ball depends on the size of the slope of the sheet. Motor-A can turn clockwise, when the arm of servo let the sheet under the horizontal, ball rolls direction from the right to the left. The bottom sheet connects to the ground via two hinges (Hinge-B) which are standing opposite to Motor-B. When both motors are used at the same, there is possible to roll the ball in any direction of the plane, also it could be holding the ball in one position. Table 1. presents these cases.
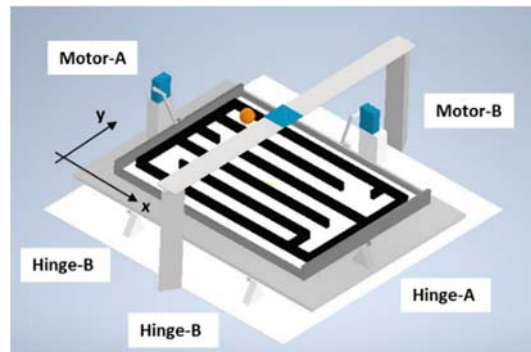

Figure 1. *Structure of ball labyrinth solving system (Szabó, 2023)*

In order to detect the ball and make decision to solve the maze problem, a camera is mounted onto the top of the system. The entire labyrinth can be checked via the camera unit. The planned structure included an electrical wiring for the microcontroller and the necessary electric power sources.

Table 1

Rolling direction of the ball depending on arms of servo motors

Motors	B: Up	B: Horizontal	B: Down
A: Up	x+ and y-	x+	x+ and y+
A: Horizontal	y-	ball in rest	y+
A: Down	x- and y-	x-	x- and y+

3. EXPERIENCE OF USING OV7670 CAMERA WITH ARDUINO NANO

In the first case, an OV7670 camera was used with Arduino Nano platform which includes ATmega328 microcontroller. The process was the following: wiring 18 pins of the camera to Arduino Nano pins, connection of pull-up and pull-down resistors, the use of voltage divider, common ground potential, data transfer cables and restart point. Thereafter the ATmega328 microcontroller is programmed in the Arduino IDE software on a personal computer. The program contains the following elements: setting of type of camera, numbers of scannable rows and columns, value of frames per second; next to checking a serial communication between the personal computer and Arduino Nano platform.

Furthermore, two servo motors were also connected to Arduino Nano platform by digital output pins in PWM mode, common ground GND potential pins, next to motors were wired to the necessary voltage supply.

In this phase of the research, it had dealt with building a faster connection between the microcontroller and the camera, as well as developing the software system during image processing. In addition, several methods and layouts were examined to create the wall of the labyrinth, as well as the sensitivity of the camera, which colours should be chosen as colour of the base plan, and which colour are contrasting for the walls and the ball.

OV7670 camera had 25° chief ray angle, therefore camera was placed the height of 700 mm from the sheet of labyrinth. Figure 2. part a) shows a photo about the real colours and lighting conditions, next to Figure 2. part b) illustrates the picture what

was produced by scanning of OV7670 camera, sent by ATmega328 via Arduino Nano platform to the personal computer.

a) Photo by reality   b) Scanned picture via OV7670
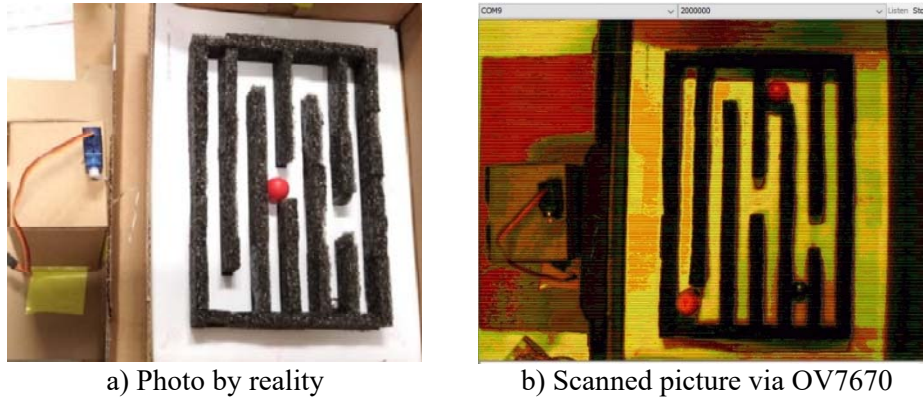
Figure 2. *Experience of using OV7076 camera with Arduino Nano*
(Szabó, 2023)

Figure provides that this scanned picture is not suitable for servicing the input data for maze-solving system. Direction of developing of maze-solving system was changed after this first planned and pilot construction. Main goal was in this case to build a control based on the microcontroller separately from a computer. Meaning of the second phase of the research was to make a control based on the personal computer.

4. DETAILS OF THE FINAL SOLUTION

As pointed out in the previous section, the control is planned to move from the microcontroller to a personal computer. In this way significantly more possibilities were revealed from the software support side. During the development, the OpenCV software came to the fore, first used in programming language C, thereafter the final program is written in Python language. Later, the use of PyCharm software became justified for the real-time control of the microcontroller which set position of the servo motors. In addition, changes were also made on the hardware side: instead of the Arduino Nano platform an Arduino Uno device was built into the system.
Figure 3 shows the placement of the camera which monitoring the labyrinth, the personal computer that runs the necessary software support, furthermore it contains the Arduino Uno, and the servo motors in the structure of labyrinth solver. The right side of Figure 3 shows the test bench, which was built from hard paper; OV7670 is

replaced with a general USB camera, and it is placed on top of structure. This construction was semi-closed box because of testing separately from the lights of environment.
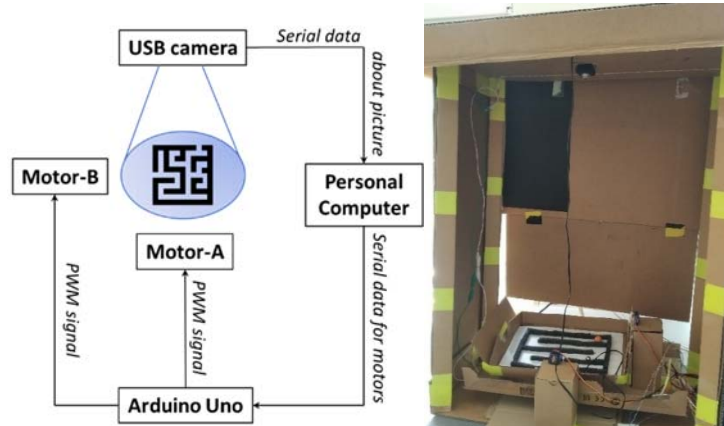
Figure 3. *Control of simple maze-solving system based on personal computer*

In this prototype lies a simple S-shaped labyrinth with a plastic ball and walls. Simple S-shaped track means that to get the ball to the target, it only requires a one-way tilt and a right-to-left roll. This control can be achieved by use two servo motors: one of them lifts the end of bottom sheet to tilt the table, the other lifts and let down the end of top sheet to roll the ball. White colour is used for the background of maze, dark grey (near to black) for the walls and orange for the ball.

The solver first needed to filter the image according to the colours mentioned above. After detecting the wall of the labyrinth, it surrounded its largest extent with a virtual rectangular contour and determined the coordinates of this rectangle. Using a similar procedure, the image processing system filtered the orange colour and identified the ball and can also characterize it with the coordinates of its centre.

After the separation by colour and the determination of the extents and the description with the coordinates, the decision-making and the control of the servo motors followed. The first mechanism for solving the simple S-shaped maze tilted the lower plate towards the target position in the upper left corner, while the second motor tilted it to the right if the ball was located on the left side, and vice versa, using X coordinate. Naturally where the wall was ended and a free path was opened to move in the direction of the goal, the ball continued on the s-shaped solving track all the way to the goal. Where the Y coordinate condition stopped the process and the ball remained in the top left target position.

Figure 4 shows the two tuned filters, with the help of which it identified the colour of the ball or the wall in the original image on the left, and cropped the image accordingly, and then the end shows the largest unit bounded by the filter, presented with a blue contour, and characterized by the centre coordinates.
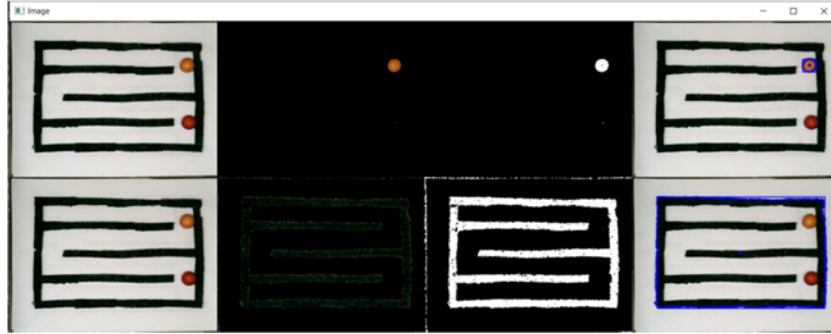
Figure 4. *Two implemented filter and detection of ball and wall (Szabó, 2023)*

Figure 4 and Figure 2 can be compared, there is a significant difference in the quality of the scanned image. It can also be cleared that the system was able to distinguish between shades of orange and red. A detailed description of the tuning of the filters can be found in the literature (Szabó, 2023), as well as how OpenCV and PyCharm were programmed to receive the camera image, process it and control the Arduino Uno development platform. The operation of the algorithms, the instruction content of the called command lines and the tuning of the parameters can also be read in that literature. The decision-making of the solver is currently based on the X and Y comparison of the centres of the largest contours identified with two different colours.
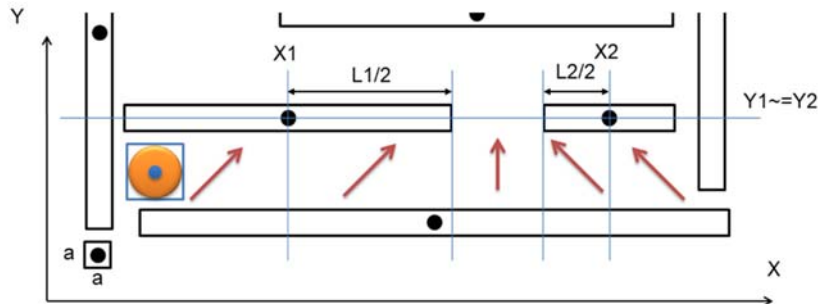
Figure 5. *The decision-making of the solver is currently further sub-units (Szabó, 2023)*

During the later development, it will be accessible by dividing the wall into further sub-units, and by making the gates in the walls a local goal: that the system is not only able to solve S-shaped labyrinths, but also general and medium difficulty mazes. Figure 5. shows a solution to take a decision process in direction X, it can be used in direction Y. This method requires an etalon, which is presented in Figure 5 by small letter a.

5. CONCLUSION

This article dealt with the design and construction of a maze-solving system capable of moving the ball from a single S-shaped maze to a predetermined target position. During the chapters, it reported on the results of an earlier research, which included a self-made image processing unit, which did not achieve the desired accuracy and repeatability. Paper shows on the work that moved the software requirement to other software that can be run on a personal computer and is able to communicate with motor-control development platforms.

Furthermore, it designates the direction of further development, which with the change brought about in the field of image processing: dividing the wall into further sub-units the specific shapes of the maze and leads the ball out of more than just a simple S-shaped maze.

REFERENCES

Almadhoun, R., & Zhang, W. (2021). Autonomous vehicle technology: A review of advancements, challenges, and future directions. *IEEE Transactions on Intelligent Transportation Systems, 22*(4), 2133-2149. https://doi.org/10.1109/TITS.2020.3005637

Kosuru, V., & Venkitaraman, A. (2023). Advancements and challenges in achieving fully autonomous self-driving vehicles. *World Journal of advanced Research and Reviews , 18*(1), 161-167. https://doi.org/10.30574/wjarr.2023.18.1.0568

Mohammed, I., Al-Dabagh, M., & Rashid, S. (2023). Path discovering in maze area using mobile robot. *TELKOMNIKA Telecommunication, Computing, Electronics and Control., 20*(2). https://doi.org/10.12928/telkomnika.v20i2.19408

Suryani, V., Agustriana, K., Rakhmatsyah, A., & Pahlevi, R. (2023). Room cleaning robot movement using A* algorithm and imperfect maze. *JURNAL INFOTEL, 15*(1), 75-81. http://doi.org/10.20895/infotel.v15i1.901

Szabó, M. (2023). Automata golyólabirintus megoldó tervezése. *BSc. szakdolgozat*. Miskolci Egyetem.

Yan, X., Zeng, Z., He, K., & Hong, H. (2023). Multi-robot cooperative autonomous exploration via task allocation in terrestrial environments 17:1179033. *Frontiers Neurorobot, 17*. https://doi.org/10.3389/fnbot.2023.1179033

Yu, J., Tong, J., Xu, Y., Dong, H., & Yang, T. (2021). SMMR-explore: submap-based multi-robot exploration system with multi-robot multi-target potential field exploration method. 8779-8758. https://doi.org/10.1109/ICRA48506.2021.9561328

SURFACE MODIFICATION METHODS OF PLASTIC COMPONENTS PRODUCED BY ADDITIVE MANUFACTURING: A REVIEW

PÉTER FICZERE[1] – NOÉMI LÁSZLÓ[1,2]

[1]*Budapest University of Technology and Economics,*
Department of Railway Vehicles and Vehicle System Analysis,
1111, Budapest, Műegyetem rkp. 3.
[2]*H-ION Kutató, Fejlesztő és Innovációs Kft. – SEM Labor*
[1]*ficzere.peter@kjk.bme.hu,* [2]*noemi.laszlo@h-ion.hu*
[1]*https://orcid.org/0000-0003-3207-5501,* [2]*https://orcid.org/0000-0002-8912-2711*

Abstract: Additive manufacturing (AM) is a widely used process today, especially for the production of complex parts that cannot be produced with traditional material removal technologies. However, in the case of components produced by 3D printing, due to the specifics of the technology, poor surface quality is often to be expected. From the point of view of the product and production process, the so-called textural characteristics, surface roughness can be considered the most critical component. The surface of the part produced by 3D printing must meet several criteria (e.g., mechanical, physical, tribological, aesthetic, etc.). This article discusses the possibilities of surface modification of polymer parts produced with additive manufacturing technology, focusing on their effects on surface roughness. The paper also deals with the features suitable for describing the surface texture of 3D printed parts and their role in the characterization of printed parts.

Keywords: surface treatment, plastic, additive manufacturing, surface roughness

1. INTRODUCTION

Nowadays, polymer-based materials (Kmetz & Takács, 2020) are successfully used in many industrial fields, and they can replace metal, - and ceramic materials in an increasing proportion in several sectors, starting from electronics to the food industry, up to the car, - and aircraft industry (Tuazon, Custodio, Basuel, Reyes, & Dizon, 2022), (Lim, Le, Lu, & Wong, 2016), (Elakkad, 2019), (Raheem, 2012).
The use of high-performance technical plastics in the automotive industry is constantly increasing, thanks to their favourable properties, such as their chemical

inertness, mechanical properties, economical production, and the ability to be extensively modified with additives (Patil, Patel, & Purohit, 2017), (Kim, et al., 2023), (Sadiku & Ibrahim, 2007). The surface properties of polymers often do not meet the requirements for scratch resistance, wettability, adhesive behaviour, and friction. For this reason, additional surface treatments are often required to achieve the desired properties while maintaining the characteristics of the volume. A possible grouping of surface treatment methods is illustrated in Figure 1.

Surface modifications of polymers can basically be classified into two groups: procedures involving the addition of material and procedures involving the removal of material. Processes involving the addition of material are the various coating processes (e.g., PVD, CVD), which can improve wear resistance, powder spraying (Heinze, Menning, & Paller, 1995), (Medel, et al., 2010).

It is also possible to influence the surface roughness without adding any material. Etching, for example, can be considered such a treatment. In these cases, the etchant used during etching mostly means acids and alkalis that are solvents for the polymer itself. In the case of polylactic acid (PLA), which is most often used during additive processing, NaOH can be such an etchant: Schneider (Schneider, et al., 2020) highlighted during his research that in the case of PLA printed parts, increasing the milling time causes an increase in surface roughness. At the same time, it can also be observed that the surface roughness of the printed material is initially smaller, on average 4.5 nm, but after a four-hour treatment, this increases to about 160 nm, thanks to erosion.
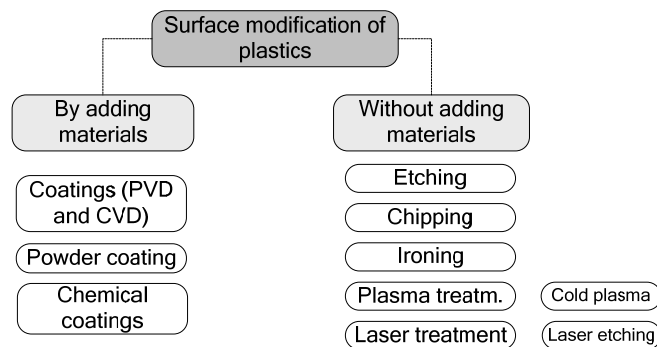
Figure 1. *Classification of surface modification technologies in case of AM plastic part*

Mechanical surface modifications include sanding, abrasive treatments, and barrel finishing. CNC milling is also widely used to improve surface roughness, which can be used well for simple geometries, but less so for undercut parts. chemical treatments are widely used, due to their many advantages, such as the absence of geometrical limitations and the speed of the process, but at the same time, the harmful effects of chemicals (e.g., health-damaging or toxic fumes) must be taken into account.

According to the relevant literature, in the case of polymers, surface and bulk eroding material types can be distinguished. Figure 2 illustrates the differences between each type of erosion.
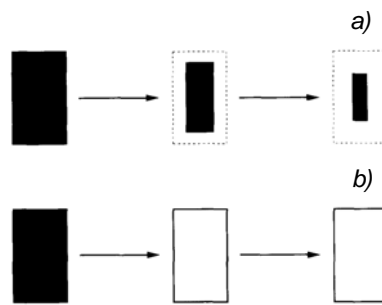
Figure 2. *Schematic diagram of the process of bulk and surface erosion a) surface b) bulk erosion (Schneider, et al., 2020)*

In the case of surface erosion, material loss occurs only from the surface of the polymer during a given application. In this case, a decrease in size can be observed, but at the same time they retain their original geometric shape. (On the other hand, during bulk erosion, the erosion is not only limited to the surface.)

2. SURFACE ROUGHNESS AND AM

The surface texture of a part produced by 3D printing can be described with several components, such as waviness, profile, and surface roughness (Figure 3). The individual components and their reasons and explanations are summarized in Table 1. (Golhin, Tonello, Frisvad, Grammatikos, & Strandlie, 2023).
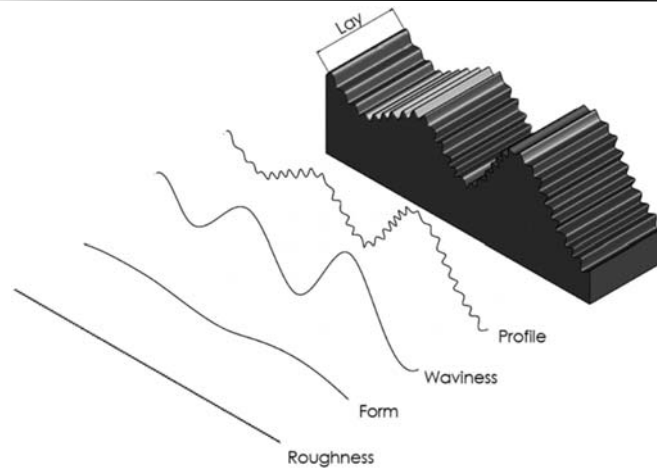
Figure 3. *Texture components of 3D manufactured parts (Golhin, Tonello, Frisvad, Grammatikos, & Strandlie, 2023)*

Table 1.
Texture components and interpretation of AM parts
(Golhin, Tonello, Frisvad, Grammatikos, & Strandlie, 2023)

Texture component	Reason/Interpretation
Profile	can be ascribed to layer-by-layer manufacturing
Waviness	Machine vibration; Poor adhesion of layer; Thermal distortion; mechanical deformation during post-processing
Form	Poor performance of manufacturing system
Roughness	generated by surface irregularities due to printing and material removal errors

Among the components mentioned above, surface roughness can be considered the most critical component from the point of view of characterizing the texture. The surface roughness can most generally be described with the roughness parameter Ra, however, there are studies that indicate that the parameters Sa (average area surface) and Sq (area root mean squared height) may also be suitable for characterizing the surface roughness, since these parameters are less sensitive to the measurement conditions such as sampling and evaluation length.

3. SURFACE MODIFICATION METHODS WITHOUT MATERIAL ADDING

3.1. Plasma and laser treatments, etching

Cold plasma is the most suitable for surface modification of polymers (Károly, Klébert, & Kalácska, 2015), (Berczeli, Hatoss, & Kókai, 2022). In this case, the atoms are at room temperature, while the temperature of the electrons is much higher, even an order of magnitude higher. The high electron temperature also results in significant chemical reactivity, which is why it is well suited for the treatment of bulk materials and even parts produced by additive processing (Figure 4).
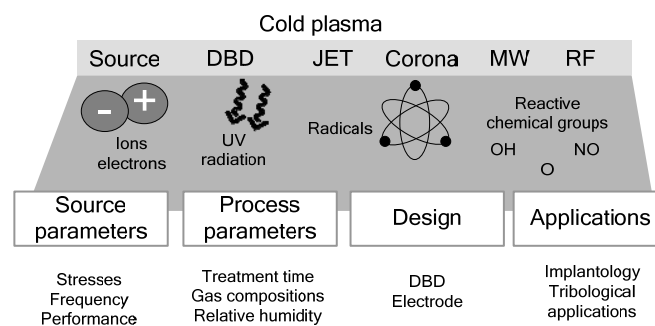
Figure 4. Cold plasma treatment: process, parameters, and typical applications

Several plasma sources can be used to create the plasma state, such as a corona discharge or a plasma beam.

The reduction of technological costs leads the development of plasma treatments in the direction of the use of cold plasma. There are many applications where low-pressure plasma cannot be substituted. Nevertheless, there are applications where the use of non-equilibrium cold plasma at atmospheric and higher pressures has significant advantages.

In their research, Károly et al. (Karoly, et al., 2019) investigated the effect of cold plasma treatment on the tribological and adhesion properties of PTFE and PA 66 materials. The treatment was carried out for periods of 24 and 800 h. Based on the tests carried out, it can be concluded that in the case of these materials, the cold plasma treatment influenced the surface composition, and the treatment resulted in oxidation of the surface. Tribological tests on various materials have shown that, under low and medium loads, PA has significantly higher wear resistance than PTFE.

Regarding the friction coefficient, it can be established that the treatment time affects its change. It can be observed that 24 h of plasma treatment results in a decrease in the coefficient of friction, while after 800 h the coefficient of friction increases.

Most literature uses the roughness parameter Ra to quantify the surface roughness, which does not consider the morphological characteristics of the surface, since profiles of different shapes but with the same arithmetic mean peak height and valley depth show the same Ra values. In terms of surface roughness, the roughness parameter Rq can best characterize the change in roughness since this parameter is much more sensitive to the presence of roughness peaks and valleys.

Based on the research carried out by Mandolfino (Mandolfino, Lertora, & Gambaro, 2014), it can be concluded that - in the case of PP - the roughness of the surface increased significantly because of the treatment. The phenomenon can be explained by changes in the mechanical properties of the joints.

The change in roughness can also be explained (Kostov, Nishime, Castro, & Toth, 2014) in the case of this treatment by the fact that the radicals in the plasma gas collide with the polymer chains in the uppermost layers, which can thus split. Chain scission can result in the formation of low molecular weight oligomers, which must be removed from the surface, thus influencing changes in surface topography. This so-called material removal process results in an effect similar to etching, which is responsible for the change in surface roughness.

During his research, Hegemann (Hegemann, Brunner, & Oehr, 2003) investigated the effects of plasma treatments on adhesion and surface characteristics in the case of PC and EPDM materials. In his research, he analysed the effect of reaction gases (He and Ar) on the friction coefficient. In his research, Hegemann discussed the friction coefficient at the atomic, micro, and macroscopic levels. Accordingly:

- the friction coefficient interpreted at the atomic level is based on dissipative mechanisms and can be defined as the sliding of atoms on each other.
- at the microscopic level, friction means the relative displacement of two interacting surfaces;
- at the macroscopic level, the friction factor is the ratio of the friction force and the load force.

During the examinations performed, the coefficient of friction of the various polymers under given test conditions (treatment parameters – 20 minutes treatment time, 300 W power and 0.2 mbar pressure) resulted in a reduction of the friction coefficient. Increasing the treatment time caused a further decrease in the friction factor. However, when the plasma treatment was performed 1 month later, it no longer caused a significant reduction in the friction factor.

Zhang (Zhang, Häger, Friedrich, Song, & Dong, 1995) plasma-treated PEEK, PEEK+8% PTFE, and PEEK+10% PTFE+10% carbon fibre materials to characterize the tribological properties. The treatments were performed in Ar gas, with treatment parameters controlled (treatment time: 1-5 minutes, voltage: 0.8-1.3 kV). The tribological tests were performed with a steel ring antibody. The tests carried out showed that the values of the sliding friction coefficient and the specific wear factor were significantly reduced, especially in the case of the PEEK-steel ring tribological pair. The average friction coefficient value

Decreased from 0.42 to 0.23. At the same time, in the case of samples that underwent plasma treatments, a different wear mechanism took place than in the case of untreated samples.

At the same time, the research points out that the plasma treatment can also affect the degree of crystallinity of the polymer, which can result in an increase in strength and hardness. This can be explained, among other things, by the presence of intermolecular binding forces in the crystalline phase, which lead to the formation of oriented chains (Balani, Verma, Agarwal, & Narayan, 2015).

One of the relatively new methods of improving surface quality is laser polishing, which - unlike traditional polishing processes - is more suitable for reducing the surface roughness of additively manufactured parts but does not involve component or tool wear (Mushtaq, Iqbal, Wang, Khan, & Petra, 2023).

By using laser technology, the Ra surface roughness can be reduced by up to 68-70% for PLA parts produced by FFF processing. With the help of continuous lasers, a constant and stable beam can be produced, with a constant power level, and therefore can also be used for cutting and welding. At the same time, with laser technologies – especially in the case of plastic parts – it must be considered that the beam (due to the longer exposure times) can cause thermal damage to the part. The solution can be the use of pulse lasers, which can be used to emit the beam with short pulses, with a higher peak value and a lower average power level. The short duration of the laser pulse enables a higher peak power to be achieved, without component failure caused by thermal damage.

During laser polishing (Figure 5), the laser beam is directed at the surface of the part, where it melts the material on a closed surface. The focal length affects the energy density and the amount of material removed, which determines the spot size. A smaller focal length results in a smaller spot size and a higher energy density, but at the same time results in less efficient material removal, which can cause an increase in the surface roughness Ra.
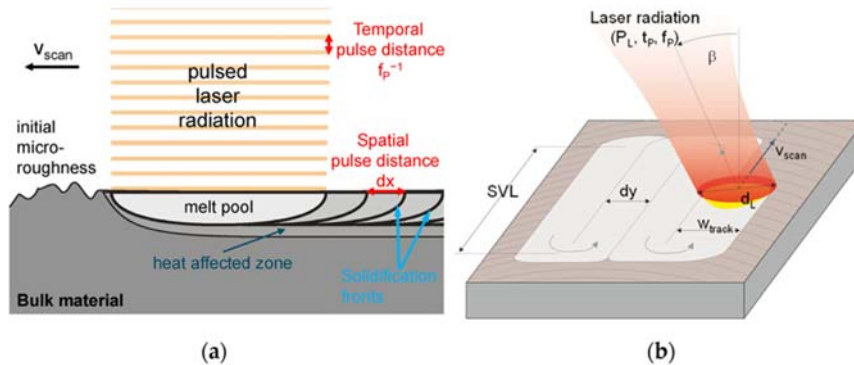
Figure 5. *Schematic illustration of laser polishing procedure*
a) pulsed laser operation with melt pool b) laser radiation
(Mushtaq, Iqbal, Wang, Khan, & Petra, 2023)

The surface quality and aesthetic appearance of plastic parts can be improved by laser polishing. At the same time, the technology is sensitive to the parameter settings, because incorrect settings can cause damage or destruction of the component due to the heat effect zone that occurs. Another problem can be the use of low beam energy, which results in the part being left untreated. During Mushtaq's research, he investigated the effect of laser polishing on the mechanical properties and surface quality of PLA parts produced by 3D printing. Based on the performed optimization experiments, it can be concluded that the mechanical properties (elastic modulus, tensile strength) can be significantly improved by determining the optimal laser scanning parameters (Mushtaq, Iqbal, Wang, Khan, & Petra, 2023).

Surface roughness can also be reduced with chemical treatments. The basis of the method is the choice of a chemical that is the solvent of the polymer to be treated. In the case of ABS, for example, dimethyl ketone-based solvents can be used with good efficiency to reduce roughness (Galantucci, Lavecchia, & Percoco, 2010). Lavecchia (Lavecchia, Guerra, & Galantucci, 2021) reduced the surface roughness of PLA parts produced with FFF technology by ethyl acetate treatment, the applied treatment time was 180 and 360 s. It can be concluded that even with a lower ethyl acetate concentration and a shorter treatment time, a significant (about 70%) reduction in roughness can be achieved, increasing the treatment time shows a significant decrease in the surface roughness values.

3.2. Roughness reduction with surface layers

Coating is a procedure often used to modify the surface roughness of bulk materials. The selection of the appropriate coating system depends on several parameters, such as the physical-chemical characteristics of the polymer, the porosity, surface characteristics and wetting ability of the bulk material (Zigon, Kariz, & Pavlic, 2020), (Khosravani, Zolfagharian, Jennings, & Reinicke, 2020), (Young, et al., 2016).

It should be noted that the coating of polymers –due to the specific properties of polymers (e.g., hydrophobic surface)– is only possible by using appropriate, mostly PU, acrylic or polyvinyl acetate based coatings (Zigon, Kariz, & Pavlic, 2020).

In their research, Zigon et al. (Zigon, Kariz, & Pavlic, 2020) investigated the effect of various coatings (waterborne acrylic coating – CW-B, solvent borne alkyd coating – CS-B and ABS diluted in acetone – C-ABS) on the surface roughness of ABS, PLA and PLA-W test specimens manufactured with FDM technology. was investigated. The individual test specimens were prepared by sanding to improve the adhesion of the coating. The test results of surface roughness measurements are presented in the following figure.
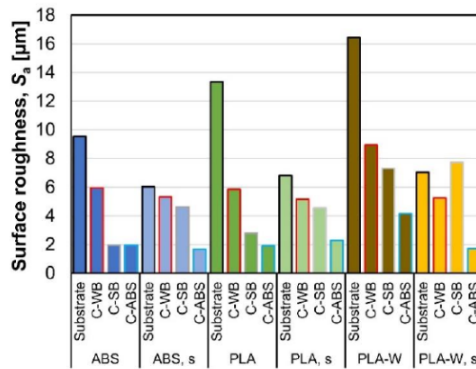
Figure 6. *Sa surface roughness parameters in case of different substrate materials (ABS, PLA and PLA-W) and coatings (CW-B, CS-B and C-ABS), s: sanded (Zigon, Kariz, & Pavlic, 2020)*

Based on the results of the surface roughness measurements, it can be concluded that the highest surface roughness can be observed in the case of the unpolished PLA-W specimens, while the smallest was determined in the case of ABS. It should be noted that both the layer thickness and the filling method have a significant effect on the surface roughness of 3D printed parts, while the printing speed does not affect it. By

applying the CW-B coating, the surface roughness of the unpolished specimens decreased by about 50%, while the roughness reduction can also be observed in the case of the polished substrate, but to a much lesser extent (19%). In the case of the C-ABS coating, a 79% reduction in roughness can be observed, which can be explained, among other things, by the presence of the acetone solvent in the coating, which presumably also partially dissolved the substrate material. In general, surface roughness can be reduced with higher solids content coatings (Zigon, Kariz, & Pavlic, 2020).

In the case of polymers, a metal coating can also be detached on the surface by combining painting and laser treatment. In his research, Yung (Young, et al., 2016) developed a treatment method in which the surface of the 3D printed part is treated with malachite-containing acrylic paint, and then transformed into a copper layer by laser treatment, through photochemical processes. The structure of malachite is illustrated in Figure 7. In the molecule, the copper ions are connected only with oxygen ions. If the energy of the photon is high enough, copper (II) ions are split from the copper-oxygen bond and are transformed into copper (0) through homolysis.
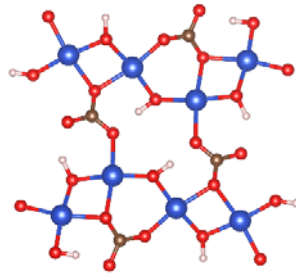
Figure 7. *Common structure of malachite (Crystallography 365, 2023)*

DLC (diamond like carbon) coatings are ceramic super hard coatings used for metallic materials, but they are also valid for polymer components to improve tribological performance (Marian, et al., 2023). The interpretation scheme of DLC coating is shown in Figure 8.

The DLC coating is a metastable form of amorphous carbon formed largely of sp3-hybrid carbon atoms,

The structure of DLC coating films moving from the substrate to the top of the coating, can be divided into three zones:

- – the components of the surface substrates are mixed with carbon.
- – the real DLC layer with sp3 bonds

– the more graphitic thin surface layer (Laszlo, 2021), (Bewilogua & Hofmann, 2014).
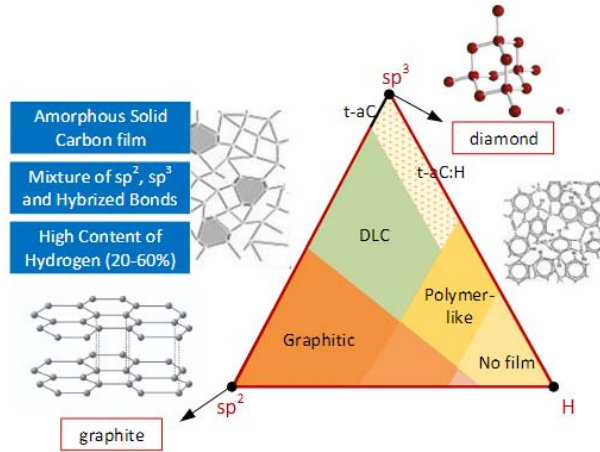
Figure 8. *Interpretation scheme of DLC coatings: amorphous carbon: a-C; amorphous carbon with tetrahedral structure: ta-C; amorphous carbon + hydrogen: a-C:H; tetrahedral amorphous carbon + hydrogen: ta-C:H*
(Casiraghi, Robertson, & Ferrari, 2007)
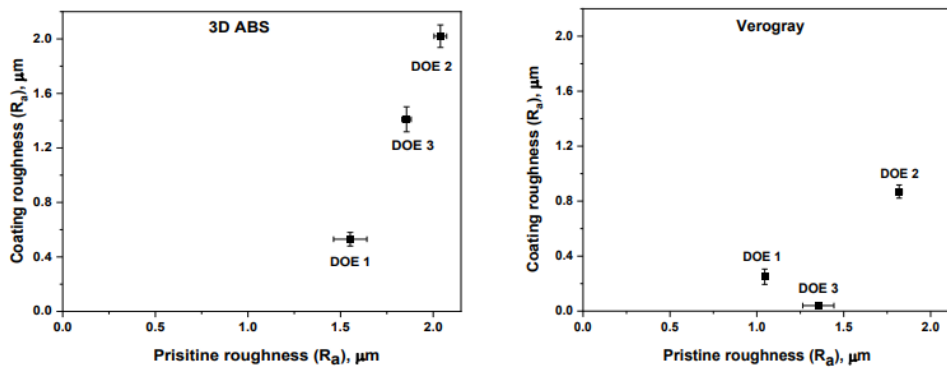
Figure 9. *Ra surface roughness of reference (uncoated) and coated ABS and Verogray 3D printed plastic parts (Ficzere, 2023)*

In the case of 3D printed parts exposed to wear, the friction conditions are determined by several parameters, such as hardness or surface roughness. During his research, Dangnan (Dangnan, 2021) dealt with the separation and testing of single-layer DLC coatings deposited by microwave-assisted PECVD process, in the case of ABS and Verogray (a type of modelling materials) material grades. In the case of the layers separated at a low temperature (45°C), in comparison with the surface roughness Ra of the reference substrate, a significant decrease in roughness can be observed in all cases. Figure 9 shows that the decrease in surface roughness is most significant in the case of ABS.

Depositing a surface layer without adding material during printing, so-called ironing is also possible. Ironing is a surface modification related to the printing process. The essence of the process is that after printing, the nozzle passes over the top layer - at the temperature used for printing - without adding material or with the addition of minimal material, because of which the surfaces merge better, the layer is more compact, the gaps are much better filled, while the surface roughness decreases (Ficzere, 2023).

Alzyod (Alzyod, Takács, & Ficzere, 2023) examined the effect of ironing post-processing on surface roughness, on specimens produced from PLA, using FDM technology, with regard to the examination of the effects of ironing parameters (ironing speed, ironing distance and volume flow). He investigated the determination of surface roughness using traditional, contact, and optical (non-contact) methods, and compared the results of these tests. The results show that the ironing process can lead to a significant reduction of the surface roughness, and that the surface roughness can be further reduced by optimizing the parameters.

4. CONCLUSION

The purpose of this research is to review the surface treatment and modification processes that help improve the surface quality of polymer parts, with regard to surface modifications suitable for reducing surface roughness.

In this paper, the most frequently used surface modification procedures and their most important characteristics were systematized and reviewed.

In addition to the conventional post-processing processes (e.g., cutting, grinding), various coating systems are now gaining ground, with the help of which not only the surface roughness can be reduced, but also –in the case of a given tribological system– the tribological performance of the part can be increased.

Although the individual treatments may already be suitable for reducing the surface roughness, in the future it may be advisable to calculate and examine the effect on the roughness by combining these procedures.

At the same time, it may also be worthwhile to deal with the quantitative characterization of surface roughness in the future: currently, most research examining the relationship between 3D printing and roughness characterizes the parts with the surface roughness Ra, however, this is a 2D characteristic that strongly depends on the test orientation used during the test (i.e., in which direction the measurement takes place on a given layer), a result closer to reality can be obtained by applying a 3D roughness measurement parameter.

REFERENCES

Alzyod, H., Takács, J., & Ficzere, P. (2023). Improving surface smoothness in FDM parts through ironing post-processing. *Journal of Reinforced Plastics and Composites*. https://doi.org/10.1177/07316844231173059

Balani, K., Verma, V., Agarwal, A., & Narayan, R. (2015). Chapter A1 - Physical, Thermal, and Mechanical Properties of Polymers. In *Biosurfaces: A Materials Science and Engineering Perspective* (pp. 329-344).

Berczeli, M., Hatoss, B., & Kókai, E. (2022). Surface treatment of polymer matrix nano-composites for adhesion enhancement by cold plasma., (pp. 1-9). https://doi.org/10.1088/1757-899X/1246/1/012028

Bewilogua, K., & Hofmann, D. (2014). History of diamond-like carbon films -From first exper-iments to worldwide applications. *Surface & Coatings Technology, 242*, 214-225. https://doi.org/10.1016/j.surfcoat.2014.01.031

Casiraghi, C., Robertson, J., & Ferrari, A. (2007). Diamond-like carbon for data and beer storage. *Materials Today,, 10*(1-2), 44-53. https://doi.org/10.1016/S1369-7021(06)71791-6

Crystallography 365. (2023, 11 01). Retrieved from Crystallography 365 web site: https://crystallography365.wordpress.com/2014/11/11/common-beauty-malachite/

Dangnan, F. (2021). Enhancing additively manufactured polymers through functional diamondlike carbon coatings. *PhD thesis*. University of Leeds.

Elakkad, A. (2019). 3D Technology in the automotive industry. *International Journal of Engineering Research & Technology, 8*(11), 248-251. https://doi.org/10.17577/IJERTV8IS110122

Ficzere, P. (2023, szeptember 15). *A vasalási eljárás paraméter-változásának hatása a felületi érdességre FFF el-járással készített additív gyártás esetén.* (N. J. Egyetem, Director) Országos Additív Ipari Tudományos Konferencia és Workshop, Kecskemét.

Galantucci, L., Lavecchia, F., & Percoco, G. (2010). Quantitative analysis of a chemical treatment to reduce roughness of parts fabricated using fused deposition modeling. *CIRP Annals, 59*(1), 247-250. https://doi.org/10.1016/j.cirp.2010.03.074

Golhin, A., Tonello, R., Frisvad, J., Grammatikos, S., & Strandlie, A. (2023). Golhin, A., Tonello, R., et. al.: Surface roughness of as-printed polymers: a compre-hensive review. *The International Journal of Advanced Manufacturing Technology, 127*, 987-1043. https://doi.org/10.1007/s00170-023-11566-z

Hegemann, D., Brunner, H., & Oehr, C. (2003). Plasma treatment of polymers for surface and adhesion improvement. *Nuclear Instruments and Methods in Physics Research Section B: Beam Interactions with Materials and Atoms, 208*, 281-286. https://doi.org/10.1016/S0168-583X(03)00644-X

Heinze, M., Menning, G., & Paller, G. (1995). Wear resistance of PVD coatings in plastics processing. *Surface and Coatings Technology, 74-75*(2), 658-663. https://doi.org/10.1016/0257-8972(95)08352-9

Karoly, Z., Kalácska, G., Sukumaran, J., Fauconnier, D., Kalácska, Á., Mohai, M., & Klébert, S. (2019). Effect of Atmospheric Cold Plasma Treatment on the Adhesion and Tribological Properties of Polyamide 66 and Poly(Tetrafluoroethylene). *Materials, 12*(4), 1-14. https://doi.org/10.3390/ma12040658

Károly, Z., Klébert, S., & Kalácska, G. (2015). Hidegplazmák alkalmazása polimerek felületmódosítására. *Polimerek, 1*(5), 147-152.

Khosravani, M., Zolfagharian, A., Jennings, M., & Reinicke, T. (2020). Structural perfor-mance of 3D-printed composites under various loads and environmental condition. *Polymer Testing, 91*, 1-9. https://doi.org/10.1016/j.polymertesting.2020.106770

Kim, D., Lim, J., Jung, D., Oh, W., Kyeong, J., Kwon, S., & Lee, S. (2023). Thermal and mechanical properties of polymeric materials for automotive applications using

molecular dynamics simulation 36. *Materials Today: Communication, 36*, 1-12. https://doi.org/10.1016/j.mtcomm.2023.106529

Kmetz, B., & Takács, Á. (2020). Demand for recycling filament in 3D printing. *Design of Machines and Structures, 10*(2), 65-72. https://doi.org/10.32972/dms.2020.016

Kostov, K., Nishime, T., Castro, A., & Toth, A. (2014). Surface modifica-tion of polymeric materials by cold atmospheric plasma jet. *Applied Surface Science, 314*, 367-375. https://doi.org/10.1016/j.apsusc.2014.07.009

Laszlo, N. (2021). Investigation of Adhesion Behaviour of Different Underlayered DLC Coated Cold Forming Tool Steel. *U.Porto Journal of Engineering, 7*(2), 60-68. https://doi.org/10.24840/2183-6493_007.002_0008

Lavecchia, F., Guerra, M., & Galantucci, L. (2021). Chemical vapor treatment to improve surface finish of 3D printed polylactic acid (PLA) parts realized by fused filament fabrication, , 2021, 7, 65, p.65-75,. *Progress in Additive Manufacturing, 7*(1), 65-75. https://doi.org/10.1007/s40964-021-00213-2

Lim, C., Le, K., Lu, Q., & Wong, C. (2016). An overview of 3D printing in manufacturing, aerospace, and automotive industries. *IEEE potentials, 35*(4), 18-22.

Mandolfino, C., Lertora, E., & Gambaro, C. (2014). Effect of Cold Plasma Treatment on Sur-face Roughness and Bonding Strength of Polymeric Substrates. *Key Engineering Materials, 611-612*, 1483-1493. https://doi.org/10.4028/www.scientific.net/KEM.611-612.1484

Marian, M., Zambrano, D., Rothammer, B., Waltenberger, V., Boidi, G., Krapf, A., . . . Grützmacher, P. (2023). Combining multi-scale surface texturing and DLC coatings for improved tribological performance of 3D printed polymers. *Surface and Coating Technology, 466*, 1-8. https://doi.org/10.1016/j.surfcoat.2023.129682

Medel, F., Martinez-Nogues, V., Mariscal, M., Endrino, J., Krzanowski, J., Yubero, F., & Puértolas, J. (2010). Tribological performance of DLC coatings on UHMWPE. *Journal of Physics: Conference Series*, 1-9. https://doi.org/10.1088/1742-6596/252/1/012006

Mushtaq, R., Iqbal, A., Wang, Y., Khan, A., & Petra, M. (2023). Advancing PLA 3D Printing with Laser Polishing: Improving Mechanical Strength, Sustainability, and Surface Quality. *Crystals, 13*(4), 1-17. https://doi.org/10.3390/cryst13040626

Patil, A., Patel, A., & Purohit, R. (2017). An overview of Polymeric Materials for Automotive Applications. *Materials Today: Proceedings, 4*(2), 3807-3815. https://doi.org/10.1016/j.matpr.2017.02.278

Raheem, D. (2012). Application of plastics and paper as food packaging materials - An overview. *Emirates Journal of Food and Agriculture, 25*(3), 177-188. https://doi.org/10.9755/ejfa.v25i3.11509

Sadiku, R., & Ibrahim, D. (2007). *Polyolefin Fibres - Structure, Properties and Industrial Applications* (2. ed.). (S. Ugbolue, Ed.) Science Direct. https://doi.org/10.1016/B978-0-08-1

Schneider, M., Fritsche, N., Puciul-Malinowska, A., Balis, A., Mostafa, A., Bald, I., . . . Taubert, A. (2020). Surface Etching of 3D Printed Poly(lactic acid) with NaOH: A Systematic Approach. *Polymers, 12*(8), 1-16. https://doi.org/10.3390/polym12081711

Tuazon, B., Custodio, N., Basuel, R., Reyes, L., & Dizon, J. (2022). 3D printing technology and materials for automotive application: a mini-review. *Key Engineering Materials, 913*, 3-16. https://doi.org/10.4028/p-26o076

Young, W., Sun, B., Huang, J., Jin, Y., Meng, Z., Choy, H., . . . Wong, W. (2016). Photochemical Copper Coating on 3D Printed Thermoplastics. *Scientific Reports,, 6*, 1-7. https://doi.org/10.1038/srep31188

Zhang, R., Häger, A., Friedrich, K., Song, Q., & Dong, Q. (1995). Study on tribological behaviour of plasma-treated PEEK and its composites. *Wear, 181-183*(2), 613-623. https://doi.org/10.1016/0043-1648(95)90177-9

Zigon, J., Kariz, M., & Pavlic, M. (2020). Surface Finishing of 3D-Printed Polymers with Selected Coatings. *Polymers, 12*(12), 1-14. https://doi.org/10.3390/polym12122797

Zlamal, T., Mrkvica, I., Szotkowski, T., & Malotova, S. (2019). The Influence of Surface Treatment of PVD Coating on Its Quality and Wear Resistant. *Coatings, 9*(7), 1-12. https://doi.org/10.3390/coatings9070439

DESIGN METHODOLOGY IN THE FRENCH ARCHITECTURE

CÉDRIC LAURENT[1] – ÁGNES TAKÁCS[2]

University of Miskolc, Institute of Machine and Product Design
H-3515, Miskolc-Egyetemváros
IPSA, Institute of Polytechnic Science and Aeronautics
40 bd Marquette 31000, Toulouse, France
[1]cedric.laurent@ipsa.fr, [2]takacs.agnes@uni-miskolc.hu
[1]https://orcid.org/0009-0007-4412-2164, [2]https://orcid.org/0000-0002-3210-6964

Abstract: In this paper the authors are focusing on Jean Nouvel, a significant member of the French architect society. The aim of this research was to analyse the most remarkable elements of the architect's life's work: what kind of notable results he created, what ideas did he apply, etc. The authors tried to make a comparison between the design ways of architecture and mechanical engineering.

Keywords: design methodology, design process, mechanical engineering, architecture

1. INTRODUCTION

Design methodology is a structured approach to solving problems that are related to design in any discipline or field. It involves a range of methods, techniques, and tools that are customized to suit the specific needs of a particular design project.
The goal of design methodology is to ensure that the design process is integrated with the broader context of the problem, taking into consideration the needs of users, the feasibility of manufacturing and production, cost, and the constraints of resources. It focuses on a systematic, iterative approach that involves multiple stages, such as research, ideation, prototyping, testing, evaluation, and refinement. Design methodology is relevant in all fields, such as product design, architecture, graphic design, fashion design, engineering, and web design. It is an essential tool for designers to develop innovative and effective solutions that can meet the needs of the users and stakeholders. (Mahmoodi, 2001)

Figure 1. *Design process*
https://discoverdesign.org/handbook
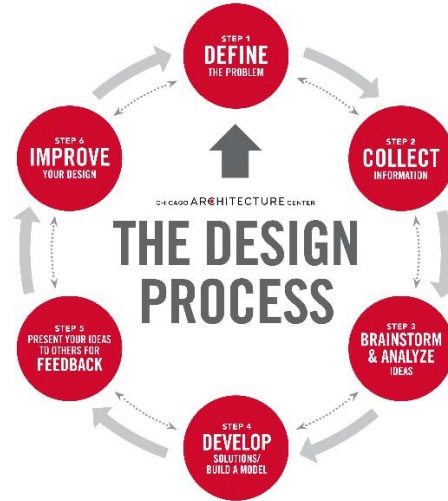
Design methodology is not a new concept, and it has been used by designers for centuries, even before we had a name for it. In fact, throughout history, designers have used a structured approach to solve design problems. For example, architects in ancient Rome used a method for designing buildings that included studying the site, sketching initial designs, testing the design, and ultimately building the structure.

In this paper we will be focusing on France where designers have a rich history of using design methodology to create innovative and effective solutions. So one of the notable French designers of the 21st century Jean Nouvel will be introduced. Nouvel's approach involves extensive research, investigation, and analysis of the site and context of a project. He then creates several design concepts, tests them, and refines them until he arrives at the best solution.

2. JEAN NOUVEL

Jean Nouvel is a celebrated French architect renowned for his avant-garde and innovative architectural designs. Born in Fumel, France, in 1945, he has had a profound impact on the world of architecture with his distinctive and futuristic creations.

His work is characterized by a relentless pursuit of originality, incorporating elements such as light, transparency, and complex geometries. Nouvel's architectural designs have received widespread recognition and numerous awards, solidifying his reputation as a visionary in the field. Thanks to his work he won the Pritzker Architectural Prize in 2008 and has also a place in the pantheon of architectural superstars. His career spans several decades and has left an indelible mark on the global architectural landscape.

2.1. Playing with the light

Artists usually really like to play with the light. In many artistic masterpieces we can see, how the author applied the perfect light. Of course, when we admire these significant works of art amazed, we cannot even imagine how and how long did it take until the artist found the proper solution. Maybe we can have a slight idea of it when we start to study the light space modulator of László Moholy-Nagy. Watching the modulator during its operation it came clear that the changing of the shades is continuous, and every shade can be strange and individual even in an unexpected moment. Nouvel does not make an exception to the rule: he played a lot with the light in his creations. In the next paragraph two significant buildings are introduced, on which a play of light and shadow with motifs from the Arab world appears. In case of the third example playing with the light is also in the focus, but from an other point of view. In this case, Nouvel uses an idea of the theory that ancient Egyptians would use some kind of mirrors for letting the sunlight into the pyramids. According to scientists these were just ideas on how the ancient people could illuminate the interior of the pyramids, as they could not have such a good quality of mirror that would made it possible to forward the sunlight.

2.1.1. The Louvre Abu Dhabi

Let us begin with one of Nouvel's most notorious works. Born out of an intergovernmental agreement signed between France and the United Arab Emirates on the 6th of March 2007, the Louvre Abu Dhabi is the first universal museum in the Arab world. It brings the Louvre name to Abu Dhabi and presents both ancient and contemporary works of historic, cultural, and sociological interest from around the world. The Louvre Abu Dhabi is one of his most internationally recognized and celebrated projects because of its complexity and its innovative design.

The particularity of this building is its vast, seemingly floating dome as we can see in Figure 2. This dome is an intricate lattice structure made of eight different layers of stainless steel and aluminium, with patterns inspired by traditional Arabic

geometric designs. The design of the dome is a reference to the interplay of light and shadow in traditional Islamic architecture.

Figure 2. *The Louvre Abu Dhabi*
https://medias-distribution.lab.arte.tv/photos/0914434-cropped.jpg
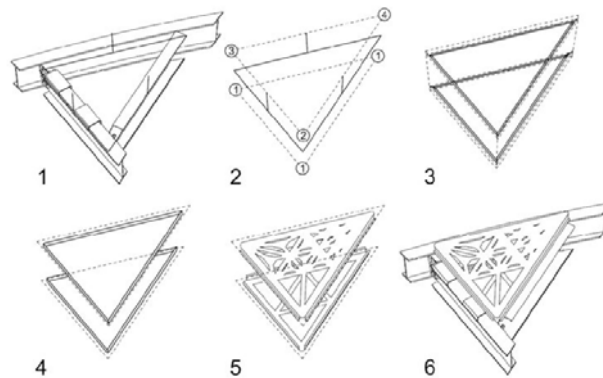
1-centre lines and orientations for a single triangle with the substructure, 2-the panels' bounding planes and density values, 3-the panel's mounting strips, 4-the panel's flanges, 5-the completed panel, 6-the panel on the substructure

Figure 3. *Different layers of the dome (Wortmann & Tuncer, 2017)*

The innovative design of the dome allows dappled sunlight to filter through the intricate pattern, creating a "rain of light" effect inside the museum. (Imbert, et al., 2012) (Tourre & Miguet, 2009) This unique play of light and shadow throughout the day provides a constantly changing and dynamic experience for visitors. The interlocking geometric patterns in the dome create a mesmerizing effect, resembling rays of sunlight passing through palm leaves. It's as if you are walking under a forest canopy while exploring the museum's interior.

2.1.2. Institute of the Arab World

Another very well-known of Nouvel's work is in Paris and is called the Institute of the Arab World. Its construction lasts 3 years and the building opened in 1987 for a purpose of representations about Arab world, art, and culture.
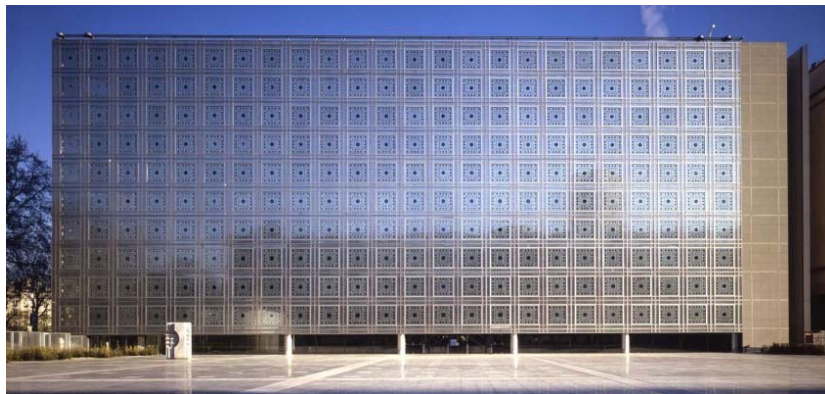
Figure 4. *Arab World Institute south facade*
https://architizer-prod.imgix.net/mediadata/projects/272010/c85761a2.jpg

The most distinctive feature of the Arab World Institute is its innovative mechanical facade. The building's southern facade is covered in a complex system of mechanical diaphragms called ***Moucharabieh***, which automatically adjust to control the amount of sunlight entering the building.
This dynamic feature was inspired by traditional Islamic latticework, but it adds a contemporary and functional element to the structure. The mechanical diaphragms on the building's exterior open and close to regulate the interior light levels. This design is not only a functional response to the intense sunlight in Paris but also a symbolic representation of the merging of technology and traditional Arabic architectural elements. The building's innovative design and cultural significance have

earned it recognition in the architectural world. It has received several architectural awards and is often cited as one of Jean Nouvel's most iconic works.

Figure 5. *Moucharabieh representation*
https://wikiarquitectura.com

2.1.3. One Central Park in Sydney

One Central Park is a landmark mixed-use development located in Sydney, Australia, known for its innovative and environmentally conscious design. Designed by Jean Nouvel in collaboration with the Australian firm PTW Architects, the complex features a striking and unique design characterized by its incorporation of extensive vertical gardens, cantilevered ***heliostat***, and innovative sustainability features.

Figure 6. *One Central Park in Sydney*
https://www.archdaily.com

The mixed-use of this building means that it encompasses a variety of functions and purposes within the same complex. It promotes a sense of community and convenience, as residents have access to a wide range of services and facilities without walking a long distance from their homes.

The particularity of One Central Park in Sydney lies in its innovative and groundbreaking approach to incorporating greenery and sustainable features into urban architecture. In our approach of Nouvel's work, one feature of this building is interesting for us, the Heliostat System. In Nouvel's way to play with the light, here is an innovative concept again. The cantilevered heliostat, the floating square that we can see in Figure 6, on the apartment tower is a unique feature. This system uses a series of pivoting mirrors to track the sun's movement and reflect sunlight into the park and public spaces below. It's an innovative way to harness natural light and reduce the need for artificial lighting, promoting energy efficiency. The mirrors were included to alleviate concerns of overshadowing the site's own and the city's public domain.

2.2. Complexity of architecture

Architects should work together with the experts of other areas, like acousticians in case of music halls like theatres and opera houses. In case of Nouvel two significant buildings are introduced in the following: the Philharmonic of Paris, and the Opera House of Lyon. Both buildings were created to enjoy musical performances, so the acoustics of the performance hall are the most important part of the building from the point of view of engineering. But as these buildings are the homes of art, the appearance must be also very important, and the building itself should represent the highest level of art. So, Nouvel, as an architect, had a hard mission to find the balance among the limits of the acoustics, the art, and of course the limits of the architecture. (Venturi, 1977)

2.2.1. Philharmonic of Paris

As it was said before, an example to represent Nouvel's work in collaboration with acousticians is the Philharmonic of Paris which is mainly a concert hall in Paris. The design of this concert hall is to provide the best sound experience for listeners and emphasize the sounds of each instrument.

The Philharmonic of Paris is known for its bold and dynamic architectural design. The building features a series of irregularly shaped, aluminium-clad volumes that appear to jut out at various angles, giving it a sense of movement and contemporary flair. This design was created to express the energy and dynamism of the music performed within.

Figure 7. *Philharmonic of Paris' outside*
https://philharmoniedeparis.fr/themes/custom/pdp_theme/images/discover/philharmonie/carousel-intro/01_VUE-EXTERIEURE-FACADE-W-BEAUCARDET-08.jpg

Figure 8. *Balconies inside the Philharmonic of Paris*
https://i.pinimg.com/564x/f3/7c/97/f37c97bdaee1b5ede347bce99eacb4a0.jpg

The concert hall inside the Philharmonic is renowned for its exceptional acoustics, making it a world-class venue for classical and contemporary music performances. The Philharmonic of Paris is not only a concert hall but also serves as a cultural centre, housing exhibition spaces, educational facilities, and rehearsal studios. The Philharmonic of Paris represents a fusion of architecture and music, with its striking design and emphasis on acoustic excellence. It's a significant cultural and

architectural landmark in Paris and is often considered one of Jean Nouvel's prominent works.

Sir Harold Marshall was the principal acoustics consultant for the Philharmonic of Paris. His contribution was essential for the design of the concert hall. As a world-renowned expert in musical acoustics, he worked with Jean Nouvel to ensure that the concert hall provided exceptional acoustics for musicians and the audience. Marshall was tasked with designing the acoustical features of the hall, including the seating and balcony layout, the height and position of the ceiling, the shape of the walls, and the reverberation of the hall. His work helped create a world-class concert hall with top-quality acoustics.

2.2.2. Opera Nouvel

Jean Nouvel's work on the Opera Nouvel in Lyon in France, is a significant architectural project that transformed the city's opera house. Completed in 1993, the Opera Nouvel represents a modern and innovative approach to the renovation and expansion of a historic cultural institution. Jean Nouvel's design involved the addition of a contemporary structure to the existing historical opera house, blending the old and the new as we can see in Figure 9. This juxtaposition of modern architecture with a historic building is a signature aspect of Nouvel's approach.

Figure 9. *Opera of Lyon*
https://www.rue89lyon.fr/2014/02/24/lopera-de-lyon-architecture-hybride-entre-rouge-noir/

The exterior of the new addition is characterized by a striking glass and metal facade. The glass surfaces allow natural light to flood into the building and create a sense of transparency, providing a contrast to the solid, historical structure. The interior of the Opera Nouvel features a modern and minimalist design. It includes a grand entrance hall, a large auditorium, and various public spaces. The design aims to create a sense of openness and contemporary elegance. Nouvel also kept the previous style for corridors and main rooms of the building as we can see in Figure 10.

Jean Nouvel paid careful attention to the acoustics of the opera house. The design incorporates state-of-the-art acoustic features to ensure that the space is suitable for world-class musical and theatrical performances. And by this, he worked with Victor Peutz, a Dutch acoustician. Peutz was tasked with improving the acoustics of the opera house, which had been criticized for its poor sound quality. Peutz's contributions to the project were significant and he made several changes to the design of the opera house to enhance its acoustics.
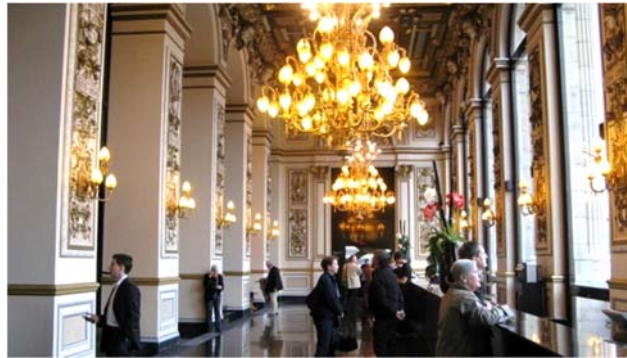
Figure 10. *Inside the Opera*
https://i0.wp.com/operasandcycling.com/wp-content/uploads/2017/10/b_7040.jpg?w=780&ssl=1

He revised the shape of the stage and the orchestra pit to improve sound projection and clarity. He also made changes to the seating arrangement and the shape of the hall to reduce echo and reverberation, which further improved the sound quality. Additionally, Peutz used his innovative computer simulation techniques to create a 3D model of the entire hall, which allowed him to test different acoustic solutions virtually before applying them for real.

Peutz's contributions to the Lyon Opera House were highly praised, and the opera house has since become known for its excellent acoustics. His work established a new standard for opera house acoustics, and he has been recognized as one of the pioneers of modern acoustic design.
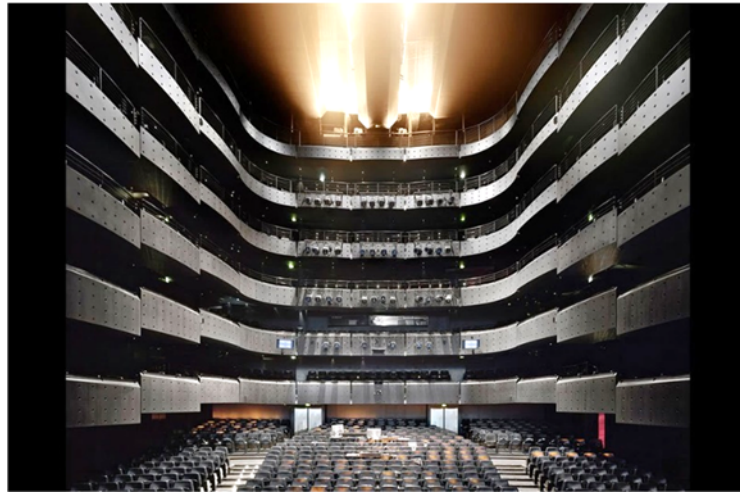
Figure 11. *Concert room inside the Opera*
https://assets.classicfm.com/2015/28/opra-nouvel-lyon-france-2014--1436882456-view-1.jpg

The Opera Nouvel has received recognition and awards for its architectural excellence, particularly in its ability to successfully blend historical and modern elements. This building is an example of Jean Nouvel's ability to transform and revitalize cultural institutions through innovative architectural design. His work on the opera house is characterized by a commitment to preserving the historical character of the building while infusing it with a sense of modernity and functionality, creating a space that continues to be a hub for cultural performances and events.

2.3. Nouvel as a world-famous architect

Jean Nouvel is renowned all around the globe. He created a lot of buildings in many different countries. Each building comes with a unique design and functions. Nouvel, thanks to his work, has implanted a few of his art or a few of his approach in a lot of buildings that are famous nowadays. We can find some of his work in Australia, France or the United Arab Emirates as we've seen but also in Spain, the USA, Denmark, the UK, China, Quatar, Austria and even more.

3. SUMMARY

In this paper some of the significant buildings of Nouvel were shown. In the paragraph Playing with the light, some of those buildings were introduced, in which Nouvel used special elements for creating an interior that has got special shades of

the sunlight. He used traditional Arabic patterns, which give organic shades on the inner surfaces, of course besides shading of the building. Through the examples of the Philharmonic of Paris, and Opera of Lyon it was proven that the interrelationship among architecture, space and acoustics make Nouvel's buildings as complex as a machine, or a product can be. The main concept of this paper was to find points in the architectural design that could have got a similar pair in mechanical engineering design. This is not an easy task, because of the two types of design are much different. The work of Nouvel could be a very good source for this, as it is extremely rich, as he designed so many significant buildings all around the word. He also applies the latest results of the CAD as well, which also could be a connection point between the architectural design and the mechanical engineering design. In further research on the basis of the here presented results a precise list of engineering applications should be defined.

REFERENCES

Imbert, F., Frost, K., Fisher, A., Witt, A., Tourre, V., & Koren, B. (2012). Concurrent Geometric, Structural and Environmental Design: Louvre Abu Dhabi. In L. Hesselgren, S. Sharma, J. Wallner, N. Baldassini, P. Bompas, & J. Raynaud (Ed.). *Advances in Architectural Geometry.* Vienna: Springer. https://doi.org/10.1007/978-3-7091-1251-9_6

Mahmoodi, A. S. (2001). *The design process in architecture - A pedagogic approach using interactive thinking.* Leeds, UK: The University of Leeds.

Tourre, V., & Miguet, F. (2009). A light-based parametric design model - The application of the inverse lighting in the design of the Louvre Abu Dhabi museum. In T. Tidafi, & T. Dorta (Ed.), *PU Montreal*, *Joining Languages, Cultures and Visions - CAADFutures 2009*, pp. 786-799. Canada.

Venturi, R. (1977). *Complexity and Contradiction in Architecture.* New York: The Museum of Modern Art.

Wortmann, T., & Tuncer, B. (2017). Differentiating parametric design: Digital workflows in contemporary architecture and construction. *Design Studies*, 173-197. https://doi.org/10.1016/j.destud.2017.05.004

CAD MODELLING OF A MILLING INSERT

TAMÁS MAKKAI[1] – FERENC SARKA[2]

[1]University of Miskolc, Institute of Manufacturing Science
H-3515, Miskolc-Egyetemváros
[2]University of Miskolc, Institute of Machine and Product Design
H-3515, Miskolc-Egyetemváros
[1]tamas.makkai@uni-miskolc.hu, [2]ferenc.sarka@uni-miskolc.hu
[1]https://orcid.org/0000-0002-7840-9856, [2]https://orcid.org/0000-0003-3136-4248

Abstract: There is often a problem when using FEM software where the tool geometry needs to be specified for the cutting simulation, one or more dimensions are not known. In the article, we present how and with what methods we determined these unknown dimensions, how we created the three-dimensional CAD model of the cutting insert as input data for the FEM software. We report our experience gained during the measurement and model creation process.

Keywords: CAD model, milling insert, FEM analysis

1. INTRODUCTION, DESCRIPTION OF THE PROBLEM

The processes, during cutting, take place relatively quickly. For this reason, their observation with optical and mechanical devices is difficult, and even more difficult in the case of rotating tools. The deformation of the material, the formation of chips, the course of mechanical and energetic characteristics over time are important characteristics of the milling process. In addition to the difficulties of observation, the expensive tools and workpieces are also arguments for which the use of computer simulation software is extremely beneficial instead of real experiments. In many cases, the finite element method is used for the analysis in several mechanical engineering problem like in (Sarka, 2022), (Alzghoul, Sarka, & Szabó, 2022), (Jálics, 2017). Standard tools can be found in the simulation software, and it is also possible to use unique tool geometry. The dynamic effects of enter cutting was investigated with the position change (axial and radial rake angle) of an octagonal milling insert

with FEM simulation by Sztankovics (Sztankovics, 2019). For this, he had to create the insert geometry individually in the software. Karpuschewski et al. investigated the changes in the components of temperature, torque, power and cutting force during face milling using two types of inserts (Karpuschewski, et al., 2018). During the FEM simulation, in addition to the chip ratio, the angles of the tool (lead angle, axial and radial rake angle) were also variable. Borysenko et al. analysed the chip formation and the components of the cutting force with FEM simulation during face milling with a special tool (Borysenko, Karpuschewski, Welzel, Kundrák, & Felhő, 2019). In the case of indexable inserts, their manufacturers usually provide several geometric characteristics in their catalogues (e.g., insert thickness, edge length), but there are some geometric dimensions that are not specified (e.g., rake angle, edge radius). If we want to use a tool of which geometrical data is unknown and cannot be found in the catalogue (e.g., older insert types), then these must be determined, and the CAD model must be created so that we can insert it into the simulation software. Hard turning experiments were carried out with a new octagonal cubic boron nitride (CBN) insert (Kundrák, Sztankovics, & Gévai, 2019) by Kundrák et al. For the FEM simulation, the rake angle of the insert was determined with a coordinate measuring machine. Felhő carried out face milling FEM simulation experiments to determine the components of the cutting force, he worked with a circular insert (Felhő, 2020). The edge radius of the insert is one of the important factors of chip separation, and he presented a new method to measure it. The measurement was carried out on a three-dimensional surface roughness measuring machine, and the value of the edge radius determined by this method was used in the FEM software, so that the simulation could be carried out such a tool geometry that is closer to the reality.

2. THE BRIEF HISTORY OF THE CUTTING INSERTS

After the First World War, diamond became very expensive, so the industry started looking for another material to replace it (as proper material as drawing die for non-sag tungsten wire). Scientists tried to convert the brittle carbide material into a plastic material by sintering, similar to tungsten. Schröter's first attempts to sinter WC (tungsten carbide) with Ni additions produced variable results. Then they experimented with the addition of cobalt powder, which proved successful, this metal-ceramic alloy was suitable for the production of drawing tools for tungsten wires. Schröter applied for a patent for his discovery, which received the number DRP 420.689 (Patent No. DE420689C, 1923). Then the patent went to the German Krupp Company, they started the production of the new material under the name WIDIA (Wie Diamant=WIDIA, like diamond). The development of carbides has led to a

continuous increase in the production and use of carbide raw materials (Ortner, Ettmayer, & Kolaska, 2014). Pálmai et al. (Pálmai, Dévényi, & Szőnyi, 1991) presented in detail the characteristics of carbides, their production methods, and the manufacturing processes of various types of carbide tools. In the early days, carbide inserts were attached to the tool shank by soldering. The worn insert could be resharpened by grinding. The growing trend of automation in metalworking and the spread of numerical control led to the development of indexable inserts. Indexable inserts with complicated geometry and tight tolerances were thrown away and replaced with a new one after they were worn out. This made it possible to reduce tool costs and save human work and time spent on resharpening. The Swedish company Sandvik started the production of carbide tools in 1942 under the name Coromant. In 1943, the first carbide metalworking tools were manufactured. Ceramic cutting materials also appeared in the 1950s. In 1957, scrapers became the first tools to have mechanically clamped indexable inserts or throw-away inserts. This year, the T-Max holder appeared, and the use of indexable insert led to an increase in productivity. The world's first surface-coated carbide insert appeared, and in 1969 the heat-resistant gamma coating (GC) was introduced, which further increased the performance of the inserts with its heat resistance (Sandvik, 2023.). In addition to ceramics are also used in insert form. The more expensive raw materials, such as diamond (PCD) and cubic boron nitride (CBN), were placed on tip of the carbide inserts (as carriers).

3. BRIEF DESCRIPTION OF THE FEM PROGRAM

For the simulation analysis of cutting processes, we can choose software from several companies. In the following, we present what input data can be entered for a face milling simulation in the Third Wave AdvantEdge software. First, it is advisable to specify the geometric dimensions of the workpiece, i.e., width, length, and height, as well as the characteristics of the finite element simulation for the workpiece. In addition to the geometry, we can specify a standard material, but it is also possible to set individual material characteristics. The next step is to specify the geometry of the tool. We can choose to work with standard or unique edge geometry. When using a standard insert, you must select the exact type of insert, specify the cutter diameter and the number of edges. The position of the insert can be specified with various tool angles, these are the radial and axial rake angle, the relief angle, and the lead angle. The edge radius and the width of the insert (Tool Width) must also be entered. In case of individual insert design, the shape of the insert must be drawn in the base plane in the program's own editor. It is also possible to draw a unique cutting edge. This is followed by the selection of the material of the insert, if necessary, we can

specify the number, thickness, and material of the coatings. After specifying the characteristics of the workpiece and the tool, the parameters of the cutting process must be specified. In the case of face milling, these are the spindle speed, feed per tooth, axial depth of cut, initial temperature, rotation angle, friction coefficient and cooling-lubrication characteristics. Finally, the parameters characteristic of the finite element mesh used during the simulation must be set. As a result of the simulation, we get the values of the following output characteristics over time: forces in the x, y and z directions interpreted in the Cartesian coordinate system, tangential and radial forces for a single cutting edge, cutting power, torque and temperature, the von Mises stress that can be measured on the tool, shear stress, pressure and temperature, as well as temperature rate, von Mises stress, plastic deformation rate and temperature that can be determined in the root of the chip. The software can also provide animation about chip formation. The results can be analysed immediately with the software called TecPlot, but they can also be saved in text format for further processing with an external application.

4. DETERMINATION OF THE GEOMETRIC DIMENSIONS OF THE INSERT

The examined insert was a parallelogram-shaped milling insert that can be attached to a face milling head. Its enclosure dimensions can be easily measured, even with a vernier calliper. However, the geometry of the boundary surfaces of the insert is much more complicated than it can be determined with simple hand tools. In order to build the CAD model of the insert, we had to perform several different types of measurements. We present them in the next two points.
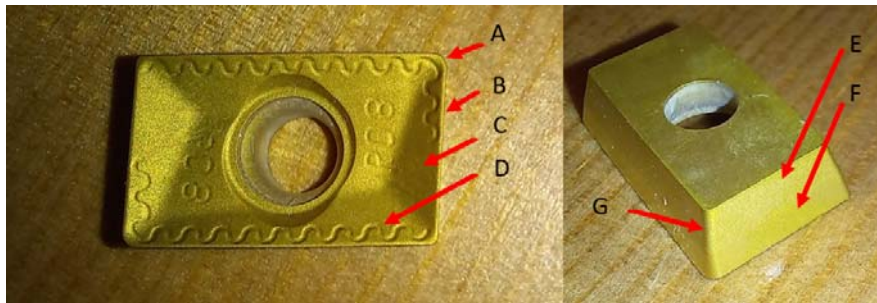
Figure 1. *Photo of the insert, marking the individual surfaces to be modelled*

We were able to determine the dimensions of the three inclusions of the insert using traditional hand measuring tools: its length, width and height. These are respectively 15.4 mm, 9.6 mm and 4 mm. The manufacturer of the insert specified the rounding

radius of the cutting tip as 0.8 mm (it is also written on the insert), which we accepted when building the CAD model. The rounding radius is a very important data in terms of the roughness and the shape of the machined surface. The following figure shows a photo of the insert (Figure 1). On this, we marked the individual surfaces, the modelling of them will be covered in the following points.

We continued the determination of the geometry with microscopic examination. We used a Zeiss Discovery v12 microscope and the accompanying ZEN software for the measurements. The measurements were performed at 20x magnification. Before the measurement, calibration was performed with a 2 mm thick gauge block. Using the microscope, we determined the width of the land. The value of the width was between 0.14-0.17 mm (Figure 2).
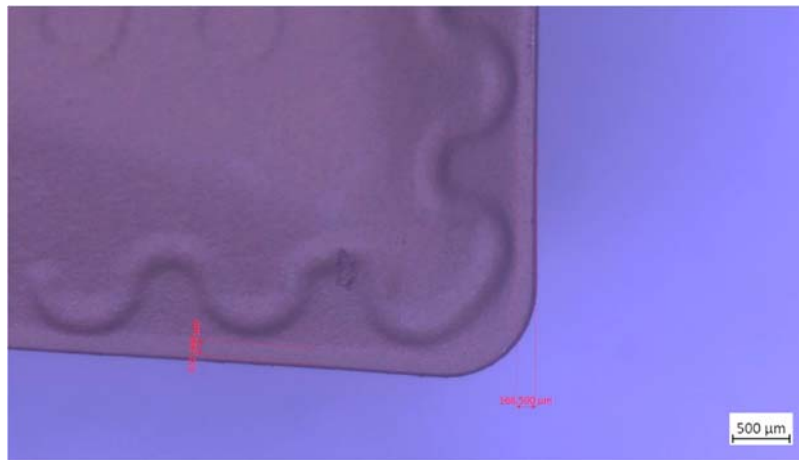
Figure 2. *Measuring the width of the land using a microscope.*

We could not determine the position of the surfaces marked C and D in Figure 1 either on the basis of the microscopic image or with a hand-held protractor, so we had to look for some other method.

4. 1. Results of scanners

We used a 3D scanner to determine the C and D surfaces of the cutting insert. First, we worked with a Roland Pix4 touch scanner. The advantage of this is that it can also digitize shiny metal surfaces. The scanning resolution was 0.05 mm in all three coordinate directions. The obtained result can be seen in Figure 3 in the Dr. Picza3 program included with the scanner. With the help of the program, the coordinates of

the scanned points can be queried, and the distance between two points can also be determined. The width of land can also be checked in the program, for this value the software gives is 0.15 mm (short red line in the figure (Figure 3))
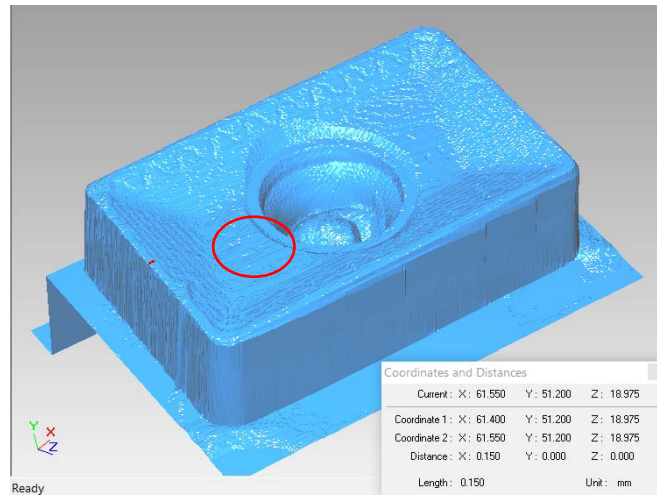
Figure 3. *The scanned image of the insert in the Picza3 program*
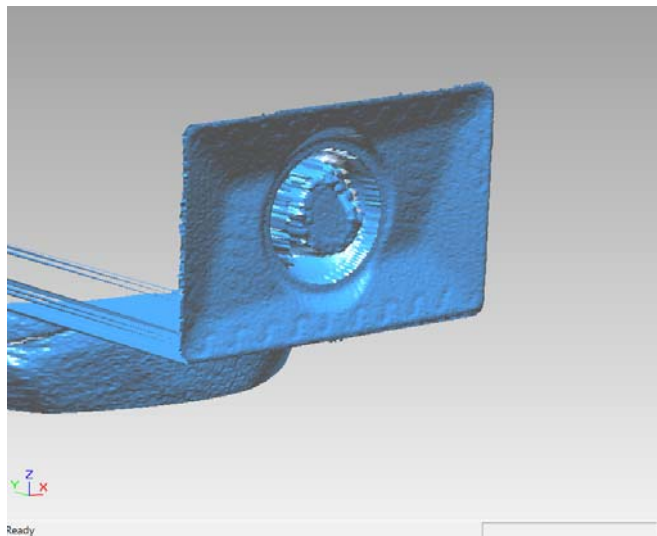
Figure 4. *Surface digitized by the laser scanner*

Based on the figure, we can see that the model made with the scanner has too bad surface and cannot be used in finite element simulations. That is why we continued the work, we painted the insert with a matte white colour (Mr. Hobby, MrFinishing Surfacer 1500 White paint at a thickness of about 30 µm with an airbrush gun) in order to try to digitize the insert in a laser scanner. The type of the used laser scanner is Roland LPX-1200. The used resolution was 0.1 mm in all coordinate directions (this is the finest resolution that the scanner can handle). For the operation, we chose the planar scanning mode. The result is shown in Figure 4.

The digitized surface of the insert is much more accurate than the one obtained with the touch scanner, but it is still not good for finite element software. The obtained result was cleaned of unnecessary parts (they were used to install the insert in the scanner) and imported into the Solid Edge 2020 program, where we were able to determine the data required for editing the CAD model.

4. 2. Building up the CAD model

The surface loaded into the Solid Edge program (cleaned of false parts) can be seen in the following figure (Figure 5). The first step in determining the geometric data of the insert is to know the inclination angle of the planes marked C and D in Figure 1 (the rake angle of the insert). Inclination angles must be measured in a plane perpendicular to the cutting edge. To do this, we first draw two straight lines on both cutting edges (drawn in black, marked by thick red arrows).
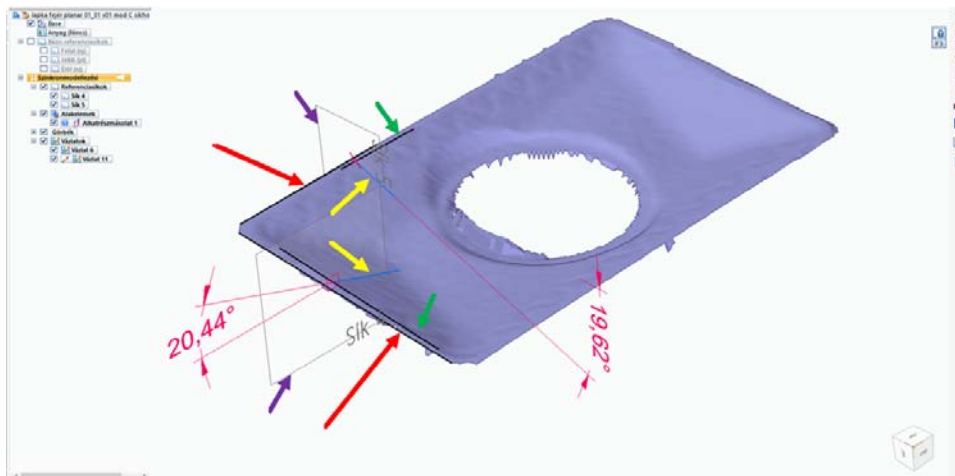
Figure 5. *Determination of the inclination angle of the planes marked C and D*

The lines were created by selecting two nodes of the scanned mesh to closely approximate the real edge of the insert. We made the planes labelled with plane 4 and plane 5 perpendicular to the two lines created in this way (indicated by purple arrows). The measurements will be carried out in these planes. We also need additional lines to determine the angle values we are looking for. Two of these are that edges of the land which facing to planes C and D (indicated by green arrows). It was created in a similar way as the straight lines of the cutting edges. These lines are needed because planes C and D start from here. Two more lines still needed for angle measurement are marked with yellow arrows. These lines run in the planes C and D (approximately, within the accuracy of the scanner). They start from the punching points of the straight lines marked with green arrows and the recorded perpendicular planes (plane 4 and plane 5) and end at a point provided by the scanner. With this, we were able to set up the auxiliary lines that give the measurement. In the following figure (Figure 6) it is visible between which lines, and in which plane the measurement takes place. The straight lines are marked with yellow arrows. In the case of plane C, we obtained 20.44°. The method described above was also applied to the plane marked with D. The value of the inclination angle obtained here is 19.62° (Figure 7).
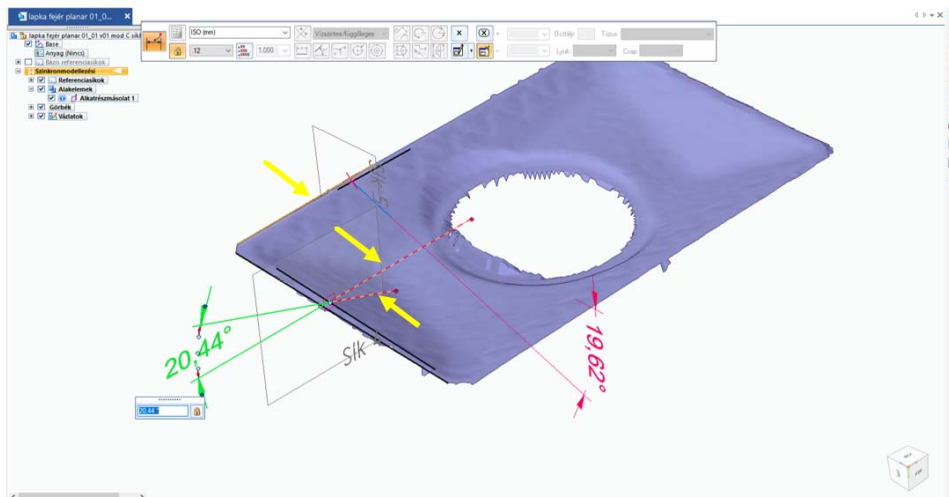
Figure 6. *The angle of inclination of the plane marked C with respect to the upper plane of the insert*
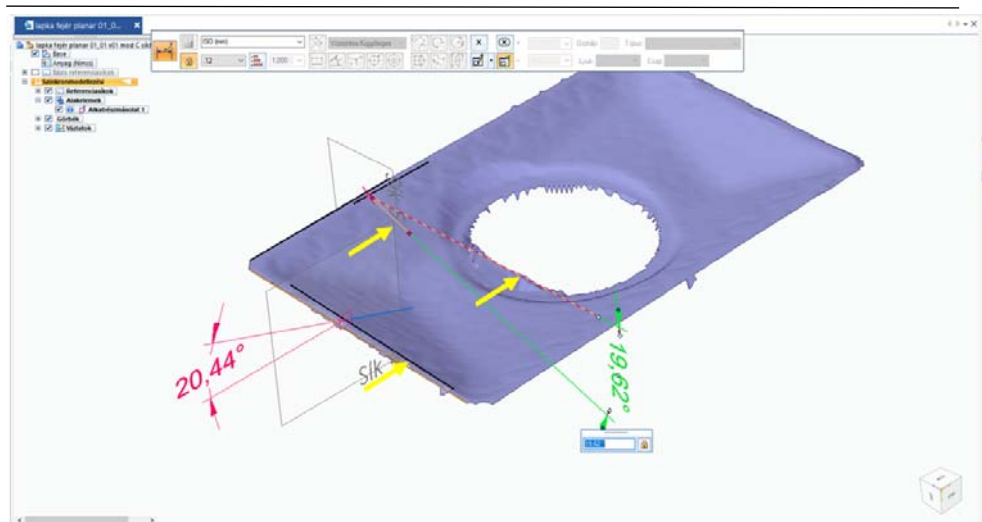
Figure 7. *Determination of the angle of inclination of the plane marked D*

When creating the CAD model, we rounded off the measured values and took the rake angle of the insert as 20° - in both directions. The error experienced in the measurement of the angles was primarily caused by the resolution of the scanner, the smallest value of the resolution is 0.1 mm (this was used). We still need additional data to create the CAD model. You should know the rounding of the outer edge of the land, the rounding between planes C and D, the data of the upper surfaces marked E, F and G. The missing data were determined using the methods described in the lines above, as well as with the help of a microscope and a three-dimensional roughness measuring machine, which are as follows:

- Edge rounding 0.05 mm, with a three-dimensional surface roughness measuring machine (method: [8]).
- The inclination angle of plane E is 18° (from the scanning result).
- The inclination angle of plane F is 11° (from the scanning result).
- The radius of the rounding marked G is 0.4 mm based on the microscope image.
- The rounding between planes C and D is given on the CAD model in such a way that it follows the R=0.8 mm rounding of the tool tip in parallel.

After the measurements, microscopic examinations and scans, all data was available to create the CAD model. The finished model can be seen in the following figure (Figure 8):
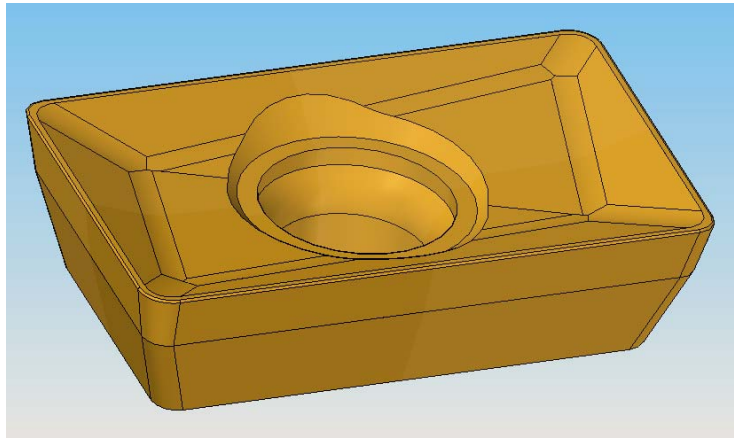
Figure 8. *The completed CAD model in the Solid Edge 2020 program*

5. INTEGRATING THE COMPLETED CAD MODEL INTO THE FEM PROGRAM

AdvantEdge software cannot directly read a model saved in Solid Edge's own file format. But it is possible to read some standard 3D CAD model file formats: stl, vrml and step. AdvantEdge best supports the step format, so the created model in Solid Edge must be saved in step format as well. We can import the tool model using the STEP Tool Import command of the AdvantEdge program. Inserts must be placed in the workspace as they appear in the milling head. The radial and axial rake angles, the lead angle, the cutter diameter, and the number of inserts (cutting edges) must be entered.
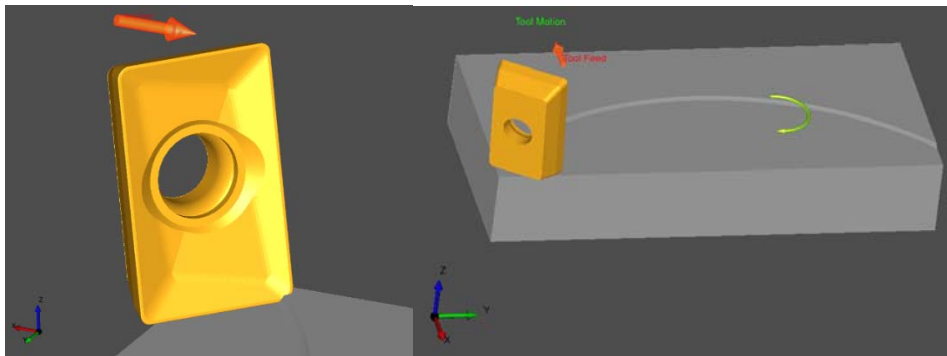
Figure 9. *CAD model of the insert in the AdvantEdge program*

The tool will then appear in the software workspace, and if necessary, it is possible to change the orientation of the tool. In the last step, we specify the necessary parameters for finite element meshing of the tool. With this, the imported insert model is ready to start the FEM face milling simulation (Figure 9.).

6. SUMMARY

With the help of the process presented in the points above, a CAD model of any existing cutting insert can be produced. The use of 3D scanners is essential in today's engineering research work. Unfortunately, its limitations are also clearly visible in the study presented. Scanners cannot create a precise edge geometry, which would be suitable in finite element programs used to model the cutting process, not least because of their resolution (inaccuracy). Therefore, there is no other option than building the inserts in CAD software. The CAD model also provides the opportunity to determine the tool's characteristic angles in the various system of tool designations, relatively easily and quickly by generating the appropriate sections.

REFERENCES

Alzghoul, M., Sarka, F., & Szabó, F. (2022). A Spindle System Analysis Using Systems Receptance Coupling Approach. *Design of Machines and Structures, 12*(2), 24-30. https://doi.org/10.32972/dms.2022.010

Borysenko, D., Karpuschewski, B., Welzel, F., Kundrák, J., & Felhő, C. (2019). Influence of cutting ratio and tool macro geometry on process characteristics and workpiece conditions in face milling. *CIRP Journal of Manufacturing Science and Technology, 24*, 1-5. https://doi.org/10.1016/j.cirpj.2018.12.003

Felhő, C. (2020). Finite element modelling of cutting force components in face milling. *Multidiszciplináris Tudományok, 10*(1), 119-128. https://doi.org/10.35925/j.multi.2020.1.15

Jálics, K. (2017). Simulation Methods in the Vehicle Noise, Vibration and Harshness (NVH). In K. Jármai, & B. Bolló (Ed.), *Vehicle and Automotive Engineering. Lecture Notes in Mechanical Engineering* (pp. 91-97). Miskolc: Springer. https://doi.org/10.1007/978-3-319-51189-4_9

Karpuschewski, B., Kundrák, J., Felhő, C., Varga, G., Sztankovics, I., Makkai, T., & Borysenko, D. (2018). Preliminary Investigations for the Effect of Cutting Tool Edge Geometry in High-Feed Face Milling. In K. Jármai, & B. Bolló (Ed.), *Vehicle*

and Automotive Engineering 2. VAE 2018. Lecture Notes in Mechanical Engineering (pp. 241-254). Miskolc: Springer. https://doi.org/10.1007/978-3-319-75677-6_20

Kundrák, J., Sztankovics, I., & Gévai, M. (2019). Comparative analysis of CBN cutting inserts with different edge geometries. *Cutting & Tools in Technological System*(91), 97-106. https://doi.org/10.20998/2078-7405.2019.91.10

Ortner, H., Ettmayer, P., & Kolaska, H. (2014). The history of the technological progress of hardmetals. *International Journal of Refractory Metals and Hard Materials, 44*, 148-159. https://doi.org/10.1016/j.ijrmhm.2013.07.014

Pálmai, Z., Dévényi, M., & Szőnyi, G. (1991). *Szerszámanyagok.* Budapest: MVAE és Műszaki Kiadó.

Sandvik. (2023., 10. 30.). Retrieved from Sandvik Web site: https://www.sandvik.coromant.com

Sarka, F. (2022). Examination of Bolt Connection with Finite Element Method. In K. Jármai, & Á. Cservenák (Ed.), *Vehicle and Automotive Engineering 4. VAE 2022. Lecture Notes in Mechanical Engineering* (pp. 212-222). Miskolc: Springer. https://doi.org/10.1007/978-3-031-15211-5_19

Schröter, K. (1923). *Patent No. DE420689C.*

Sztankovics, I. (2019). FEM analysis on the impact conditions of the insert in face milling. *MultiScience - XXXIII. microCAD International Multidisciplinary Scientific Conference.* Miskolc: Miskolc University Press. https://doi.org/10.26649/musci.2019.053

INVESTIGATION AND COMPARISON OF ITERATION CURVES OF OPTIMIZATION ALGORITHMS

FERENC JÁNOS SZABÓ

University of Miskolc, Institute of Machine and Product Design
H-3515, Miskolc-Egyetemváros
ferenc.szabo@uni-miskolc.hu
https://orcid.org/0000-0002-6694-8959

Abstract: The iteration history curve of optimization algorithms is a saturation- type development curve or sigmoid shape curve. After an overview of several different sigmoid curves, the iteration history curve of the RVA (Random Virus Algorithm) is analysed in order to find its best settings for a given optimization problem. The analysis of the characteristics and numerical parameters of the iteration history curve provides the possibility to discover the speed and efficiency of the algorithm without the necessity to wait throughout the whole running until its final result, which can speed up numerical experiments during the search for the solution to the optimization problem and while 'fine tuning' the algorithm to the given task. Since sigmoid-type curves can be found in many different fields of life (the history of the sport world records, comparison of the achievements of several groups), the results of this analysis can be used in several different domains of life, when the ranking, comparison, evaluation or qualification of several individuals or groups is important.

Keywords: *Iteration history curves, sigmoid curves, saturation curves, comparison of algorithms, group achievements.*

1. INTRODUCTION

Each optimization algorithm has some very important numerical parameters which can have important effects on the behaviour and characteristics of the algorithm. These important characteristics could be the 'speed' (how many objective function evaluations are necessary until finding the final optimum solution), or the 'efficiency' (how many times the constraints are checked until finding the optimum solution). These characteristics are strongly connected with the quantity of the necessary calculations to be performed until the optimum result.

These days Multidisciplinary Optimization (MDO) is a very common approach (Abraham, Hassanien, Siarry, & Engelbrecht, 2009), (Cramer , Dennis, Jr., Frank, Lewis, & Shubin, 1994), (Martins & Lambe, 2013), (Szabó, 2008), (Vanderplaats, 2007) and more and more structures are being analysed by MDO methods. During an MDO task, the evaluation of the objective function and/or the checking the constraints may require long finite element computations, therefore the computer running of these investigations could take even several days. Nowadays evolutionary optimization offers efficient algorithms for the solution of these tasks (Das, Dasgupta, Biswas, Abraham, & Konar, 2009), (Deb, 2007), (Eberhart & Kennedy, 1995), (Fogel, 1999.), (Gao, Hongwei, Zhao, & Cui, 2006), (Goldberg, 1989), (Martens, et al., 2007), (Sheel, 1985). Engineering Design Optimization is also an increasingly popular field in optimization science (Herskovits, Mappa, Goulart, & Mota Soares, 2005), (Pang, Chen, Wang, & Hou, 2012), (Zhang, Zhou, Zhou, Wang, & Zhang, 2005), (Szabó, 2016).

Because the parameters of the algorithm can have important effects on the most important characteristics of the algorithm, by modifying these parameters it may be possible to spare a significant amount of calculations, so we could decrease the number of days necessary for finding the final solution. The procedure for changing the settings of these parameters and finding the effects of these settings on the value of the optimum solution and on the time and calculation amount necessary to reach to goal, can be called 'numerical experiments' on the algorithm settings. If the total running time of the algorithm can be several days, this means we have to wait for several days in order to see the effects of the current settings of the algorithm parameters. After that there will be the time necessary to evaluate and understand these effects, and to determine some new values to improve the settings. Once more several days will be necessary to see the new results and find the effects of these new settings. This procedure makes the total time of the numerical experiments process very long.

In this paper the RVA optimization algorithm (Szabó, 2008) is used to demonstrate the usage and efficiency of the iteration curve analysis, showing the numerical experiment (parameter setting combinations) process for a simple optimization task. The analysis of the equations of the sigmoid curves can be used not only for investigating one algorithm, but for the comparison of several algorithms (for the same test problem for example), thus it could be possible to find the best algorithm for the given optimization problem.

Sigmoid curves describing growth or saturation phenomena are used in many fields of life for description, study and forecast of these kinds of situations. These curves are highly multidisciplinary curves, because one can find many different applications of these curves in a large variety of problems (biology – population dynamics,

economy – lifecycle curve of products, medicine – growth of tumours or time history of pandemic disease just like COVID 19, environmental protection – plastic waste in oceans, agriculture – growth of fishes and forests, optimization – iteration history curve of optimization algorithms).

Discovery and investigation of the sigmoid curves started in the years of 1700. Malthus (Malthus, 1798), who proved that the increase in the number of members of a species is dependent from the actual value of this number. This is the basis of the Moore (Moore, 1965) law for computers capacity increase. Verhulst (Verhulst, 1847) derived the sigmoid curve describing the case of saturation, introducing the denomination of this type of curve 'logistic curve' or logistic function. Pearl and Reed (Pearl & Reed, 1920) applied the logistic curve for the study of the population growth of USA. The S-like shape of the curve made possible to use the attribute "sigmoid" for these curves. Fisher and Pry (Fisher & Pry, 1971) developed a transformation of the curves from S-shape into linear function, which makes easier to calculate the regression coefficient in case of approximation of the curves. Bertalanffy (Von Bertalanffy, 1960) used sigmoid curves for the description of the growth of the length of sharks, these results are useful also for the study of several fish species and in forestry too. Kozuko and Bajzer (Kozuko & Bajzer, 2003) applied this growth function for the study of the growth of tumours in medicine. The growth function modified by Richards (Richards, 1959) is applicable for the studies of the growth of several plants, too.

Mansfield (Mansfield, 1961) and Rogers (Rogers, 1962) described the products lifecycle as sigmoid curve. Jang Show- Ling, Dai, and Sung (Jang, Dai, & Sung, 2005) shown that the spread of the mobile phones in 29 OECD countries and Taiwan can be described also by sigmoid curves. Investigating some pulsating or multi-wave phenomena by Meyer (Meyer & Turner II, 1994) shown the possibility of the application of bi-logistic, tri-logistic or multi-logistic curves, which were used by Silverberg and Lehnert (Silverberg & Lehnert, 2003) for the investigation of the evolutionary models of economic growth. Fokasz (Fokasz, 2006) gave interesting examples of the application of sigmoid curves for social phenomena.

Szabó investigated several phenomena by sigmoid curves: one hundred years history of sports world records (Szabó, 2011), proposed a comparison and qualification system using sigmoid curves (Szabó, 2017) having the name EBSYQ (Evolutionary Based System for Qualification and comparison of group achievements), investigated the iteration history curves of optimization algorithms (Szabó, 2018), studied the possible future of the plastic waste in oceans of the Earth (Szabó, 2019), investigated wear curves of tools (Szabó, 2021), shown that product lifecycle can be described also by sigmoid curves (Vajna, 2020), (Bihari & Sarka, 2018), investigated the time curve of COVID 19 disease in Hungary (Szabó, 2020). For all these

investigations Szabó applied the approximation procedure based on the Nelder-Mead optimization algorithm (Nelder & Mead, 1965), defined the approximation process as an optimization procedure searching for the minimum of the square differences. Rézsó (Rézsó, 2020) shown an example for the application of the EBSYQ system for the comparison of several student groups writing the same exam test.

Because sigmoid type curves can be found in many different fields of the life (history of the sport world records, comparison of the achievements of several groups), the results of this kind of analysis can be used in several different domains of life; anywhere where the ranking, comparison, evaluation or qualification of several individuals or groups is important. This could help the work of teachers of student groups, jury members of grants and competitions, or selection teams and committees for job applications, adjudications of grants or awards, etc.

2. OVERVIEW OF SOME SIGMOID CURVES

The iteration history curve of the RVA optimization algorithm for a simple demonstration optimization problem can be found in Figure 1. It can be seen from the figure, that in the beginning phase of the optimization, the improvement in the objective function is high over several generations, but this 'improvement speed' decreases in the final phase of the optimum search. This effect can be called 'saturation', and this gives the sigmoid shape of the curve.
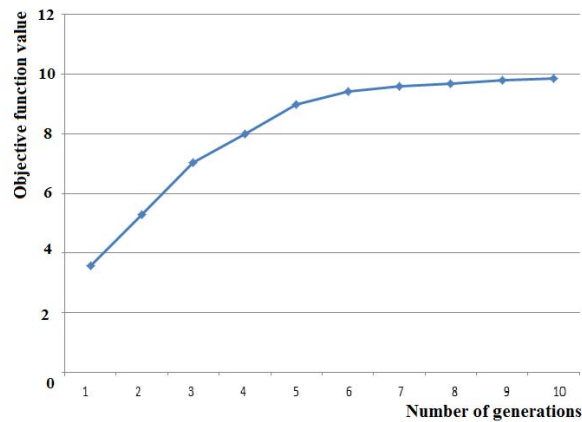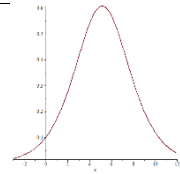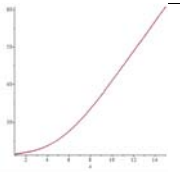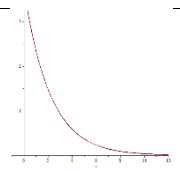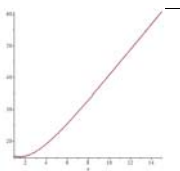
Figure 1. *Iteration history curve of RVA algorithm*

On the basis of the mathematical representation of the iteration history sigmoid curve of the algorithm, it will be possible to see the most important parameters determining the shape of the curve and also the most important characteristics of the result (maximum possible value achievable, steepness of the curve which is in connection with the improvement speed of objective function, etc.). If the curve is approximated by using only the first 3-4 iterations, it is not necessary to wait for the total running time of the algorithm; the current setting can be evaluated and qualified much earlier. This gives the possibility for developers to save more than the half of the total development time, which is an important achievement.

Table 1 shows the curve shape, the first derivative and the integral function shape of several different sigmoid type functions, in order to see and compare the most important characteristics of the sigmoid shape curves. One can draw some conclusions from the Table 1. Two different types of curves are possible: in the beginning phase with a curvature (e.g., Pearl-Reed function), or without beginning curvature (e.g., Bertalanffy function). Maybe it is not the curve itself that has the sigmoid shape but its integral (e.g., Life-curve). The derivative of the curves also can have different shapes (e.g., a Törnquist curve, Mitscherlich curve, Life-curve, or Pearl-Reed curve). For further investigations three curves will be selected: the Pearl-Reed curve because of its beginning curvature, one curve without beginning curvature (Bertalanffy), and later the Life-curve because of its very special shape.

Table 1
Sigmoid curves used for approximation

curve	derivative	integral
Pearl–Reed		
Bertalanffy		

Equations of the curves and their derivatives or integrals are as follows:

a.) Pearl-Reed (logistic) curve (Pearl & Reed, 1920):
equation of the curve:

$$y(x) = \frac{K}{1+ce^{-rx}}, \text{ first derivative: } \frac{dy(x)}{dx} = \frac{Kcre^{-rx}}{(1+ce^{-rx})^2} \tag{1}$$

$$\text{integral: } \int y(x)dx = -\frac{K}{r}\ln(e^{-rx}) + \frac{K}{r}\ln(1+ce^{-rx}) \tag{2}$$

b.) Bertalanffy growth-curve (Von Bertalanffy, 1960):
equation of the curve:

$$y(x) = K(1 - ce^{-rx}), \text{ first derivative: } \frac{dy(x)}{dx} = Krce^{-rx} \tag{3}$$

$$\text{integral: } \int y(x)dx = Kx + \frac{Kc}{r}e^{-rx} \tag{4}$$

Since the real iteration history curve of the studied algorithm can be either a growth-curve type, or a logistic curve, it is enough to select two curves (the Bertalanffy curve and the Pearl-Reed curve) from the six sigmoid curves of Table 1. Analysis of the Life-curve (equation of the curve, derivative, integral of it) may give further special results (eigenvalue of the algorithm, Lorentz-profile (Lorentz, 1905), spreading characteristics).

3. APPROXIMATION OF THE CURVES

The iteration history curve will be approximated by the Pearl-Reed and Bertalanffy curve, by using the method of least squares, determining the parameter values of K, r, c in the equation of the curves which give the best approximation to the iteration history curve.

During the method of least squares it is necessary to approach the given discrete values: $(x_i, y_i), i = 1, 2, 3, \ldots, n,$ by a function $y^* = f(x)$, while the parameters of the curve should give the minimum possible value of the sum of the squares of the differences. This means that regarding the function values $f(x_i) = y^*_i$, we have to find:

$$H = \sum_{i=1}^{n}(y_i - y_i^*)^2 = min \tag{5}$$

The minimum is possible if the first derivative of the function H is 0, therefore: $\frac{\partial H}{\partial K} = 0, \frac{\partial H}{\partial r} = 0, \frac{\partial H}{\partial c} = 0$, this gives three equations for the three unknowns K, r and c, so it is possible to find the parameters for the best approximation. Another possible way to find the minimum of H as a function of the three parameters, is to solve the problem as an unconstrained minimization task of H using the three parameters as design variables. In this paper this method of optimization is selected for the

calculation of the best curve-parameters during the approximations. For the numerical solution of this optimization task the Nelder-Mead 'simplex' algorithm (Nelder & Mead, 1965) is used.

The linear regression coefficient will be used to check the quality of the approximation. Thus it is necessary to calculate the regression coefficient for both of the curves. Since the two selected curves are non-linear, before the analysis of the regression it is necessary to transform the equations of the curves into linear form. The regression coefficient calculated for these resulting linear functions will show which curve has the better correlation with the discrete data, so the conclusions derived from that curve will be stronger, or more realistic.

The value of the regression coefficient is always between -1 and +1. If it has a value of 0, that means there is no relationship between the curve and the discrete values. The closer the regression coefficient's absolute value to 1, the better the correlation is between the data and the approximation curve. If the regression coefficient is negative, it shows a decreasing tendency, while positive value shows an increase. This means that the conclusions derived from a curve having a 'weak' regression coefficient will be not 'true', not 'strong' or not accurate enough, but the conclusions derived on the basis of a curve having good correlation will be true and adequate, or 'strong'.

For calculation of the regression coefficient, the curve equations need to be transformed into linear form for both of the selected functions. The linear transformation of the Bertalanffy- function:

$$y(x) = K(1 - ce^{-rx}), \, ce^{-rx} = \frac{K-y(x)}{K}, \, \ln c + \ln e^{-rx} = \ln\left(\frac{K-y(x)}{K}\right), \qquad (6)$$

therefore, linear function for the Bertalanffy -curve is: $y^* = a + bx$, where $a = \ln c$, $b = -r$.

The linear transformation of the Pearl-Reed function can be done in a similar way:

$$y(x) = \frac{K}{1+ce^{-rx}}, \, \frac{K-y(x)}{y(x)} = ce^{-rx}, \, \ln c + \ln e^{-rx} = \ln \frac{K-y(x)}{y(x)}, \, y^* = a + bx \qquad (7)$$

The regression coefficient can be calculated as:

$$R_{lin} = \frac{A_{xy} - \frac{B_{xy}}{n}}{\sqrt{\left(C_x - \frac{D_x}{n}\right)\left(C_y - \frac{D_y}{n}\right)}} \qquad (8)$$

where: $A_{xy} = \sum_{i=1}^{n} x_i y_i$, $B_{xy} = \sum_{i=1}^{n} x_i \sum_{i=1}^{n} y_i$, $C_x = \sum_{i=1}^{n} x_i^2$, $D_x = (\sum_{i=1}^{n} x_i)^2$ and $C_y = \sum_{i=1}^{n} y_i^2$, $D_y = (\sum_{i=1}^{n} y_i)^2$.

In equation (8) it is possible to calculate the linear regression coefficient of the y^* transformed function determined in equation (6) or (7), but for simplicity we return to the y notation.

4. DEMONSTRATION EXAMPLE

In order to show the steps of the numerical experiments, let us consider the following simple optimization problem: Find the maximum of the two variables Rosenbrock-function (9) (Rosenbrock, 1960):

$$f(x, y) = 10 - (1 - x)^2 - 100(y - x^2)^2 \tag{9}$$

when the explicit constraints are:

$-2.5 \leq x \leq 2.5$ and $-2.5 \leq y \leq 2.5$, implicit constraint: $x^2 + y^2 \leq 2$.

The shape and contours of the objectives function are shown in Figure 2.
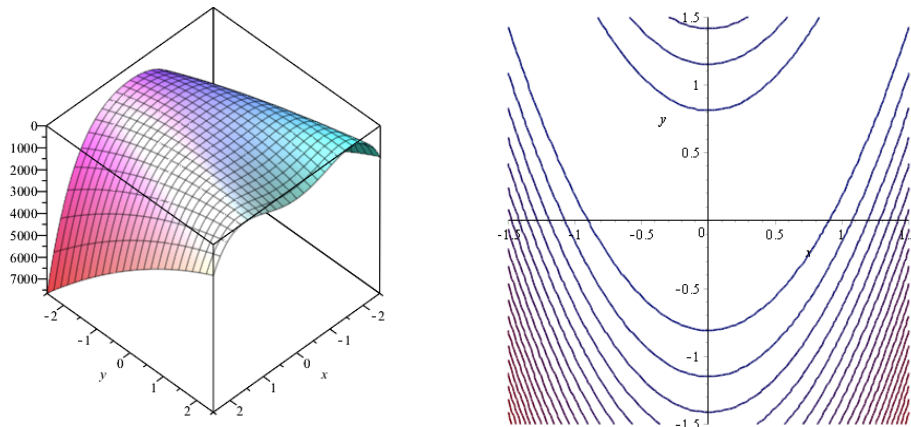
Shape of the function   Contours of the function

Figure 2. The objective function of the optimization example

The solution of the problem is that the maximum of the $f(x, y)$ is 10 at $x = 1$ and $y = 1$.

For the solution the RVA (Random Virus Algorithm) optimization algorithm is used and the iteration history curve of the algorithm is shown in Figure 1. This curve is a sigmoid function having saturation behaviour; therefore the Pearl-Reed function and

the Bertalanffy-function is used for its approximation. The approximation of the iteration history curve can be seen in Figure 3 which shows that all the three curves (the original curve, the Pearl-Reed curve and the Bertalanffy curve) are very close each to another, so any of the selected two curves can be used for the approximation.
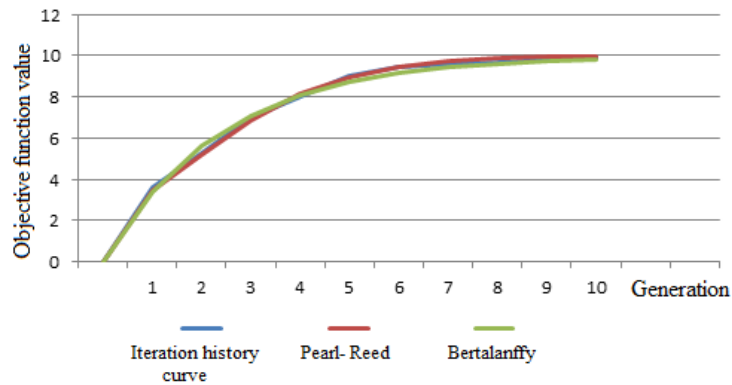
Figure 3. Approximation of the original iteration history curve

For further investigations the Bertalanffy curve seems to be better to use, because in the original iteration history curve the initial curvature of the Pearl-Reed curve is missing, therefore the shape of the curve is closer to the Bertalanffy curve. Also the regression coefficient absolute value is higher for the Bertalanffy curve than for the Pearl-Reed curve. However, because of the very special shape of its derivative, the Pearl-Reed function could give some interesting additional information during comparisons of several algorithms.

Equations of the approximating curves:

Pearl-Reed curve: $y = \frac{K}{1+ce^{-rx}}$, $K = 10$, $r = 0.7, c = 3.8$, regression coefficient value: -0.99183.

Bertalanffy curve: $y = K(1 - ce^{-rx})$, $K = 10$, $r = 0.41, c = 1$, regression coefficient: -0.99607.

The curves of the approximating functions can be seen in Figure 4 and their derivatives in Figure 5.
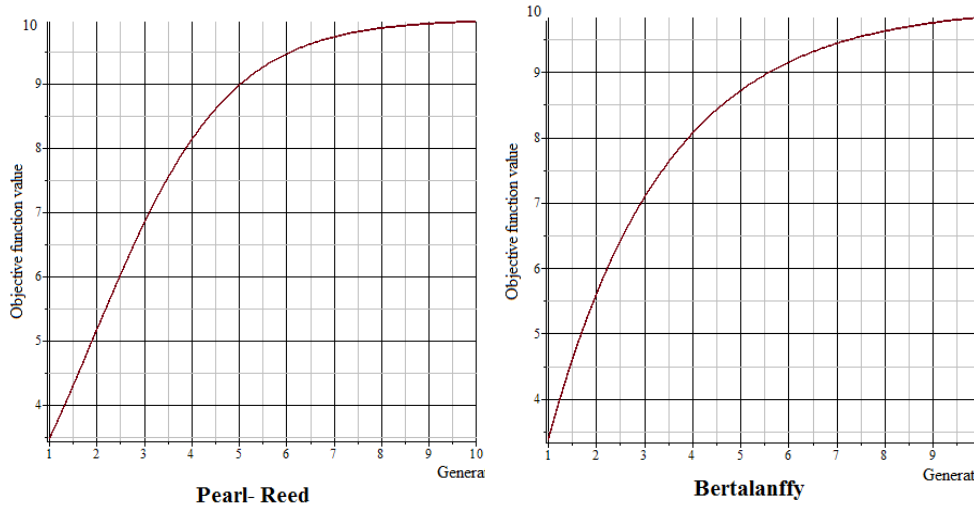
Figure 4. *The approximating functions*
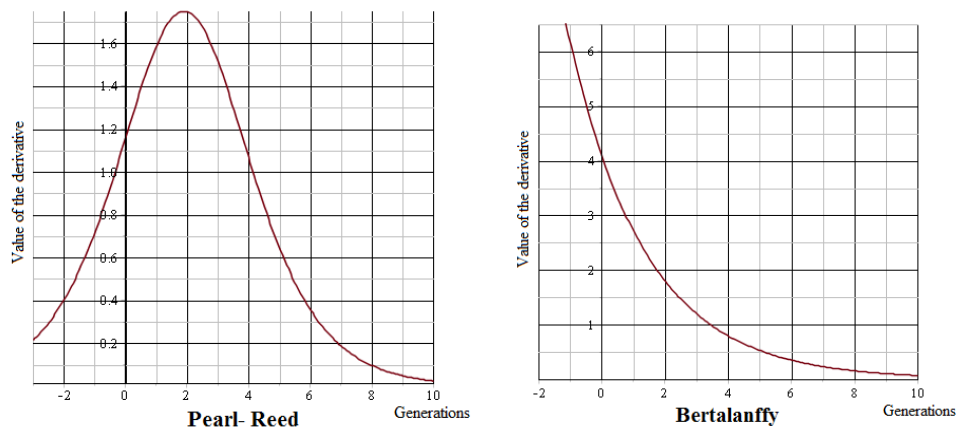
Figure 5. *First derivative of the approximating functions*

The derivative functions show the speed of the increasing of the objective function. It can be seen in Figure 5 that this speed decreases at higher number of iterations. The derivative of the Pearl-Reed function can say more: it shows, where the maximum of this speed is. This could be useful information if we want to compare several

algorithms, because a better algorithm should have this maximum earlier, since this will give a more efficient search in the starting phase of the optimization. The width of the Pearl-Reed derivative curve in the half of its maximum shows how durable this maximum speed is, so it could be also very useful for the comparisons of several optimization algorithms.

The integral function of the approximating curves is presented in Figure 6.
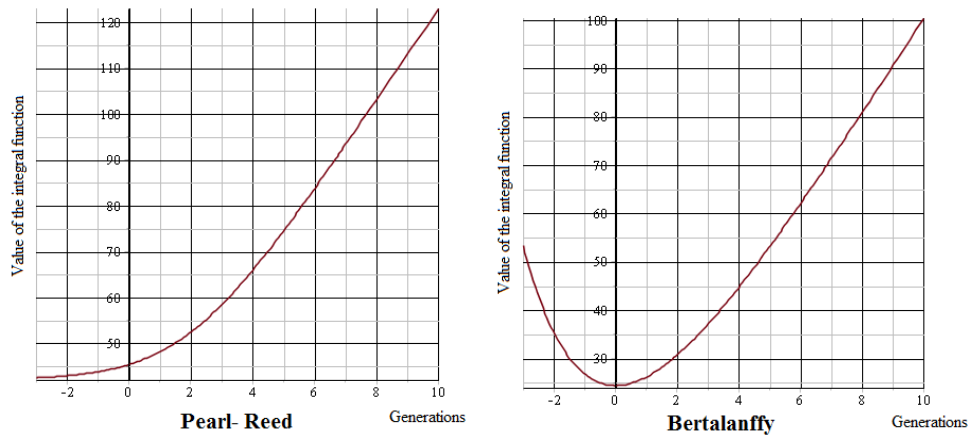
Figure 6. Integral of approximation curves

Comparison of the integral function of the approximating Pearl-Reed and Bertalanffy curves of the iteration history curve shows that the beginning phase of the search is more efficient for the Pearl-Reed function than for the Bertalanffy curve (because the same number of iterations shows a higher value of the integral function). In case of a higher number of iterations (or in the final phase of the optimization) the integral functions are parallel, so in this phase there is no difference in the efficiency. These curves can be very useful during the comparison of several algorithms.

In Figure 5 the first derivative of the Pearl-Reed function shows that the most efficient part of the optimization is the first phase of the process, with four generations, since the speed increase of the best objective function value of the generations is highest here. This leads to the idea to use only the first four iterations for building up the approximation curves of the iteration history curve, in this way saving 60% of the total time. There is no need to wait until the end of the total running time of the algorithm, we can guess the expectable optimum result. On the basis of this result, it is possible to change the settings of the algorithm and continue the numerical

experiment. This method will decrease the total development time by more than 50%. Comparing the curves belonging to different settings of the algorithm parameters, it is possible to compare different states of the algorithm and will be easier to find the best setting values. Therefore, by using the proposed system of comparison the numerical experiment process can be made quicker and more accurate, based on the numerical comparison of different characteristics of the iteration history curves resulting from the settings.

Since the shape of the Life function and the derivative of the Pearl-Reed function (logistic function) is very similar, it seems to be useful to approximate the derivative of the logistic function with the equation of the Life-curve (Lorentz, 1905), (Andrews, 1998), because this way it will be possible to study the dispersion function (derivative of the Life-curve) and the error-function (integral of the Life-curve) of the algorithm, too (Figure 7.).

Here $K = 1.73, r = 1.85, c = 0.32$. The regression coefficient is 0.98381.

Life- curve
(Lorentz- function)   **Dispersion function**   **Integral of the Lorentz- function**
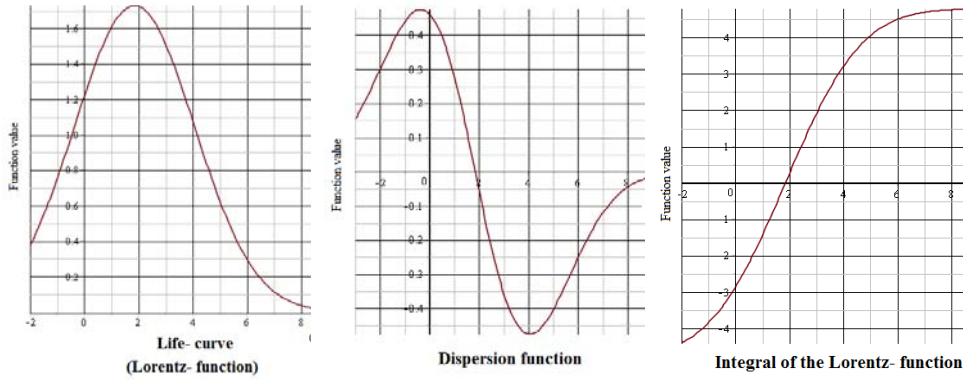
Figure 7. *Life-curve, dispersion function and error function of the algorithm*

Equation of the approximating Life-curve of the algorithm (the Lorentz-function):

$$f(x) = \frac{K}{e^{c^2(x-r)^2}} \tag{10}$$

The dispersion function is the derivative of the Life-curve:

$$f'(x) = -\frac{K(2c^2x - 2c^2r)}{e^{c^2(x-r)^2}} \tag{11}$$

The integral of the Life-curve is the error function of the algorithm:

$$\int f(x)\,dx = \frac{K\sqrt{\pi}}{2c}\operatorname{erf}\left(c(x-r)\right), \text{ where } \operatorname{erf}(x) = \frac{2}{\sqrt{\pi}}\int_0^x e^{-t^2}\,dt \qquad (12)$$

The error function of the algorithm is once more a sigmoid curve; therefore it could be also used for the comparison of different algorithms or to compare the different settings of the same algorithm. Smaller K in this function means smaller expectable value of the error function, so it seems to be better than higher K values. If r is smaller, the error function is not so steep, which could be better than higher r values (when the increase in the error function is slower).

Table 2

Comparison of two different settings of the RVA algorithm

Short description of the point of view	Score of setting I	Score of setting II	Point of view winner
Expectable optimum (K), Pearl - Reed, (PR)	10	10	both
Expectable optimum (K), Bertalanffy, (Bfy)	10	10	both
Obj. function value increasing speed (r), PR	0.7	0.67	setting I
Obj. function value increasing speed (r), Bfy	0.41	0.39	setting I
Regression coefficient, PR	-0.99183	-0.98743	setting I
Regression coefficient, Bfy	-0.99607	-0.98832	setting I
Place of the speed maximum, PR derivative	2	3	setting I
Durability of the speed maximum, PR derivative	5	5	both
Algorithm efficiency from integral of PR	130	125	setting I
Algorithm efficiency from integral of Bfy	90	85	setting I
Eigenvalue in Life-curve	2	3	setting I
Durability in Life-curve	5	5	both
Error function K	1.73	1.75	setting I
Error function r	1.85	2.3	setting I
Maximum amplitude of the dispersion function	0.94	0.9	setting II
Half width of the dispersion function	8	7.8	setting II
Maximum expectable value of the error function K	4.85	5.25	setting I
Increasing speed of the error function r	0.592	0.678	setting I
Number of points of view won	16	6	setting I

In Table 2 several points of view are collected comparing two different settings of the RVA algorithm for the demonstration example shown above. Comparing the two settings of the RVA optimization algorithm to the same problem, it can be concluded that the 'winning' setting will result the quicker and more efficient work of the algorithm. Applying the four-point approximation method for the sigmoid curve of the

algorithm makes possible to decrease the total time necessary for the whole development process approximately by 50% comparing to the case when always waiting through the total running time of the algorithm with a given setting.

Results and comparison points of view presented in this work are parts of the EB-SYQ (Evolution Based System for Qualification of Group Achievements) curve analysis system (Szabó, 2017), which is a comparison and evaluation system developed for the qualification and evaluation of groups. It is intended to help the decision-making work of teachers of student groups and jury of competitions, grants, or awards, but it is based also on sigmoid curves and one can find or 'translate' more useful comparison points of view from that system into the algorithm comparison process, too.

Main steps of the usage of the EBSYQ system: set up the points of view (which represent the most important characteristics to be compared), see the curves and equations for comparing these points of view, and compare how many points of view has won each item (group, algorithm, or setting) to be compared.

Table 3

Comparing setting parameters of the curve obtained by four points and of the curve obtained by waiting through the total running time (original curve)

	K	r	c
Original curve	10	0.41	1.0
Four points curve	9.88	0.39	0.97

According to the results shown in Table 2, Setting I is the winner, winning 73% of the total possible points. Taking only the four first generations of the iteration history, the Bertalanffy curve of the algorithm was approximated with the parameters shown in Table 3. It can be seen that the values are in good agreement, which means that by using this evaluation system, it is possible to cut down the total development time by more than half, during the numerical experiments process.

5. SUMMARY

The iteration history curve of optimization algorithms is a sigmoid shape saturation curve. The parameters in the equations of these curves are strongly connected to the most important characteristics of the algorithm (best objective function value increasing speed in function of the number of generations, expectable final optimum result, etc.). These characteristics can be efficiently modified by the setting parameters of the optimization algorithm. A complete numerical experiment process is needed for finding the best setting constellation for a given optimization problem. In

order to see the effects of the settings, normally it is necessary to wait until the algorithm has finished running, which can be very long in case of some complicated Multidisciplinary Optimization problems. This paper shows a proposed approximation and analysis system of the algorithm's iteration curve (EBSYQ) which makes possible to set up the iteration curve's equation from just the objective function best values of the first four generations. This gives the possibility to reduce the total time needed for the numerical experiment process by more than 50%.

During these investigations it is very interesting to discover the Lorentz-curve, the eigenvalue and dispersion function of the algorithm, which can give important additional information about the characteristics and behaviour of the investigated algorithm. The integral of the Lorentz-function is the error function (erf) of the algorithm, while the parameters of this curve also give very useful points of view for describing and characterizing the algorithm's speed and efficiency. On the basis of these results, it is possible to investigate one algorithm with several different setting constellations or to compare several different algorithms for the same optimization task in order to find the most efficient or quick one.

In this paper the example of the RVA algorithm is shown applied for the optimization of the Rosenbrock-function over a cylindrical feasible region in order to demonstrate the steps, the usage and efficiency of the EBSYQ curve analysis system. Two different setting constellations are compared and using 18 points of view the better setting can be selected for the optimization task. Continuing the setting change and comparing process, it is possible to find the settings that give the quickest or most efficient working of the algorithm.

The results and points of view of the EBSYQ system can be used for the analysis of several other problems in real life, such as selection and comparison of different groups applying for grants, for scholarships or for jobs (jury activity) or for sport results analysis during a time period, while teachers of several student groups can discover more accurately different sub-groups of their students and they can find more easily some target-groups for differentiated training or extra activities.

REFERENCES

Abraham, A., Hassanien, A.-E., Siarry, P., & Engelbrecht, A. (2009). *Foundations of Computa-tional Intelligence* (Vol. 3.). Springer.

Andrews, L. (1998). *Special Functions of Mathematics for Engineers.* Bellingham, USA: SPIE Optical Engineering Press.

Bihari, J., & Sarka, F. (2018). Human-electric hybrid drives in medium-sized cities by daily traffic. In K. Jármai, & B. Bolló (Ed.), *Vehicle and Automotive Engineering 2. VAE 2018. Lecture Notes in Mechanical Engineering.* Springer. https://doi.org/10.1007/978-3-319-75677-6_5

Cramer , E., Dennis, Jr., J., Frank, P., Lewis, R., & Shubin, G. (1994). Problem Formulation for Multidisciplinary Optimization. *SIAM Journal on Optimization, 4*(4), 754-776. https://doi.org/10.1137/0804044

Das, S., Dasgupta, S., Biswas, A., Abraham, A., & Konar, A. (2009). On Stability of the Chemotactic Dynamics in Bacterial-Foraging Optimization Algorithm. *IEEE Transactions on Systems, Man, and Cybernetics, Part A: Systems and Humans, 39*(3), 670-679. https://doi.org/10.1109/TSMCA.2008.2011474

Deb, K. (2007). Current trends in evolutionary multi-objective optimization. *International Journal for Simulation and Multidisciplinary Design Optimization, 1*(1), 1-8. https://doi.org/10.1051/ijsmdo:2007001

Eberhart, R., & Kennedy, J. (1995). A new optimizer using particle swarm theory. *Proceedings of the Sixth International Symposium on Micro Machine and Human Science*, pp. 39-43. Nagoya, Japan: IEEE. https://doi.org/10.1109/MHS.1995.494215

Fisher, J., & Pry, R. (1971). A Simple Substitution Model of Technological Change. *Technological Forecasting and Social Change, 3*, 75-88. https://doi.org/10.1016/S0040-1625(71)80005-7

Fogel, L. (1999.). *Intelligence through Simulated Evolution: Forty Years of Evolutionary Programming* (1. ed.). Chichester,: John Wiley,.

Fokasz, N. (2006). Növekedési függvények, társadalmi diffúzió, társadalmi változás. *Szociológiai szemle, 16*(3).

Gao, F., Hongwei, L., Zhao, Q., & Cui, G. (2006). Virus-Evolutionary Particle Swarm Optimization Algorithm. In L. Jiao, L. Wang, F. Wu, X. Gao, & J. Liu (Ed.), *ICNC 2006. II.*, pp. 156-165. Berlin Heidelberg: Springer. https://doi.org/10.1007/11881223_20

Goldberg, D. (1989). *Genetic Algorithms in Search, Optimization and Machine Learning* (1. ed.). Massachusetts, USA: Addison-Wesley Longman Publishing.

Herskovits, J., Mappa, P., Goulart, E., & Mota Soares, C. (2005). Mathematical Programming Models and Algorithms for Engineering Design Optimization. *Computer Methods in Applied Mechanics and Engineering, 194*(30-33), 3244-3268. https://doi.org/10.1016/j.cma.2004.12.017

Jang, S., Dai, S., & Sung, S. (2005). The pattern and Externality Effect of Diffusion of Mobile Telecommunications: the Case of OECD and Taiwan. *Information Economics and Policy, 17*(2), 133-148. https://doi.org/10.1016/j.infoecopol.2004.05.001

Kozuko, F., & Bajzer, Z. (2003). Combining Gompertzian Growth and Cell Population Dynamics 185, 153- 167. *Mathematical Biosciences, 185*(2), 153-167. https://doi.org/10.1016/S0025-5564(03)00094-4

Lorentz, M. (1905). Methods of Measuring the Concentration of Wealth. *Publications of the American Statistical Association, 9*(70), 209-219. https://doi.org/10.2307/2276207

Malthus, T. (1798). *An Essay on the Principle of Population.* London.

Mansfield, E. (1961). Technical Change and the Rate of Imitation. *Econometrica, 29*(4), 741-766. https://doi.org/10.2307/1911817

Martens, D., De Backer, M., Haesen, R., Vanthienen, J., Snoeck, M., & Baesens, B. (2007). Classification with Ant Colony Optimization. *IEEE Transactions on Evolutionary Computation, 11*(5), 651-665. https://doi.org/10.1109/TEVC.2006.890229

Martins, J., & Lambe, A. (2013). Multidisciplinary design optimization: A Survey of architectures. *AIAA Journal, 51*(9), 2049-2075. https://doi.org/10.2514/1.J051895

Meyer, W. B., & Turner II, B. L. (1994). *Changes in Land Use and Land Cover: A Global Perspective. Vol. 4,.* Cambridge: Cambridge University Press.

Mitscherlich, E. (1909). Das gesetz des minimums und das gesetz des abnehmenden bodenertrages. *Landwirtsch Jahrbuch, 38*, 537-552.

Moore, E. (1965). Cramming more Components onto Integrated Circuits. 38 (8):pp. 114- 117. *Electronics, 38*(8), 114-117.

Nelder, J., & Mead, R. (1965). A Simplex Method for Function Minimization. *The Computer Journal, 7*(4), 308-313. https://doi.org/10.1093/comjnl/7.4.308

Pang, X., Chen, J., Wang, J., & Hou, Y. (2012). Parametric and Controllable Shape Model of the Water-Lubricated Rubber Journal Bearing. *Advanced Materials Research, 455-456*, 1468-1473. https://doi.org/10.4028/www.scientific.net/AMR.455-456.1468

Pearl, R., & Reed, L. (1920). On the rate of growth of the population of the United States since 1790 and its mathematical representation. *Proceedings of the National Academy of Sciences, 6*(6), 275-288. doi:https://doi.org/10.1073/pnas.6.6.275

Rézsó, F. (2020). Szigmoid görbék alkalmazása tanulócsoportok eredményeinek vizsgálatához. *Multidiszciplináris Tudományok, 10*(3), 195-211. https://doi.org/10.35925/j.multi.2020.3.25

Richards, F. (1959). A Flexible Growth Function for Empirical Use. *Journal of Experimental Botany, 10*(2), 290-300. https://doi.org/10.1093/jxb/10.2.290

Rogers, M. (1962). *Diffusion of Innovations* (3. ed.). New York, USA: The Free Press, Macmillan Publishing Co.

Rosenbrock, H. (1960). An automatic method for finding the greatest or least value of a function. *The Computer Journal, 3*(3), 175-184. https://doi.org/10.1093/comjnl/3.3.175

Sheel, A. (1985). Betrag zur Theorie der Evolutionsstrategie. *Dissertation*. Berlin: TU Berlin.

Silverberg, G., & Lehnert, D. (2003). Evolúciós káosz: növekedés és fluktuációk az "alkotó rombolás" Schumpeter-féle modelljében. In N. Fokasz, *Káosz és nemlineáris dinamika a társadalomtudományokban.* Typotex.

Szabó, F. (2008). Multidisciplinary optimization of a structure with temperature dependent material characteristics, subjected to impact loading. *Internationa Review of Mechanical Engineering, 2*(3), 499-505.

Szabó, F. (2011). Analógia a sport-világcsúcsok története és az evolúciós optimáló algoritmusok iteráció-története között. *GÉP, 62*(9-10), 28-31.

Szabó, F. (2016). Multidisciplinary Optimization of Journal Bearings, using a RVA evolutionary type optimization algorithm. *Acta Polytechnica Hungarica, 13*(7), 181-195. https://doi.org/10.12700/APH.13.7.2016.7.10

Szabó, F. (2017). Evolutionary based system for qualification and evaluation of group achievments (EBSYQ). *International Journal of Current Research, 9*(8), 55507-55516.

Szabó, F. (2018). Optimumkereső algoritmusok iterációtörténetének vizsgálata. *GÉP, 69*(4), 82-85.

Szabó, F. (2019). Application of sigmoid curves in environmental protection. In K. Tóthné Szita, K. Jármai, & K. Voith (Eds.), *Solutions for Sustainable Development* (1. ed., p. 7). London: CRC Press.

Szabó, F. (2020). A COVID-19 járvány időbeli alakulásának vizsgálata szigmoid görbékkel. *Multidiszciplináris Tudományok, 10*(3), 294-306. https://doi.org/10.35925/j.multi.2020.3.35

Szabó, F. (2021). Analysis of Wear Curves as Sigmoid Functions. In K. Jármai, & K. Voith (Ed.), *Vehicle and Automotive Engineering 3. VAE 2020. Lecture Notes in Mechanical Engineering* (pp. 273-281). Singapore: Springer. https://doi.org/10.1007/978-981-15-9529-5_24

Törnquist, L. (1936, 10). The Bank of Finland's Consumption Price Index. *Bank of Finland Monthly*, 1-8.

Törnquist, L. (1981). *Collected Scientific Papers of Leo Törnquist.* Research Institute of the Finnish Economy.

Vajna, S. (2020). *Integrated Design Engineering. Interdisciplinary and holistic product development* (1. ed.). Switzerland: Springer Nature.

Vanderplaats, G. (2007). *Multidiscipline Design Optimization.* Vanderplaats R&D, Inc.

Verhulst, P.-F. (1847). Deuxieme mémoire sur la loi d'accroissement de la population. *Mémoires de l'Académie Royale des Sciences, des Lettres et des Beaux-Arts de Belgique, 20*, 1-32.

Von Bertalanffy, L. (1960). Principles and theory of growth. In W. Nowinski, *Fundamental Aspects of Normal and Malignant Growth* (pp. 137-259). Amsterdam: Elsevier.

Zhang, Z., Zhou, J., Zhou, N., Wang, X., & Zhang, L. (2005). Shape Optimization Using Reproducing Kernel Practice Method and an Enriched Genetic Algorithm. *Computer Methods in Applied Mechanics and Engineering,, 194*(39-41), 4048-4070. https://doi.org/10.1016/j.cma.2004.10.004

A BRIEF OVERVIEW OF GENETIC ALGORITHMS

KRISTÓF SZABÓ

University of Miskolc, Institute of Machine Tools and Mechatronics
H-3515, Miskolc-Egyetemváros
kristof.szabo@uni-miskolc.hu
https://orcid.org/0000-0002-4126-6687

Abstract: This article examines the topic of Genetic Algorithms, discussing the basic concepts and terminology related to Genetic Algorithms. The advantages, disadvantages and limitations of the mentioned algorithms are defined. The different population models and the process of parent selection are presented, as well as the areas of application of the procedure are summarized.

Keywords: genetic algorithms, optimization, evolutionary algorithms

1. INTRODUCTION

Continuing advances in manufacturing and materials science have enabled design engineers to produce complex digital models that are difficult or impossible to produce using traditional manufacturing methods and technologies. This unprecedented manufacturing flexibility will continue to offer even more opportunities and challenges for computer-aided design of digital models. With these possibilities, even the most experienced design engineer's intuition can be underwhelmed. To address design challenges, computer algorithms have been developed to solve the problem based on specific design goals and constraints. This type of genetic algorithm-driven design process is now called Generative Design.

This design approach is not a single algorithm or ready process, but an approach by which the designer defines a series of instructions, rules and relationships that precisely identify the steps required to implement the proposed design and the resulting data or geometry.

Genetic Algorithm (GA) is a search-based optimization technique based on the principles of genetics and natural selection. It is often used in solving optimization

problems, in research and in machine learning stages as it is very useful when the objective function is highly complex, just as in case of Generative Design.

In the optimization process, we have an input and an output, and, in the process, we look for the input that gives the 'best' output. In mathematical terms, the definition of 'best' is the maximization or minimization of one or more objective functions by varying the input parameters. The set of all possible solutions constitutes the search space. In this search space, there is a point that gives the optimal solution. The objective of optimization is to find a given point or set of points in this search space (Erdős-Sélley, Gyurecz, Janik, & Körtvélyesi, 2013), (Hegedűs, 2002).

2. GENETIC ALGORITHMS

Genetic algorithms are search-based algorithms based on the principles of natural selection and genetics. Genetic algorithms were developed by John Holland, his students and colleagues at the University of Michigan, and David Edward Goldberg has achieved great success in solving various optimization problems (Goldberg & Samtani, 1986), (Holland, 1992), (Mitchell, 1998). In genetic algorithms, possible solutions to a given problem undergo recombination and mutation, as in natural genetics. Through this process new individuals are created, and the process is repeated over several generations. Each individual or solution is assigned a so-called fitness value, which is determined by the value of the objective function. More fit individuals are given a better chance of producing individuals with a higher fitness value. This is in line with the Darwinian theory of 'survival of the fittest' (Darwin, 1859). Thus, over generations, better solutions are continuously produced until the stopping criterion is reached. Genetic algorithms are spontaneous processes, but they perform much better than random local search, in which only different random solutions are tried, following the best ones so far (Haupt & Haupt, 2004), (Deb, 2011).

2. 1. The justification for genetic algorithms

Genetic algorithms have many positive features that have made them extremely popular. First, they do not require derivative information, which is not available for many real-world problems. In many cases they are faster and more efficient than traditional methods. They can handle both continuous and discrete functions as well as multi objective problems. It provides a list of 'good' solutions, not just a single solution. You always get an answer to the problem, which can only get better over time. It is useful when the search area is very large and there are many parameters.

In addition to the so-called advantages, the disadvantages or, in a sense, limitations should also be mentioned. Genetic algorithms are not suitable for solving all types

of problems, especially those that are simple and where derived information is available. The calculation of the fitness value is repeated, which can be computationally expensive for certain problems. Assuming a stochastic process, there is no guarantee that the solution is optimal and of the best quality. If not properly implemented, the algorithm may not converge to the optimal solution on the other hand it shows how close a given design solution is from the designer's goals. Genetic algorithms are also cannot be applied when the aim is to find ideas to the design task, and we need originally new ideas (Takács & Kamondi, 2006).

For many problems in computer science, even the most powerful computing systems may take a very long time to solve a problem. In this case, genetic algorithms have proven to be a powerful tool to provide usable, near-optimal solutions in a short time. Traditional gradient-based methods work by starting from a random point and moving in the direction of the gradient until a maximum value is reached. This technique is efficient and works very well for objective functions with a maximum point. But in most real situations this is not the case. Mostly, we have to deal with objective functions that have multiple peaks, which is why these methods fail. This is because they suffer from getting stuck in the local optimum.

2. 2. Basic concepts of Genetic Algorithms

Table 1
Terminology of Genetic Algorithms
(Michalewicz, 1994), (Mitchell, 1998)

Title	Definition
Population	The subset of all coded solutions to a given problem.
Chromosomes	A possible solution to the problem.
Gene	An elementary position on a chromosome.
Allele	The value that a gene takes for a given chromosome.
Genotype	Population of the computational space.
Phenotype	The population in the real solution space in which solutions are represented as they appear in the real world.
Decoding	For simple problems, the phenotype and genotype spaces are the same. In most cases, however, the phenotype and genotype spaces are different. Decoding is the process of transforming a solution from the genotype to the phenotype space, while coding is the process of transforming the solution from the phenotype to the genotype space
Fitness Function	A simply defined fitness function is a function that takes the solution as input and produces the fitness of the solution as output.
Genetic operators	They change the genetic make-up of the offspring. This includes cross-breeding, mutation and selection

When examining genetic algorithms, it is very important to go into sufficient detail about the basic terminology of the procedure, which is summarised in Table 1.

2. 3. The basic structure of Genetic Algorithms

Figure 1 shows the flowchart of the method, which starts with an initial population and can be randomly generated. Every individual or design option can be mentioned as a possible solution to the complete design problem. From this population, so-called parents are selected for subsequent mating. Thanks to the crossing and mutation operators used, new offspring are generated. Finally, these offspring replace the existing individuals in the population and the process is repeated. In this way, genetic algorithms attempt to mimic human evolution to some extent (Mitchell, 1998).
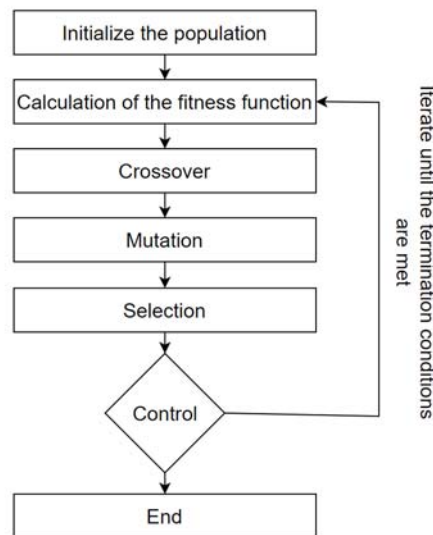
Figure 1. *Flowchart of Genetic Algorithms*

2. 4. Coding of solutions

When implementing a genetic algorithm, one of the most important aspects is the representation we want to use to represent our solutions. Observations have shown that the selection of the appropriate representation to properly define the mappings

between phenotype and genotype spaces is essential for the success of Genetic Algorithm (Goldberg & Samtani, 1986), (Mitchell, 1998).

The binary representation is one of the simplest and widely used representations in genetic algorithms. This representation is shown in Figure 2. In this type of representation, the genotype consists of a set of bits. For some problems, when the solution space consists of Boolean decision variables: yes or no, the binary representation is natural.

0	0	1	0	1	1	1	0	1	0

Figure 2. *Binary representation of genotype*

Figure 3 shows a solution where genes can be defined by continuous rather than discrete variables. In this case, a real-valued representation is most appropriate. However, the accuracy of these real-valued or floating-point numbers may be a function of the computer.

0,5	0,2	0,1	0,4	0,6	0,8	0,3	0,9	0,2	0,8

Figure 3. *Representation of a genotype with continuous variables*

For genes with discrete values, the solution space cannot always be restricted to binary values. If four criteria have to be distinguished, then in such cases the representation of integers may be appropriate, as illustrated in Figure 4.

1	3	2	4	1	4	3	2	2	3

Figure 4. *Representation of a genotype with discrete variables*

In many problems, the solution itself is the order of the elements. In such cases, the permutation representation is the most obvious solution, as shown in Figure 5.

1	5	9	6	4	3	2	8	10	7

Figure 5. *Permutation representation of the genotype*

2. 5. Evaluation of solutions

In steady-state genetic algorithms, one or two offspring are generated in each itera-
tion and replace at least one individual in the population. These algorithms are also
called incremental algorithms. In the generative model, 'n' offspring are generated,
where 'n' is the population size, and at the end of the iteration the entire population
is replaced.

A fitness function is the objective function for the genetic algorithm –it is a function
that takes as input a possible solution to a problem and gives as output a measure of
how 'good' the solution is relative to the problem. It shows how close a design so-
lution is from the designer's original goal. The fitness value is calculated repeatedly.
In most cases, the fitness function and the objective function are the same, with the
objective being to maximise or minimise the objective function. The fitness function
must be fast to compute and, importantly, it must be measurable. In some cases, it
may not be possible to calculate the fitness function directly due to the complexity
of the problem. In such cases, approximations are made.

2. 6. Parent selection

Table 2

Methods of parent choosing
(Mitchell, 1998), (Michalewicz, 1994), (Yang & Soh, 1997)

Method	Description
Roulette wheel selection	A pie chart is divided into 'n' units and the area of each unit is proportional to the fitness value of the parents. Using a fixed point, the selection is made by rotating and stopping the dia-gram
Stochastic universal sampling	Similar to roulette wheel selection, but there are several fixed points so that all parents can be selected at the same time.
Tournament selection	"k" individuals are randomly selected from the population and the best of them is chosen to become the parent. It is also very popular in the literature, as it can work even with negative fit-ness values.
Rank selection	All individuals in the population are ranked according to their fitness. The selection of parents depends on the rank of the in-dividual and not on fitness. It is used when the fitness values of individuals in a population are very close to each other.
Random selection	Parents are randomly selected from the existing population. There is no selection pressure on the fitter individuals, so this strategy is not popular.

The choice of parents is very important for the convergence rate in genetic algorithms, as the right parents lead to better solutions. Maintaining population diversity is crucial to the success of genetic algorithms, so it is important that a highly suitable solution does not produce convergent results within a few generations, as this leads to a loss of diversity. This process is called premature convergence, which is an undesirable state in genetic algorithms.

Fitness Proportional Choice is one of the most popular ways of parenting. In it, each individual has a probability of becoming a parent proportional to his or her fitness score. Those with higher fitness scores have better genes and are more likely to be selected. There are several possible cases of fitness proportional selection. The most common methods of selection are summarised in Table 2.

3. SUMMARY

Genetic algorithms are not only used in case of Generative Design, but it is most often used in optimization tasks where the value of a given objective function needs to be maximized or minimized under a given set of constraints. In economics, genetic algorithms are used to characterise various economic models. Genetic algorithms are used to train neural networks, in various digital image processing (DIP), in dense pixel matching tasks, to solve various scheduling problems, and to process spectrometric data. Genetic Algorithm Based Machine Learning (GBML) is a narrow field of machine learning in which algorithms have been used to plan the trajectories of robotic arms. The method has also been exploited in parametric design of aircraft, which has been used to design aircraft more efficiently. Genetic algorithms are good approaches for multimodal optimization, in which multiple optimal solutions must be found (Mitchell, 1998), (Borsodi & Takács, 2022).

The following article summarises the topic of genetic algorithms, covering the basic concepts and terminology related to genetic algorithms. The advantages, disadvantages and limitations of these algorithms were identified. The different population models and the process of parental selection were presented, and the applications of the procedure were summarised.

REFERENCES

Borsodi, E., & Takács, Á. (2022). Generative Design: An Overview and Its Relationship to Artificial Intelligence. *Design of Machines and Structures, 12*(2), 54-60. doi:https://doi.org/10.32972/dms.2022.013

Darwin, C. (1859). *Darwin, C. R.: 1872. The origin of species by means of natural selection, or the preservation of favoured races in the struggle for life.* London: John Murray.

Deb, K. (2011). Multi-objective Optimisation Using Evolutionary Algorithms: An Introduction. In:. In L. Wang, A. Ng, & K. Deb, *Multi-objective Evolutionary Optimisation for Product Design and Manufacturing.* London: Springer. doi:https://doi.org/10.1007/978-0-85729-652-8_1

Erdős-Sélley, C., Gyurecz, G., Janik, J., & Körtvélyesi, G. (2013). *Mérnöki optimalizáció.* Typotex.

Goldberg, D. E., & Kuo, C. (1987). Genetic algorithms in pipeline optimization. *Journal of Computing in Civil Engineering, 1*(2). doi:https://doi.org/10.1061/(ASCE)0887-3801(1987)1:2(128)

Goldberg, D., & Samtani, M. (1986). Engineering optimization via genetic algorithm. *Engineering, .*

Haupt, R., & Haupt, S. (2004). *Practical Genetic Algorithms* (2 ed.). Hoboken, New Jersey: John Wiley and Sons.

Hegedűs, G. (2002). A módszeres géptervezés alkalmazása ipari mérőgép fejlesztése esetén. *Doktoranduszok Fóruma.* Miskolc: Miskolc University Press.

Holland, J. (1992). *Adaptation in Natural and Artificial Systems* (Reprint ed.). Bradford Books.

Michalewicz, Z. (1994). *Genetic Algorithms + Data Structures = Evolution Programs* (2. ed.). Springer.

Mitchell, M. (1998). *An Introduction to Genetic Algorithms.* MIT Press.

Takács, Á., & Kamondi, L. (2006). A genetikus algoritmusok. In V. Csibi (Ed.), *OGÉT 2006: XIV. Nemzetközi Gépész Találkozó* (pp. 332-335). Kolozsvár: EMT.

Yang, J., & Soh, C. (1997). Structural Optimization by Genetic Algorithms with Tournament Selection. *Journal of Computing in Civil Engineering*, 195-200. doi:https://doi.org/10.1061/(ASCE)0887-3801(1997)11:3(195)

DESIGN OF A UNIVERSAL DEVICE HOLDER SYSTEM

DÁNIEL TÓTH

University of Miskolc, Institute of Machine Tools and Mechatronics
H-3515, Miskolc-Egyetemváros
daniel.toth1@uni-miskolc.hu
https://orcid.org/0000-0001-8928-4633

Abstract: During the performance of the dust chamber tests, the device systems must meet not only mechanical but also flow aspects, for this reason a special system –which cannot be used on other test equipment– must be developed to perform the dust tests. During the development of the concept of the modular device system (MDDT: Modular Device for Dust Test) designed for carrying out dust chamber tests, the design methods based on function analysis, used in the design of production equipment, can be well applied.

Keywords: dust test, function structure, modular device system

1. INTRODUCTION

In connection with several test devices, there was a need to develop a device system that could represent an economical solution for testing an extremely large number of products. A basic requirement for the device systems used in the test equipment is a high degree of universality, which can adapt as large a range of the vehicle components to be tested to the workspace of the test equipment as possible with the smallest possible number of components. Based on previous experience, such equipment problems can be effectively solved by creating a modular equipment system.

2. COMPONENTS OF MODULAR DEVICE SYSTEM

During the development of the concept of the modular device system (Modular Device for Dust Test, hereinafter MDDT) designed to carry out dust chamber tests, the first and most important operation is the exploration of the elementary functions of the planned system (Deutsches Institut für Normung, 1997). Among the basic

functions, there are those without which the MDDT system does not work, these mandatory basic functions. There are elementary functions whose effects are equivalent to each other, but one of the alternative functions must be included in the MDDT function structures, these are the mandatory alternative elementary functions. The non-mandatory elementary functions can increase the function content of the component, but their application is not absolutely necessary for the operation of the component, they must be integrated into the MDDT system according to user needs. Figure 1 shows the symbols and meanings of elementary functions.
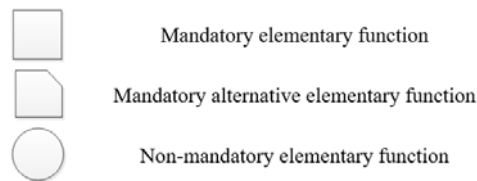
Figure 1. Symbols of elementary functions

The modular device system designed to carry out dust chamber tests is made up of functional sub-units, the individual sub-units implement the elementary functions listed below.

f(K) – Device body
The central function of the MDDT system is the device body (frame), which enables the inclusion of other functions. The device body must be designed in such a way that it does not create a significant obstacle in the way of the dust flowing from top to bottom in the test device and does not change the flow lines formed around the tested generator.

f(Rk) – Fixing the device body
This function enables the device body to be fixed in several possible positions on the grid worktable of the dust-test equipment. When designing the function, it is necessary to ensure that, during installation and removal or relocation of the device body, it can also be fixed from the work area, and the grid worktable does not have to be removed from the test machine for this reason.

f(SX) – Displacement of the generator in the X-axis direction in the device
The geometric dimensions of the generators to be tested are different. If the plane of the belt drive in the drive system cannot be changed, the generators must be made axially movable in the device. (The X-axis of the coordinate system is parallel to the axis of the drive.)

f(S_Y)

f(SY) – Y-axis displacement of the generator in the device
If the tension of the drive belt in the drive system cannot be adjusted independently of the device (e.g. with a tension roller), then the generators must be made movable in the Y direction in the device. (The Y-axis of the coordinate system is perpendicular to the axis of the drive.)

f(S_Z)

f(SZ) – Shifting the generator in the Z-axis direction in the device
The geometric dimensions of the generators to be tested are different. If the cross-sectional dimensions of the tested generator are larger, the generators must be made movable in the Z direction so that the tested generator can fit above the device body. (The Z-axis of the coordinate system is perpendicular to the worktable of the test equipment.)

f(S_A)

f(SA) – Rotating the generator around the X-axis in the device
The generators must be tested in the same spatial position as they are installed in the vehicle. This function will allow dust tests to be performed in any angle position. Tests in any angular position may also be necessary during the development of special generators.

f(R_X)

f(RX) – Fixation of device elements moving in the direction of the X-axis in the device
After adjusting the plane of the belt drive, the device components must be fixed.

f(R_Y)

f(RY) – Fixation of device elements moving in the direction of the Y-axis in the device
If the belt tension is adjusted by shifting the tested generator in the device, the device elements adjusted according to the belt tension must be fixed.

f(R_Z)

f(RZ) – Fixation of device elements moving in the direction of the Z-axis in the device
Device elements set according to the cross-sectional dimensions of the tested generator must be fixed.

f(R_A)

f(RA) – Fixing the orientation in the device
After setting the test orientation of the generator, the device components must be fixed.

f(A)

f(A) – Shape that does not affect flow conditions
All elements of the MDDT device system must be designed in such a way that they do not create a significant obstacle in the path of dust flowing from top to bottom in the test equipment, do not change the flow lines formed around the tested generator, and ensure constant flow conditions during the tests.

f(I)

f(I) – Common mechanical interface
In order to the MDDT device system to be suitable for testing as many types of generators as possible using as few device elements as possible, it is advisable to concentrate the differences resulting from the geometric differences in the

perception of the generators on one element. This is the task of this function, so it matches the connector dimensions of the device and the tested generator.

f(P) – Baffle plates to modify the flow

This is an optional feature. After performing many dust tests, the experience may arise that the intensity of the dust flowing in the dust chamber around the tested generator must be condensed/thinned somewhere. The developed static flow capacity can be modified with deflector/shadow plates. These deflector/shield plates must always be designed according to the unique needs that induce the test. They can be fixed to the device frame or to the grid table of the dust chamber.

3. MDTT DEVICE SYSTEM

The elementary functions described in the previous point can be linked in many possible ways into a function structure that satisfies the requirements related to the design of the MDDT system. If we create device structures from predefined elementary functions, we essentially record the elements of the set whose elements we want to take into account in the formation of the versions (Tajnafői, 1993), (Takács G. , 1997), (Takács Á. , 2017). Figure 2 shows the relationship of elementary functions. It is also necessary to record how certain elements (atoms) of the set are connected to other elements (atoms) of the set. The above definitions can be considered as a graph in a mathematical sense, where the elementary functions are the corner points of the graph, the defined mutual relations are the edges of the graph, and the individual conceptual versions are subgraphs of the graph.

Figure 2. Characterization of the relationship of elementary functions with a graph

The maximum number of edges (m) of a graph with n corner points can be calculated using the equation (1), which assumes that every atom is connected to every other atom and that there can be no parallel edges between two atoms.

$$m = \frac{n(n-3)}{2} + n \tag{1}$$

The edges of the graph define a connection between one atom each, so in the case of n atoms, a maximum of m connections must be defined. The connection between atoms can be described using relation (2), which is the adjacency matrix.

$$S = \begin{bmatrix} 0 & k_{a_1,a_2} & . & . & k_{a_1,a_n} \\ k_{a_2,a_1} & 0 & . & . & . \\ . & . & 0 & . & . \\ . & . & . & 0 & . \\ k_{a_n,a_1} & . & . & . & 0 \end{bmatrix} \tag{2}$$

The characteristic of the matrix is that the value set of the elements is 0 or 1, according to whether the relationship exists or not, its main diagonal is made up of zero elements, because the relationship of the elements with themselves cannot be logically interpreted. Another characteristic is that the matrix is symmetrical because the connection of the elements is mutual and bidirectional. It follows from the above that, in terms of the necessary information content, the triangular matrix above the main diagonal is sufficient for a clear description of the system of connections between elementary functions. The vertices can be arranged arbitrarily; therefore, a graph S can have many adjacency matrices, which means that the permutation of the rows and columns of S always results in a different matrix, but this does not change the content meaning of the graph, in this case the relationship of the members' connections. Figure 3 contains the adjacency matrix of the functions of MDDT system. To write down the device concepts, a graph can be used, the corner points of which are individual building elements that can be used to build the device system, and the individual connections between the elements are represented by the edges of the graph. The graph contains all possible device variants in the form of subgraphs. By determining the number of versions, it is possible to find out how many sub-graphs the complete graph contains, which as independent device versions can satisfy the device requirements for testing the generators. No general method can be prescribed for search and selection, the logic of the selection is provided by the specific planning task. In most cases, the method of equal probability can be applied well, but due to the homogeneous treatment of functions, it also creates many incorrect solutions during planning. This graph search method assigns the same random variable to each corner point of the graph.

	f(K)	f(R_K)	f(S_X)	f(S_Y)	f(S_Z)	f(S_A)	f(R_X)	f(R_Y)	f(R_Z)	f(R_A)	f(A)	f(I)	f(P)
f(K)	0	k(K,R_k)	k(K,S_X)	k(K,S_Y)	k(K,S_Z)	k(K,S_A)	k(K,R_X)	k(K,R_Y)	k(K,R_Z)	k(K,R_A)	k(K,A)	k(K,I)	k(K,P)
f(R_K)		0	k(R_k,S_Y)	k(R_k,S_Y)	k(R_k,S_Z)	k(R_k,S_A)	k(R_k,R_X)	k(R_k,R_Y)	k(R_k,R_Z)	k(R_k,R_A)	k(R_k,A)	k(R_k,I)	k(R_k,P)
f(S_X)			0	k(S_X,S_Y)	k(S_X,S_Z)	k(S_X,S_A)	k(S_X,R_X)	k(S_X,R_Y)	k(S_X,R_Z)	k(S_X,R_A)	k(S_X,A)	k(S_X,I)	k(S_X,P)
f(S_Y)				0	k(S_Y,S_Z)	k(S_Y,S_A)	k(S_Y,R_X)	k(S_Y,R_Y)	k(S_Y,R_Z)	k(S_Y,R_A)	k(S_Y,A)	k(S_Y,I)	k(S_Y,P)
f(S_Z)					0	k(S_Z,S_A)	k(S_Z,R_X)	k(S_Z,R_Y)	k(S_Z,R_Z)	k(S_Z,R_A)	k(S_Z,A)	k(S_Z,I)	k(S_Z,P)
f(S_A)						0	k(S_A,R_X)	k(S_A,R_Y)	k(S_A,R_X)	k(S_A,R_A)	k(S_A,A)	k(S_A,I)	k(S_A,P)
f(R_X)							0	k(R_x,R_Y)	k(R_x,R_Z)	k(R_x,R_A)	k(R_x,A)	k(R_x,I)	k(R_x,P)
f(R_Y)								0	k(R_Y,R_Z)	k(R_Y,R_A)	k(R_Y,A)	k(R_Y,I)	k(R_Y,P)
f(R_Z)									0	k(R_z,R_A)	k(R_z,A)	k(R_z,I)	k(R_z,P)
f(R_A)										0	k(R_A,A)	k(R_A,I)	k(R_A,P)
f(A)											0	k(A,I)	k(A,P)
f(I)												0	k(I,P)
f(P)													0

Figure 3. *Adjacency matrix of MDDT system functions*

$$P_{a1} = P_{a2} = \cdots = P_{an} \tag{3}$$

Since the random variable Pai represents the selectability of each corner point of the graph in a subgraph, the value set of ai is 0 or 1. Figure 4 shows the selection of subgraphs.

Figure 4. *Selection of subgraphs*

The corner points of the entire graph take on different values for each calculation cycle, so a different subgraph can be formed in each cycle depending on the corner points with value ai=1 and the edges starting from them. After the individual corner points are randomly selected, several subgraphs can be formed at the same time, of which only the largest contiguous size (which contains more atoms) is taken into account. The defined functions can be connected to each other in several possible ways and with several possible contents. Figure 5 shows the adjacency matrix of the version that can be designed according to the requirements. Figure 6 shows the function structure corresponding to the adjacency matrix. The initial concept of the dust chamber device is presented in Figure 7.

	f(K)	f(R$_K$)	f(S$_X$)	f(S$_Y$)	f(S$_Z$)	f(S$_A$)	f(R$_X$)	f(R$_Y$)	f(R$_Z$)	f(R$_A$)	f(A)	f(I)	f(P)
f(K)	0	1	1	0	0	0	1	1	1	1	1	0	1
f(R$_K$)		0	0	0	0	0	0	0	0	0	1	0	0
f(S$_X$)			0	1	0	0	1	0	0	0	1	0	0
f(S$_Y$)				0	1	0	0	1	0	0	1	0	0
f(S$_Z$)					0	0	0	0	1	0	1	0	0
f(S$_A$)						0	0	0	0	1	1	1	0
f(R$_X$)							0	0	0	0	1	0	0
f(R$_Y$)								0	0	0	1	0	0
f(R$_Z$)									0	0	1	0	0
f(R$_A$)										0	1	0	0
f(A)											0	0	0
f(I)												0	0
f(P)													0

Figure 5. A possible adjacency matrix of MDDT system functions

In addition to the specified dimensions of the generator, the component that implements the f(I) function depicted in red (see Figure 7) is capable of handling differences resulting from changes in installation dimensions. This is important because the other parts of the device may remain unchanged. In the final design, each generator group has one of these common parts. From the point of view of the tests, the most important function is f(A), which stipulates that all components must be designed in such a way that they affect the flow picture of the flowing dust as little as possible. The f(K) function (appliance frame) is designed in such a way that it can

be moved to different places depending on the grid division and can be fixed there with hooks if necessary.
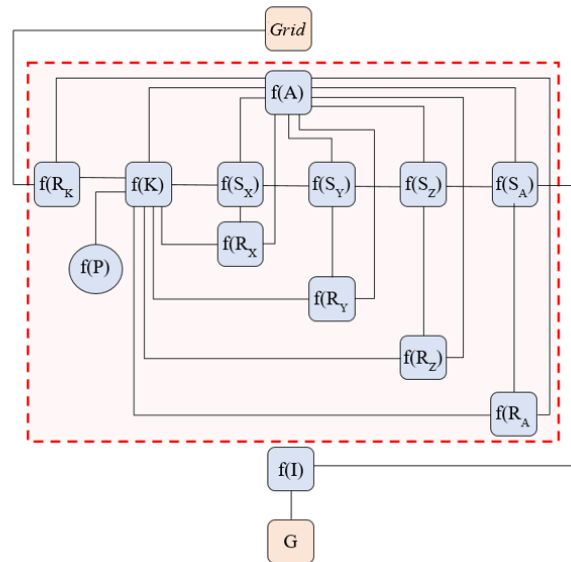

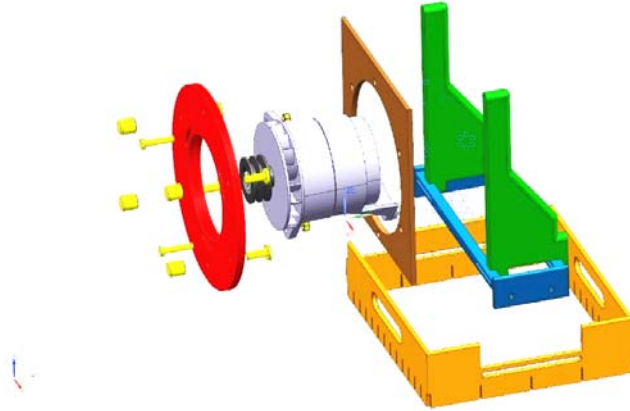**Figure 6.** *Function structure of a possible solution of MDDT system*

Figure 7. *Exploded view of the dust chamber device*

4. SUMMARY

Within the framework of this article, the development of the concept of a modular device system designed to perform dust chamber tests was presented. Based on the list of requirements established by the dust chamber, elementary functions were defined, from which a graph can be created. The optimal device concept can be selected from the device variations that can be derived from the graph. A study was prepared on the design process of the device concept, which is well suited for explaining the design methodology of methodical production device design.

REFERENCES

Deutsches Institut für Normung. (1997). DIN EN 60068-2-68. *Environmental testing - Part 2: Tests; test L: Dust and sand.*

Tajnafői, J. (1993). *Szerszámgéptervezés II. Struktúraképzések.* Budapest: Nemzeti Tankönyvkiadó.

Takács, Á. (2017). Computer Aided Concept Building. *Solid State Phenomena, 261*, 402-407. doi:https://doi.org/10.4028/www.scientific.net/ssp.261.402

Takács, G. (1997). Szerszámgép struktúrák tervezése grafikus adatbázisokkal. *PhD thesis*. Miskolc.